Investigation of the distinctive role of lung macrophage subtypes in airway inflammation

Seunghan Han

Department of Medical Science

The Graduate School, Yonsei University

Investigation of the distinctive role of lung macrophage subtypes in airway inflammation

Directed by Professor Ji-Hwan Ryu

The Doctoral Dissertation
submitted to the Department of Medical Science,
the Graduate School of Yonsei University
in partial fulfillment of the requirements for the degree of
Doctor of Philosophy in Medical Science

Seunghan Han

December 2023

This certifies that the Doctoral Dissertation of Seunghan Han is approved.

Thesis Supervisor: Ji-Hwan Ryu

Thesis Committee Member#1: Hyung-Ju Cho

Thesis Committee Member#2: Sang Sun Yoon

Thesis Committee Member#3: Young-Min Hyun

Thesis Committee Member#4: Jong-Seok Moon

The Graduate School
Yonsei University

December 2023

ACKNOWLEDGEMENTS

I would like to express genuine appreciation for my supervisor, Prof. Ji-Hwan Ryu, who guided and encouraged me throughout the entire Doctor of Philosophy course. He provided me with the exact path and the confidence I needed to carry out my thesis from the beginning to the end.

I'm deeply grateful to the members of my thesis committee - Prof. Hyung-Ju Cho, Prof. Sang Sun Yoon, Prof. Young-Min Hyun, and Prof. Jong-Seok Moon. They helped me move my research in a better direction and provided advice in a variety of ways.

My special thanks go to Prof. Daehee Hwang and Dr. Do Young Hyeon, who provide such wonderful cooperation for research. And I'm also grateful to Prof. Youn Wook Chung, who supported and advised me whenever I was in trouble. Thank you to our lab colleagues, Jimin Cha, Sungmin Moon, Daeun Jeong, Kyeongeun Kwon, Taehyun Kim, and Wuseong Lee.

Finally, to my family—Yuseok Han, Youngrim Jo, and Chasong Han—and to all the relatives, thank you for all that you do. I don't express it enough, but I am incredibly thankful for your endless support and love. Thank you so much.

Sincerely,

Seunghan Han

<TABLE OF CONTENTS>

NETosis

LIST OF FIGURES

Part 1. Alveolar macrophage recruitment is responsible for attenuation of neutrophilic inflammation upon *Staphylococcus aureus* (*S. aureus*) infection

Part 2. Distinctive CD39$^+$CD9$^+$ lung interstitial macrophages suppress IL-23/Th17-mediated neutrophilic asthma by inhibiting NETosis

ABSTRACT

Investigation of the distinctive role of lung macrophage subtypes in airway inflammation

Seunghan Han

Department of Medical Science
The Graduate School, Yonsei University

(Directed by Professor Ji-Hwan Ryu)

Lung macrophages comprise several subtypes and play diverse roles in states of inflammation. Here, we investigate the roles of alveolar macrophages (AM) in acute airway inflammation and interstitial macrophages (IM) in chronic airway inflammation.

In Part 1, when the lungs are infected with bacteria, alveolar macrophages (AMs) are recruited to the site and play a crucial role in protecting the host by reducing excessive lung inflammation. Despite this pivotal function, the regulatory mechanisms triggering the recruitment of AMs to lung alveoli during an infection remain not fully understood. In our study, we identified a critical role for NADPH oxidase 4 (NOX4) in the recruitment of AMs during *S. aureus* lung infection. Our findings reveal that NOX4 knockout (KO) mice exhibited decreased recruitment of AMs, accompanied by increased lung neutrophils and injury compared to wild-type (WT) mice, all in response to *S. aureus* infection. Interestingly, the burden of *S. aureus* in the lungs showed no significant difference between NOX4 KO and WT mice. Furthermore, we observed that depletion of AMs in WT mice during *S. aureus* infection led to an increase in the number of neutrophils and lung injury, similar to levels observed in NOX4 KO mice. Additionally, we found that expression of intercellular adhesion molecule-1 (ICAM1) in NOX4 KO mice-derived lung endothelial cells was lower than that in WT mice-derived endothelial cells. Therefore, we conclude that NOX4 plays a crucial role in inducing the recruitment of AMs by

controlling ICAM1 expression in lung endothelial cells. This regulation is responsible for resolving lung inflammation during acute *S. aureus* infection.

In Part 2, $CD39^{+}CD9^{+}$ IMs suppress IL-23/Th17-mediated neutrophilic asthma by inhibiting NETosis. IL-23-Th17 axis is responsible for neutrophilic inflammation in various inflammatory diseases. Here, we discovered a novel potent pathway to suppress neutrophilic inflammation in severe asthma. In our neutrophil- dominant asthma (NDA) model, single-cell multiomics analysis identified a subpopulation of $CD39^{+}CD9^{+}$ IMs suppressed by IL-23 in NDA conditions, but increased by IL-23 inhibitor. Adoptively transferred $CD39^{+}CD9^{+}$ IMs suppressed neutrophil extracellular trap formation (NETosis), a representative phenotype of NDA, together with Th17 cell activation and neutrophilic inflammation. $CD39^{+}CD9^{+}$ IMs first attach to neutrophils in a CD9-dependent manner, and then remove ATPs near neutrophils that contribute to NETosis in a CD39-dependent manner. Our results suggest that $CD39^{+}CD9^{+}$ IMs are a potent regulator of NETosis in neutrophilic inflammation, comparable to Th17 cells in IL-23-Th17 axis. We finally demonstrated decreased $CD39^{+}CD9^{+}$ immune cells in patients with severe asthma or chronic rhinosinusitis, suggesting $CD39^{+}CD9^{+}$ IMs as a potential therapeutic target for IL-23-Th17-mediated airway inflammatory diseases.

Taken together, our study demonstrates that specific subtypes of macrophages play crucial roles in regulating neutrophilic inflammation during both acute and chronic airway inflammation in the lung.

Key words: lung macrophage, macrophage subtypes, alveolar macrophage, *Staphylococcus aureus*, NADPH oxidase 4, bacterial infections, interstitial macrophage, neutrophilic asthma, IL-23, chronic airway inflammation.

Investigation of the distinctive role of lung macrophage subtypes in airway inflammation

Seunghan Han

Department of Medical Science
The Graduate School, Yonsei University

(Directed by Professor Ji-Hwan Ryu)

I. INTRODUCTION

Lung macrophages have several subtypes, such as inflammatory macrophages, alveolar macrophages (AM), and interstitial macrophages (IM) in human and mouse[1-3]. Generally, they are characterized by their phenotypes, the proinflammatory M1 and anti-inflammatory M2 types[1-3]. Each subtype of macrophage plays distinctive roles in airway inflammation[1]. In acute and chronic airway inflammation, inflammatory macrophages have an M1 phenotype and participate in proinflammatory state, neutrophilic inflammation, and tissue injury[4]. However, AMs and IMs can have M1 or M2 phenotypes in acute and chronic airway inflammation[4]. Their distinct roles and interactions are poorly understood.

Initially, in the lung, AMs are the predominant immune cells and provide a key function in maintaining lung homeostasis[5-7]. During severe situations such as bacterial infections, monocytes are recruited from the bloodstream to the alveoli[8]. For recruitment of the monocytes, LFA1 and MAC1 on the monocytes bind to endothelial intercellular adhesion molecule-1 (ICAM1), and then the monocytes proceed to rolling, crawling, and transmigration[9,10]. And the recruited monocytes are differentiated into monocyte-derived AMs[11]. The AMs reduce excessive inflammation and effect resolution of inflammation by producing anti-inflammatory and repair

factors[12-14]. However, the regulatory role of AM recruitment into the alveoli in bacterial infection is not well defined. Therefore we investigate their role in bacterial infection in Part 1.

In Part 1, bacterial pneumonia is associated with high rates of morbidity and mortality in individuals with compromised immune systems or hospitalization[15,16]. In immune-compromised patients or community-acquired pneumonia (CAP) patients, *Staphylococcus aureus* (*S. aureus*) has been recognized as a cause of lung infection[17,18]. *S. aureus* is a gram-positive bacterium and a commensal microbe in the upper respiratory tract and on the skin[19]. Although *S. aureus* is well known as a nosocomial and respiratory pathogen, the virulence mechanisms of *S. aureus* have concentrated on microbial factors[20]. Furthermore, host defense mechanisms against *S. aureus* have been studied primarily in neutrophils[21]. Therefore, identifying the regulatory mechanisms of immune cells other than neutrophils against *S. aureus* infection is necessary.

NADPH oxidases (NOX), such as NOX2, NOX4, and DUOX, are known to be host proteins that produce reactive oxygen species (ROS) in several cell types in the lung[22]. NOX4 is a major source of cellular superoxide anion, which is involved in the biological functions of cell survival, differentiation, and apoptosis[23-25]. NOX4 increases ICAM1 expression in the endothelium via the TLR5-flagellin interaction[26]. NOX4 in inflammatory macrophages enhances NLRP3 inflammasome activation via fatty acid oxidation against *Streptococcus pneumoniae*[27]. And NOX4 in macrophages helps to block *Toxoplasma gondii* infection[28]. Moreover, knockdown of NOX4 in lung attenuates pulmonary permeability after *Pseudomonas aeruginosa* infection[29]. According to these studies, NOX4 plays a variety of roles against various pathogens. However, the specific immunologic role of NOX4 against *S. aureus* lung infection remains unclear.

In Part 1, we demonstrated that vascular endothelial growth factor (VEGF) induces ICAM1 expression in a NOX4-dependent manner, resulting in the recruitment of AMs into the lung. Additionally, we showed that AM recruitment is crucial for resolving neutrophilic inflammation in mice with NOX4 following *S. aureus* infection. These findings shed new light on the protective role of NOX4, highlighting the connection between VEGF and AM recruitment against S. aureus infection.

Secondly, in the lung, IMs exist in the interstitium and are identified in three types following their marker proteins, CD11c and MHCII[3]. They have both proinflammatory and anti-inflammatory properties in states of inflammation[3]. However, the role of IMs in neutrophilic asthma and the interaction between the IMs and IL-23 are not well defined. Therefore, we investigate the role of IMs in neutrophilic asthma in Part 2.

In Part 2, asthma is a chronic inflammatory disorder of the airways with multiple endotypes and high morbidity[30-32]. There are several types of asthmatic airway inflammation involving T helper (Th) 2 cell-mediated eosinophilic, Th17 cell-mediated neutrophilic, or even agranulocytic inflammation. Recently, relationships of lung neutrophilic inflammation with asthma severity and exacerbations in asthma patients have been reported[33]. Neutrophilic airway inflammation often shows no response to inhaled or systemic corticosteroids, unlike eosinophilic airway inflammation, resulting in poor disease control and recurrent exacerbations. Therefore, there has been a significant need for alternative therapeutic approaches for neutrophilic airway inflammation[34]. However, the development of a new therapy suited for neutrophilic asthma has been hampered because of limited understanding of the underlying mechanisms[35].

Myeloid cells, including macrophages and dendritic cells (DCs), have antigen-presenting roles, instruct naïve $CD4^+$ T cell differentiation into effector

Th2 and Th17 cells in asthma, and control tolerance to inhaled antigens[36,37]. High doses of antigens, such as ovalbumin (OVA) and house dust mite (HDM), coupled with LPS stimulation are reported to induce Th17 cell differentiation, involving expression of CD40 and CD86, and high levels of proinflammatory cytokines, including IL-6, IL-1β, IL-23, and transforming growth factor-β (TGF-β)[38-40]. In particular, IL-23 induces neutrophilic infiltration in the airways of asthmatic mice, leading to severe asthma through Th17 cell activation and IL-17 secretion[41,42]. Recently, potential therapeutic effects of IL-23 inhibition using IL-23 antagonists or by depletion have been evaluated in neutrophilic asthma patients or mouse models[43-45]. However, the development of IL-23-targeting therapeutics has been slowed down because the regulatory mechanisms of IL-23 and its specific role in neutrophilic asthma are not clear. Thus, the target cells of IL-23 and their functional roles in neutrophilic airway inflammation need to be investigated.

To identify known or novel target cell populations in various lung disease conditions, single-cell RNA-seq (scRNA-seq) and ATAC-seq (scATAC-seq) have been recently used[46-51]. The lung is a multifaceted tissue composed of more than 40 kinds of cell populations[52]. A few single-cell analyses have been performed for respiratory diseases. For example, scRNA-seq analysis in mouse models have reconstructed cell lineage hierarchies of lung epithelial cells and identified novel subsets of innate lymphoid cells (ILCs) precursors[53-55]. It was also applied to decipher the transcriptional landscape of lung-resident ILCs in an allergic lung inflammation model, and the neuromedin U (NMU) receptor (NMUR) was identified as a modulator of allergen-driven responses of type 2 ILC2s[56]. In addition, scATAC-seq analysis in lungs from healthy donors of three different age groups revealed cis-regulatory elements with age-increased activity linked to *TMPRSS2*, a gene associated with host entry of severe acute respiratory syndrome

coronavirus 2[57]. However, the target cells of IL-23 in neutrophilic airway inflammation have not been investigated using single-cell analysis.

Here, we present an OVA-driven mouse model exhibiting the phenotypes of neutrophil-dominant asthma (NDA), such as Th17 cell activation, neutrophilic inflammation, and resistance of steroids (e.g., Dexamethasone). We observed that the treatment of IL-23p19 neutralizing antibody (αIL-23p19) significantly reduced Th17 cell activation and neutrophilic inflammation in our NDA model, suggesting its suitability for investigating the mechanisms underlying the therapeutic effects of αIL-23p19. Therefore, we used scRNA-seq and scATAC-seq analyses to identify IMs responsible for the therapeutic effects of αIL-23p19, examined functional roles of these target cells in neutrophil airway inflammation using our NDA model via diverse molecular and cellular experiments, and then demonstrated their therapeutic effects through adoptive transfer. We finally examined associations of these target cells with severity in patients with asthma and another upper airway inflammatory disease, chronic rhinosinusitis (CRS).

Consequently, we show two subtypes of macrophages that can regulate neutrophilic inflammation. In Part 1, AM recruitment is responsible for attenuation of neutrophilic inflammation upon *S. aureus* infection. In Part 2, $CD39^{+}CD9^{+}$ IMs suppress IL-23/Th17-mediated neutrophilic asthma by inhibiting NETosis. Taken together, our findings demonstrate that specific macrophage subtypes play crucial roles in regulating neutrophilic airway inflammation in the lung.

II. MATERIALS AND METHODS

Part 1. Alveolar macrophage recruitment is responsible for attenuation of neutrophilic inflammation upon *Staphylococcus aureus* (*S. aureus*) infection

A. Animals

Male C57BL/6 mice were purchased from Orient Bio (Seongnam, Korea). NOX4 knockout (KO) mice on a C57BL/6 background were bred at the animal facility of Yonsei University. Age-matched, 8- to 12-wk-old mice were used for all experiments. Mice were housed under specific pathogen-free conditions and maintained in a 12 h light-dark cycle until the start of each experiment. All experiments were performed in accordance with the guidelines of the Association for Assessment and Accreditation of Laboratory Animal Care International (AAALAC International) and were approved by the Institutional Animal Care and Use Committee (IACUC) of Yonsei University Health System.

B. Preparation of *S. aureus*

S. aureus (ATCC 29213) was grown on a Brain Heart Infusion (BHI) agar plate at 37℃ overnight. The *S. aureus* colonies were inoculated into 10 ml fresh BHI medium and cultured in a shaking incubator at 37℃ overnight. The cultured *S. aureus* was inoculated into fresh BHI medium and grown in the shaking incubator until OD600 values of 1. GFP-tagged *S. aureus* was cultured on a BHI agar plate with tetracycline (100 μg/ml) at 37℃ overnight. GFP-tagged *S. aureus* was grown in BHI medium containing tetracycline (100 μg/ml) until OD600 values of 1.

C. Bacterial infection model

Mice were anesthetized by zoletil/rompun mixture. The mice were intranasally instilled with 3×10^7 colony forming units (CFUs) of *S. aureus* in 40 μl PBS. Control mice were intranasally instilled with 40 μl PBS. After the infection, mice were sacrificed at the indicated time points (0, 12, 24, 48, 72, and 120 h).

D. Bronchoalveolar lavage fluid (BALF) and lung tissue sample collection

Mice were sacrificed by administering an overdose of the zoletil/rompun mixture. BALF was obtained by injecting 1 ml of ice-cold PBS into the trachea using a catheter. The aspiration was repeated twice until no further fluid was collected. The collected BALF was centrifuged at 4,000 rpm for 5 min at 4°C. The supernatant was used for cytokine measurement, while the pellet was counted using a hemocytometer and stained for flow cytometry. Through the right ventricle, 10 ml of ice-cold PBS were perfused into the lungs. The left lobe of the lung was fixed with 4% paraformaldehyde for H&E staining, while the right lobes of the lung were extracted and chopped into small pieces. The right lobes of the lung were dissociated with collagenase type II solution (0.005 g collagenase type II and 1 μl DNase in 5 ml PBS per mouse) for 1 h at 37°C. After dissociation, the samples were filtered twice through a 70 μm strainer and then centrifuged at 4,000 rpm for 5 min. The pellet was stained and then isolated using FACS or magnetic-activated cell sorting (MACS).

E. Histological inflammatory score

H&E staining of the lung section was examined and assessed through BX53 microscope (Olympus Corporation, Tokyo, Japan). The

section was analyzed and qualified through random selection. Using a score, the degree of lung inflammation was assessed. Briefly, a score of 0 meant there were no leukocytes around bronchioles or alveoli; a score of 1 meant there were a few leukocytes there; a score of 2 meant there were 1–3 layers of leukocytes there; and a score of 3 meant there were 5 layers of leukocytes there.

F. Immunofluorescence stain

The paraffin-embedded lung tissue was stained to identify neutrophils and macrophages. After deparaffinization and rehydration using xylene at decreasing concentrations (100% to 50%), the slides underwent heat-induced Ag retrieval in 10 mM sodium citrate buffer (pH 6.0) for 20 min at 95°C. The slides were then blocked with PBS containing 2% BSA and 2% donkey serum for 2 h at room temperature (RT). They were stained with DAKO Ab diluent (Agilent, Carpinteria, CA, USA), including neutrophil Abs (Abcam, Cambridge, UK) (1:100), and anti-F4/80 Abs (Novus Biologicals, LLC, Centennial, CO, USA) (1:100) overnight at 4°C. After the washing step, the slides were stained with secondary donkey anti-rat IgG Abs conjugated with Alexa Fluor 488 (1:1,000) and donkey anti-rabbit IgG Abs conjugated with Alexa Fluor 546 (1:1,000) for 1 h in the dark at RT. They were mounted with Fluoroshield containing DAPI (Sigma-Aldrich, St. Louis, MO, USA). The stained slides were analyzed using a Carl-Zeiss confocal microscope LSM 700. For quantification, the mean fluorescence intensity (MFI) of Ly6G or F4/80 relative to DAPI was processed using ZEN 2.3 black software (Carl Zeiss, Dresden, Germany).

G. BALF protein and Cytokine measurement

To measure BALF protein, BALF supernatant was collected after centrifugation. The supernatant was diluted by one-fifth and quantified by Pierce™ BCA Protein Assay Kit (ThermoFisher Scientific, Waltham, MA, USA). Cytokines were measured in the supernatant by using Duoset ELISA kits for mouse TNFα and VEGF (R&D Systems, Minneapolis, MN, USA) according to the manufacturer's protocol.

H. AM depletion and *In vivo* inhibitor treatment

To deplete AMs, mice were anesthetized and then intranasally pre-treated with clophosome A clodronate liposome (f70101c; FormuMax Scientific, Sunnyvale, CA, USA) 48 h before bacterial infection. Control mice were intranasally pre-treated with control liposome for clophosome (f70101; FormuMax Scientific). Mice were anesthetized and then intranasally treated with IgG control or anti-VEGF Ab (5 μg per mouse; R&D Systems) to block local alveolar VEGF at the same time as infection.

I. Flow cytometry and FACS sorting

Single cells from the dissociated lung or BALF pellet were lysed with RBC lysis buffer for 5 min at 4°C and centrifuged. After removing the supernatant, the cell pellet was washed twice with PBS containing 2% FBS. The washed pellet was counted using a hemocytometer and stained with Abs for 30 min at 4°C. The Abs were PE-Cy7-anti-CD45 (BD Bioscience, San Jose, CA, USA), eFlour-450-anti-Ly6G (eBioscience, San Diego, CA, USA), APC-anti-CD11c (BioLegend, San Diego, CA, USA), PE-anti-CD170 (SiglecF; BioLegend), FITC-anti-CD11b (BD Bioscience), Percp-cy5.5-anti-CD64 (BioLegend), and Brilliant-Violet711- anti-F4/80 (BioLegend). To examine *in vivo* AM cell death, BALF cells were stained with PE-cy7-anti-CD45, APC-anti-CD11c, PE-anti-CD170 (SiglecF),

DAPI, and Annexin V-FITC Apoptosis Kit (BioVision Inc., Milpitas, CA, USA). The stained cells were analyzed using a FACS Fortessa BD flow cytometer. To isolate AMs, stained cells were isolated with $CD45^{+}CD11c^{+}SiglecF^{+}$ using BD FACS Aria II. The data was analyzed using FlowJo software (BD Biosciences).

J. MACS for $CD31^{+}$ endothelium and BMDN

The right lobes of the lung were chopped into small pieces and dissociated using a collagenase type II solution for 1 h at 37°C. The samples were filtered twice through a 70 μm strainer and washed. The single cells were washed after being processed in RBC lysis buffer for 5 min at 4°C. The single cells were stained with CD31 microbeads (130-097-418; Miltenyi Biotec, Bergisch Gladbach, Germany) for 20 min at 4°C. After washing, the stained samples were isolated by using positive selection in an autoMACS Pro separator (Miltenyi Biotec).

For BMDN sorting, the femurs and tibias of mice were removed and cut at both ends with scissors. A 5 ml of PBS was added, and the cells were lysed with RBC lysis buffer. The single cells were stained with a neutrophil isolation kit (130-097-658; Miltenyi Biotec) for 20 min at 4°C. After washing, the stained samples were isolated by using positive selection in an autoMACS Pro separator (Miltenyi Biotec).

K. Immunoblotting

Cells were lysed in RIPA buffer (Sigma-Aldrich) containing 1% Protease and Phosphatase Inhibitor Cocktail (Sigma-Aldrich) for 10 min on ice. The cells were sonicated and centrifuged for 15 min at 4 °C at 13,000 rpm. The supernatant was collected and quantified by Pierce™ BCA Protein Assay Kit (ThermoFisher Scientific). A total of 10 μg protein was

loaded onto an 8% or 12% SDS-PAGE gel and then transferred to a polyvinylidene difluoride membrane by using a wet/tank transfer system (Bio-Rad, Hercules, CA, USA). The membrane was blocked by Tris-buffered saline with Tween 20 (TTBS) containing 5% Difco skim milk (BD Biosciences) for 1 h at room temperature. After blocking, the membrane was incubated with Purified anti-CD54 (ICAM1) Ab (BioLegend) or anti-VCAM1/CD106 Ab (R&D Systems) or anti-β-actin Ab (Santa Cruz Biotechnology, Santa Cruz, CA, USA) overnight at 4°C with rotation. The membrane was washed with TTBS three times and incubated with secondary Abs linked with HRP for 2 h at RT.

L. Real time PCR

Following MACS or FACS sorting, total mRNA was extracted from the isolated cells using GeneAll Hybrid-R (305-101; Geneall, Seoul, Korea). The extracted mRNA was quantified using a NANO DROP 1000 spectrophotometer (ThermoFisher Scientific). cDNA was obtained with PrimeScript RT Master Mix (RR036A; Takara, Kusatsu, Japan). Real-time PCR was performed with KAPA SYBR FAST (KK4605; Roche, Basel, Switzerland) and QuantStudio 3 Real-Time PCR System (Applied Biosystems, Waltham, MA, USA). The sequences were as follows: mouse NOX4 sense primer 5′-TTG CCT GGA AGA ACC CAA GT-3′, NOX4 antisense primer 5′-TCC GCA CAA TAA AGG CAC AA -3′, mouse ICAM1 sense primer 5′- AGG TGG TTC TTC TGA GCG GC-3′, ICAM1 antisense primer 5′-AAA CAG GAA CTT TCC CGC CA -3′, mouse GAPDH sense primer 5′-TAG GGC CTC TCT TGC TCA GT-3′, GAPDH antisense primer 5′-GGA CCT CAT GGC CTA CAT GG-3′. Gene specific expression was normalized against the GAPDH housekeeping gene. The relative expression was determined by the comparative $2^{-\Delta\Delta CT}$ method.

M. Ea.hy926 cell culture

Ea.hy926 cells were obtained from Yonsei University (Seoul, Korea) and maintained in Endothelial Cell Growth Medium-2 Bulletkit (EGM2, CC-3162; Lonza, Basel, Switzerland) at 37°C in a humidified 5% CO_2 incubator. Ea.hy926 cells in 6-well plates were pre-treated with 5 μM GLX353122 (HY-100111; MedChemExpress, Monmouth Junction, NJ, USA), a NOX4 inhibitor. The cells were treated for 6 h with 25 ng/ml recombinant human VEGF 165 ($rhVEGF_{165}$) at 37°C in a humidified 5% CO_2.

N. *Ex vivo* AM apoptosis assay

AMs ($CD45^+CD11c^+CD11b^-SiglecF^+$), isolated by FACS, were seeded and cultured *ex vivo* in DMEM (Lonza) in 12-well plates. The cells were infected with *S. aureus* (multiplicity of infection [MOI] 10) and incubated for 300 min at 37°C with 5% CO_2. They were then collected and stained using the Annexin V-FITC/PI Apoptosis Kit (BioVision Inc.). The stained cells were analyzed using a FACS Fortessa BD flow cytometer.

O. *S. aureus*-GFP uptake assay

BMDN isolated by MACS and AMs isolated by FACS were seeded in 12-well plates. The cells were infected with GFP-tagged *S. aureus* (MOI 10 or 20) and incubated for 1 h at 37°C with 5% CO_2. Then, they were collected in a tube and centrifuged at 4,000 rpm, 5 min, RT. The supernatant was cultivated on a BHI agar plate for measuring CFU. The pellet was washed twice and analyzed for GFP-positive populations using FACS as described previously.

P. Statistical analysis

Comparisons of 2 samples were processed by an unpaired Student's *t*-test, whereas analysis of variance was followed by one-way ANOVA using Bonferroni's multiple comparisons test in all statistical analyses. Comparisons of multiple samples, including time variance, were analyzed by two-way ANOVA test. Data were expressed as mean ± SEM for all graphs. p-values <0.05 were considered statistically significant. Statistical analyses were performed using the GraphPad PRISM 8 software (GraphPad, San Diego, CA, USA).

Part 2. Distinctive $CD39^{+}CD9^{+}$ lung interstitial macrophages suppress IL-23/Th17-mediated neutrophilic asthma by inhibiting NETosis

A. Animals

Wild-type C57BL/6 male mice (aged 6–8 weeks) were purchased from Orient Bio (Gyeonggi, Korea), and housed under specific pathogen-free conditions until an asthma model was generated. All experiments were performed in accordance with the Association for Assessment and Accreditation of Laboratory Animal Care International (AAALAC International) guidelines and approved by the Institutional Review Board of the Yonsei University College of Medicine.

B. Generation of the NDA mouse models

In the OVA-derived NDA mouse model, mice were anesthetized with Zoletil-Rompun mixture and then sensitized through intranasal instillation of OVA (75 μg, Grade V; Sigma-Aldrich, St. Louis, MO, USA) and LPS (10 μg) on days 0, 1, 2, and 7. On 7 days after the fourth sensitization, mice were anesthetized, challenged through intranasal instillation of OVA (100 μg) only on days 14, 15, 21, and 22, and then

sacrificed on day 24. When quantified using ToxinSensor chromogenic LAL Endotoxin assay kit (Genescript, Piscataway, NJ, USA), the OVA (100 μg) used was found to contain 5.77 EU LPS. In the HDM-derived NDA mouse model, mice were anesthetized with Zoletil-Rompun mixture and then sensitized through intranasal instillation of house dust mite extracts (HDM, 25 μg; XPB82D3A25, Greer Laboratories, Lenoir, NC, USA) and LPS (10 μg) on days 0, 1, and 2. On 7 days after the fourth sensitization, mice were anesthetized, challenged through intranasal instillation of HDM (6.25 μg) on days 14, 15, 18, and 19, and sacrificed on day 21. Instillated HDM (25 μg) contained 20 EU LPS by limulus amebocyte assay (Greer Laboratories).

C. Neutralizing antibody, dexamethasone, and inhibitor treatment

Mice were pre-treated intraperitoneally (i.p.) with IL-23p19 (400 μg per mouse; BioxCell, West Lebanon, NH, USA) or dexamethasone (1 mg/kg per mouse; Sigma-Aldrich) 1 h before the challenge, but not during the sensitization period. Control mice were treated with rat IgG2a isotype control (400 μg per mouse; BioxCell). All inhibitors were pretreated i.p. 1 h before the challenge: POM1 (20 mg/kg; Tocris Bioscience, Bristol, UK), anti-CD9 antibody (5 mg/kg; BD Pharmingen, San Diego, CA, USA), IL-17/IL-17A Antibody (250 μg/kg; R&D Systems, Minneapolis, MN, USA), and GSK484 (4 mg/kg; Cayman Chemical, Michigan, USA).

D. Measurement of methacholine AHR levels

At 24 h after the last OVA challenge (on day 23), responses to inhaled methacholine (Sigma-Aldrich) were measured in unrestrained mice using whole-body plethysmography (WBP; Buxco Research Systems, Wilmington, NC, USA). Mice were nebulized for 3 min with PBS,

followed by increasing the amount of methacholine at multiple concentrations (6.25, 12.5, 25, and 50 mg/ml). Lung function was recorded for 2 min and calculated as enhanced pause (P_{enh}), which is a dimensionless unit that correlates with pulmonary resistance. Calculations were performed using FinePoint software (Buxco Electronics Ltd)[58]. Moreover, to measure AHR in an invasive manner, mice were anesthetized and operated via tracheostomy. The mice were connected using a metal cannula to FlexiVent (Scireq, Montreal, Canada) and mechanically ventilated. To determine respiratory system resistance (R_{rs}), methacholine at multiple concentrations (0, 6.25, 12.5, 25, and 50 mg/ml) was nebulized. Snapshot150 and Quick Prime-3 perturbation were then measured. Each value was repeated until acceptable measurements (coefficient of determination > 0.95) were recorded. The mean value of R_{rs} was then calculated[59].

E. Sample collection from blood, BALF, and lung tissue

Mice were sacrificed by an overdose of a Zoletil-Rompun mixture. BALF was acquired using 1 ml of cold PBS through the murine trachea. The aspiration was repeated twice until no further fluid was collected. BALF was centrifuged (1600 × g, 5 min), and the separated BALF supernatant was used to measure cytokine levels. The BALF pellets were used for cell counting and flow cytometry analysis. Through the right ventricle, 10 ml of PBS was perfused into the lungs. The left lobe of the lung was extracted and fixed for H&E, PAS, and immunofluorescence staining. The right lobes of the lung were extracted and chopped into small pieces. The lung tissues were homogenized using a collagenase dissociation solution [25 mg collagenase type II and 1 μl DNase in 5 ml Hank's balanced salt solution (HBSS) per mouse] for 1 h at 37°C. After dissociation, the samples were filtered through a 70 μm strainer twice and

then centrifuged at 1600 × g for 5 min. The pellet was stained and analyzed using flow cytometry.

F. Flow cytometry

Single cells were lysed with red blood cell (RBC) lysis buffer for 3 min on ice and then centrifuged at 1600 × g for 5 min. After the supernatant was removed, the pellet was stained with an antibody (1:100) for 20 min on ice and then washed twice. The washed pellet was resuspended in PBS containing 2% fetal bovine serum (FBS) and filtered through a 40 μm strainer. The samples were then analyzed using flow cytometry. The cells obtained from BALF and lung samples were counted and stained with 4′,6-diamidino-2-phenylindole (DAPI), eFluor 450 anti-mouse Ly6G (eBioscience, San Diego, CA, USA), Percp/Cyanine 5.5-anti-mouse CD11c (Biolegend, San Diego, CA, USA), PE-anti-mouse CD170 (SiglecF) (Biolegend), FITC rat-anti mouse CD11b (BD Bioscience, San Jose, CA, USA), PE-Cy7 rat-anti mouse CD45 (BD Bioscience), AF700-rat anti-CD9 (NOVUSBIO, Centennial, CO, USA), PE/Dazzle 594 anti-mouse CD39 (Biolegend).

To examine T cell population, the lung single cell samples were stained with LIVE/DEAD Fixable Aqua Dead Cell Stain Kit (ThermoFisher), Percp/Cyanine 5.5-anti-mouse/human CD11b (Biolegend), Percp/Cyanine 5.5-anti- CD14 (eBioscience), Percp/Cyanine 5.5-anti-CD19 (Biolegend), Percp/Cyanine 5.5-anti-B220 (eBioscience), Percp/Cyanine 5.5-anti-I-A/1-E (Biolegend), Brilliant Violet 605-anti-mouse TCR β chain (Biolegend), BV421 Mouse Anti-Mouse RORγt (BD), Alexa Fluor 488-anti-FOXP3 (eBioscience), PE/Cyanine7-anti-mouse IFN-γ (Biolegend), PE-CF594-anti-T-bet (BD), Alexa Fluor 700-anti-mouse IL-17A (BD), APC-eFluor 780-CD44 (eBioscience), Brilliant Violet

711-anti-mouse CD4 (Biolgend), PE-anti-GATA3 (eBioscience), or APC-anti-mouse IL-5 (Biolgend). For intracellular staining, the cells were processed using the FOXP3 transcription factor staining buffer set (eBioscience) according to the manufacturer's protocol. The stained cells were analyzed by sorting Th17 [live $Dump^-$($CD11b^-CD14^-CD19^-B220^-$ $I\text{-}A/I\text{-}E^-$)$FOXP3^-CD44^+CD4^+TCR\beta^+ROR\gamma t^+T\text{-}bet^-$], Th1 [live $Dump^-$ $FOXP3^-CD44^+CD4^+TCR\beta^+ROR\gamma t^-T\text{-}bet^+$] and Th2 cells [live $Dump^-$ $FOXP3^-CD44^+CD4^+TCR\ \beta^+ROR\gamma t^-T\text{-}bet^-GATA3^+$][60].

Cells obtained from human ethmoid mucosa samples were stained with Brilliant Violet 421 anti-human CD45 (Biolegend), PE anti-human CD9 (Biolegend,), FITC anti-human CD39 (Biolegend), Brilliant Violet 605 anti-human CD193 (Biolegend), or APC anti-human CD16 (Biolegend). The stained cells were analyzed using an FACS Fortessa BD flow cytometer or sorted with an FACS Aria II BD cell sorter (BD Biosciences, Sparks, MD, USA). For scRNA-seq and scATAC-seq, $CD45^+$ cells isolated from the lungs pooled from two or more mice were used for each replicate.

G. Cell morphology

To explore the identity of sorted cells, we examined their morphologies by cytospin preparation. $Ly6G^-CD39^+CD9^+CD11b^+CD11c^-$ or $Ly6G^+CD39^+$ $CD9^+CD11b^+CD11c^-$ cells were fixed on slides using cytospin centrifuge. The cells were then stained using the Wright–Giemsa. The stained cells were characterized as mononuclear (MN) or polymorphonuclear (PMN) cells based on the morphology of their nuclei.

H. Adoptive transfer

We pooled lungs from 4 to 6 donor mice and sorted using flow

cytometry. We isolated donor cells from CD45.1$^+$ mice and used recipient mice as CD45.2$^+$ mice. CD39$^+$CD9$^+$ IM (CD45$^+$CD11b$^+$CD11c$^-$Ly6G$^-$ CD39$^+$CD9$^+$) donor cells were sorted from PBS/PBS or OVA+LPS/OVA +αIL-23p19 mice on day 24. Moreover, CD39$^+$CD9$^+$ neutrophil (CD45$^+$ CD11b$^+$CD11c$^-$Ly6G$^+$ CD39$^+$CD9$^+$) donor cells were sorted from PBS/PBS mice. PBS was also used as a non-cellular negative control. On 14, 15, 21, and 22 days, the sorted 3-4×10^4 cells were adoptively transferred into the recipient mice (OVA+LPS/OVA) via intravenous route. When total number of 10^5 donor cells isolated from CD45.1$^+$ mice were injected, the number of 10^3 cells were present in the lung of the recipient CD45.2$^+$ mice under OVA+LPS/OVA on 24 days.

I. Cytokine measurements

Cytokine levels in BALF supernatant were measured using a Duoset ELISA Development kit for mouse IL-17 and IL-22 (R&D Systems, Minneapolis, MN, USA), the OptEIA set for mouse IL-5 and IFN-γ (BD Biosciences), and mouse IL-23 ELISA Kit (Abcam) for mouse IL-23.

J. scRNA-seq

Cellular suspensions were loaded onto a chromium controller (10x Genomics) to generate nanoliter-sized gel bead-in-emulsions (GEMs) containing single cells, reagents, and a single gel bead containing barcoded oligonucleotides. Barcoded sequencing libraries were prepared using Chromium Next GEM Single Cell 3' v3.1 Dual Index (10X Genomics) according to the manufacturer's protocol. The sequencing libraries were sequenced on NovaSeq 6000 (Illumina) with the following read lengths: 28 base pairs (bp) for Read 1 (16 bp 10x Barcode + 12 bp UMI), 10 bp for Sample Index (dual), and 90 bp for Read 2. The raw and processed data of

scRNA-seq were deposited at Gene Expression Omnibus (GEO) database (GSE222456).

K. scRNA-seq data analysis

Illumina BCL files were demultiplexed and converted to FASTQ files using 'cellranger mkfastq' function in Cell Ranger software (v.6.1.2)[61]. The resulting FASTQ files were used to perform alignment to mouse GRCm38 genome, filtering, and UMI counting, as well as to produce gene-barcode matrices using 'cellranger count' function. Subsequent data analysis was performed using Seurat (v.4.0.4)[62]. We first selected cells that had the number of genes per cell over 200 and less than 5,000, the number of UMIs per cell over 3,000, and the percent of mitochondrial reads less than 10%. Gene counts for the selected cells were then normalized by the LogNormalize method using 'NormalizeData' function, and 2,000 highly variable genes were identified using 'FindVariableFeatures' function. Data integration between the samples was performed using 'IntegrateData' function. Cell-to-cell variation in the number of detected UMIs, mitochondrial contamination, and cell cycle stage was regressed out using 'ScaleData' function. For clustering analysis, linear dimensional reduction was performed on the scaled data using 'RunPCA' function, and the number of statistically significant principal components (PCs) used for the subsequent analyses was determined using an Elbow plot. Louvain clustering method was then used to cluster the cells using 'FindNeighbors' and 'FindClusters' functions with a resolution of 0.1 (total cell clustering and subclustering of neutrophil/monocyte cluster) or 0.2 (subclustering of $CD11b^+$ macrophage, alveolar macrophage, dendritic cell, and monocyte clusters). Uniform manifold approximation and projection (UMAP), a nonlinear dimensional reduction method, was used to visualize the

clustered cells. Transfer of cell type labels from ImmGen dataset[63] was performed using SingleR[64] with default parameters.

L. Identification of marker genes significantly upregulated in the individual cell clusters

Using the normalized gene counts for each detected gene, we calculated Z-transformed Wilcoxon's rank-sum statistic values (Z-values) between a cell cluster (Group 1) and the other clusters (Group 2; e.g., Cluster 0 versus Clusters 1–10). We then estimated empirical distributions of Z-values for the null hypothesis (i.e., the expression level of a gene is not different between the two groups) by random permutation of the cells in the two groups. Using the estimated empirical distributions, we computed the adjusted *P*-values for the gene. Finally, we identified the genes significantly upregulated in a cluster compared to the other clusters as those that had 1) adjusted *P*-values < 0.01 (total cell clustering) or 0.05 (subclustering), 2) log-fold changes > 0.4 (1.49-fold; total cell clustering) or 0.25 (1.28-fold; subclustering), and 3) median normalized counts of the cells in the cluster larger than those of the cells in the other clusters.

M. scATAC-seq

Cellular suspensions were loaded onto a Chromium Controller (10x Genomics) to generate nanoliter-sized GEMs containing single-cell nuclei, reagents, and a single gel bead containing barcoded oligonucleotides. Barcoded sequencing libraries were prepared using Chromium Next GEM Single Cell ATAC v1.1 (10x Genomics) according to the manufacturer's protocol. The sequencing libraries were sequenced on NovaSeq 6000 (Illumina) with the following read lengths: 50 bp for Read 1, 16 bp for 10x Barcode in the i5 read, 8 bp for Sample Index in the i7 read,

and 50 bp for Read 2. The raw and processed data of scATAC-seq were deposited at Gene Expression Omnibus (GEO) database (GSE222455).

N. scATAC-seq data analysis

Illumina BCL files were demultiplexed and converted to FASTQ files using 'cellranger-atac mkfastq' function in Cell Ranger ATAC software (v.2.0.0). The resulting FASTQ files were used to perform the alignment to the mouse GRCm38 genome, filtering, barcode counting, and peak calling as well as to produce peak-barcode matrices using 'cellranger-atac count' function. The subsequent data analysis was performed using the R package Signac (v.1.7.0)[65]. We first selected cells with the number of genes per cell over 200, the number of UMIs per cell over 1000, total number of fragments in peaks over 3,000, but less than 30,000, percent of fragments in peaks over 15%, nucleosome signal less than 4, and transcriptional start site (TSS) enrichment score over 2. The number of fragments in peaks for the selected cells was then normalized by the term frequency-inverse document frequency (TF-IDF) normalization method using 'RunTFIDF' function, and peaks detected in more than 10 cells were selected using 'FindTopFeatures' function. For dimension reduction, singular value decomposition was performed on the TF-IDF matrix for the selected peaks using 'RunSVD' function. Integration of the low-dimensional embeddings between the samples was then performed using 'IntegrateEmbeddings' function. Second to 20^{th} (total cell clustering) or 30^{th} (subclustering) components were used for the subsequent analyses. SLM clustering method was then used to cluster the cells based on peak intensities using 'FindNeighbors' and 'FindClusters' functions with a resolution of 0.075 (total cell clustering), 0.15 (subclustering of $CD11b^{+}$ macrophage cluster), or 0.3 (subclustering of neutrophil/monocyte cluster).

For subclustering analysis, only the cells predicted as $CD11b^{+}$ macrophage and neutrophil/monocyte by label transfer in ATAC C1 and ATAC C6 were used, respectively. UMAP was used to visualize the clustered cells. The activity of each gene was quantified by summing the fragments intersecting the gene body and promoter region using 'GeneActivity' function. Gene activities were then normalized by the LogNormalize method using 'NormalizeData' function. Transfer of cell type labels from the scRNA-seq data was performed using 'TransferData' function.

O. Analysis of differentially accessible peaks

We identified differentially accessible peaks (DAPs) between the clusters by utilizing logistic regression using 'FindAllMarkers' function with default parameters in Signac (v.1.7.0). Finally, we identified the DAPs as those that had 1) adjusted *P*-values < 0.05, 2) log-fold changes > 0.18, and 3) percent of expressed cells > 10%. If peaks were identified as DAPs in multiple clusters, we assigned them to the cluster with the largest log-fold change. DAPs were further classified into the followings, according to the peak annotation provided by 'cellranger-atac count' function in Cell Ranger ATAC software (v.2.0.0): 1) promoter peaks when the peaks overlapped with the promoter region [from 3 kbp upstream to 100 bp downstream of transcription start site (TSS)] of any protein coding gene; 2) distal peaks when they were within 200 kbp of the closest TSS, but not in the promoter region; 3) intergenic peaks when they were not classified as promoter or distal peaks. Of note, the default promoter region of 1 kbp upstream was modified to 3 kbp upstream in our analysis due to the small number of promoter peaks for the subsequent analyses. To identify motifs enriched by the DAPs, we performed the enrichment analysis of motifs for each peak

group using 'FindMotifs' function in Signac and then selected the motifs with adjusted *p*-value < 0.05.

P. Functional enrichment analysis

To identify cellular processes represented by the genes, we performed an enrichment analysis of gene ontology biological processes (GOBPs) for the genes using DAVID software[66] and then selected the GOBPs with *P*-value < 0.05 and gene count ≥ 3. To identify cellular processes represented by the DAPs, we performed the enrichment analysis of GOBPs using GREAT software[67] and then selected the GOBPs with FDR Q-value from binomial test < 0.05 and peak count ≥ 2.

Q. Bulk RNA-sequencing and data analysis

Total RNA was isolated from $CD39^{+}CD9^{+}$ IMs (n = 3) and $CD39^{-}CD9^{-}$ monocytes (n = 3) under OVA+LPS/OVA+αIL-23p19 condition using TRIzol RNA Isolation Reagent (Life technologies, Carlsbad, CA, USA), and purified according to the manufacturer's instructions. The libraries were prepared for 151 bp paired-end sequencing using RNA Prep with Enrichment, (L) Tagmentation (96 Samples) (Illumina). These cDNA libraries were qualified with the Agilent 4200 Tapestation (Agilent) and quantified with the Qubit Flex Fluorometer (Thermo Fisher Scientific) according to the manufacturer's library protocol. Sequencing was performed as paired-end using NovaSeq 6000 (Illumina). For the read sequences from the sequencing, we removed the adapter sequences and the ends of reads less than Phred quality score 20 using cutadapt (v.1.18)[68]. We then mapped the resulting reads to the *Mus musculus* reference genome (GRCm38) using HISAT2 (v.2.2.1)[69]. We filtered out PCR or optical duplicate reads using Picard (v.2.25.5)

(https://broadinstitute.github.io/picard/). We counted the remaining reads for gene features (GTF file of GRCm38) using HTSeq (v.0.11.3)[70]. To estimate the fractions of cells belonging to RNA CM-C3, RNA NM-C1, RNA MO-C0, RNA AM-C2, and RNA DC-C2 in $CD39^{+}CD9^{+}$ IMs and $CD39^{-}CD9^{-}$ monocytes, we performed deconvolution analysis with CIBERSORTx[71] based on cell type-specific RNA signatures (i.e., marker genes) of these five subclusters. We operated the software in absolute mode with S-mode batch correction and 100 permutations, according to the instructions. The raw and processed data of RNA-sequencing were deposited at Gene Expression Omnibus (GEO) database (GSE222459).

R. Analysis of RNA expression profiles of asthma patients

We obtained three RNA expression profiles of lung tissues collected from asthma patients with severity information available via bronchial biopsy or endobronchial brushing from GEO database: SARP (GSE63142[72]; endobronchial brushing, microarray), U-BIOPRED (GSE76225[73]; bronchial biopsy, microarray), and IMSA (GSE158752[74]; endobronchial brushing, RNA-sequencing). We downloaded the normalized $\log_2$-intensities (microarray dataset) or read counts (RNA-sequencing datasets) from GEO database. Since oral corticosteroids may affect the expression of genes associated with severity, mild/moderate patients who received oral corticosteroid were excluded from the analysis. For the microarray datasets, we applied quantile normalization[75] to the normalized $\log_2$-intensities across the individual samples, and then calculated $\log_2$-fold changes with respect to their median values. We next subtracted the minimum of the $\log_2$-fold changes from the $\log_2$-fold changes to set the minimum to zero. Using these values or read counts, we performed deconvolution analysis with CIBERSORTx based on cell

type-specific RNA signatures of RNA CM-C0-5 to estimate the fractions of cells belonging to RNA CM-C0-5 in the lung tissues. We operated the software in absolute mode, with S-mode batch correction and 100 permutations, according to the instructions.

S. Histological inflammatory score

H&E staining was observed through BX53 microscope (Olympus Corporation) and analyzed through random selection. The extent of lung inflammation was estimated by a score. Briefly, score 0 corresponded to no infiltration of leukocytes around bronchioles and alveoli; score 1 indicated a little infiltration of leukocytes around bronchioles and alveoli; and score 2 or 3 were assigned to 1-3 or 5 layers of leukocyte infiltration around bronchioles and alveoli, respectively[76].

T. Immunofluorescence staining

To identify NETs from lung tissue, the left lobe of the lung was collected as described above and fixed with 4% paraformaldehyde (PFA) for 24 h. The left lung lobe was paraffin-embedded for staining. For deparaffinization and rehydration, the slides were washed in xylene, subsequently in ethanol as decreasing concentrations (100, 95, 70, and 50%), and finally with PBS. Next, the slides were boiled in 10 mM sodium citrate buffer (pH 6.0) for 20 min at 90°C for antigen retrieval. The lung tissues were incubated with PBS containing 2% bovine serum albumin (BSA) and 2% donkey serum (Sigma-Aldrich) for 1 h at room temperature (RT). They were stained with DAKO antibody diluent (Agilent, Carpinteria, CA, USA) including anti-histone H3 (citrulline R2+R8+R17) antibody (Abcam, Cambridge, UK) (1:100) and anti-MPO antibodies (NOVUSBIO) (1:100) overnight at 4°C. After washing the slides with PBS, the slides

were stained with DAKO diluent including secondary donkey anti-rabbit IgG antibodies conjugated with Alexa Fluor 568 (1:1000) and donkey anti-goat IgG antibodies conjugated with Alexa Fluor 647 (1:1000) for 2 h in the dark at RT. Finally, the slides were mounted with Fluoroshield containing DAPI (Sigma-Aldrich) and stored at 4°C[77].

For visualization of $CD39^{+}CD9^{+}$ IMs in human biopsy or mouse lung, human ethmoid, colon mucosa biopsies or mouse lung tissues were fixed with 4% PFA for 24 h. The biopsies and lung tissues were embedded in paraffin. They were deparaffinized and rehydrated as described above. The slides were boiled in 1 mM EDTA (pH 8.0) for 20 min at 90°C for antigen retrieval and then incubated with PBS containing 2% BSA and 2% donkey serum for 1 h at RT. For human biopsies, they were stained with DAKO antibody diluent including recombinant anti-CD39 antibody (Abcam) (1:100), anti-CD9 antibody (Abcam) (1:100), and anti-CD45 antibody (ThermoFisher) (1:100) for overnight at 4°C. For mouse lung tissues, they were stained with DAKO antibody diluent including recombinant anti-CD39 antibody (Abcam) (1:200), anti-CD9 antibody (Novus Biologicals) (1:200), and anti-F4/80 antibody (Santa Cruz) (1:200) for overnight at 4°C. After washing the slides with PBS, the slides were stained in DAKO diluent including secondary donkey anti-rabbit IgG antibodies conjugated with Alexa Fluor 546 (1:1000), donkey anti-mouse IgG antibodies conjugated with Alexa Fluor 647 (1:1000), and anti-rat IgG antibodies conjugated with Alexa Flour 488 (1:1000) (Invitrogen, Carlsbad, CA, USA) for 2 h in the dark at RT. The slides were mounted with Fluoroshield containing DAPI (Sigma-Aldrich) and stored at 4°C [77]. All samples were analyzed and quantified using a Carl-Zeiss confocal microscope LSM 700, and all quantifications were processed using ZEN 2.3 black software (Carl Zeiss, Dresden, Germany).

U. *ex vivo* co-culture NETosis assay

Neutrophils and $CD39^+CD9^+$ IMs were sorted using flow cytometry. Neutrophils (1×10^5 cells/well) were seeded and cultured *ex vivo* for 2 or 15 h with or without $CD39^+CD9^+$ IMs (1×10^5 cells/well) in Dulbecco's Modified Eagle's Medium (DMEM; Lonza) supplemented with 10% FBS and 1% penicillin/streptomycin (P/S) on chamber slides (Nunc Lab-TEK II 4 Chamber slide system, Sigma-Aldrich) pre-coated with poly D-lysine hydrobromide (Sigma-Aldrich). POM1 (10 μM/well; Tocris Bioscience), anti-CD9 antibody (5 μg/ml; BD Biosciences), or ATP (100, 1, 0.1, and 0.01 μM/well) were added to the wells simultaneously with $CD39^+CD9^+$ IMs. To identify NETs from *ex vivo* co-culture slides, the slides were fixed with 10% PFA and permeabilized with 0.5% Triton X-100 after incubation. The slides were incubated with PBS containing 2% bovine serum albumin (BSA) and 2% donkey serum (Sigma-Aldrich) for 1 h at room temperature (RT). They were stained with DAKO antibody diluent including anti-histone H3 (citrulline R2+R8+R17) antibody (Abcam) (1:100) and anti-MPO antibody (NOVUSBIO) (1:100) overnight at 4°C. After washing the slides with PBS, the slides were stained with DAKO diluent including secondary donkey anti-rabbit IgG antibodies conjugated with Alexa Fluor 568 (1:1000) and donkey anti-goat IgG antibodies conjugated with Alexa Fluor 647 (1:1000) for 2 h in the dark at RT. Finally, the slides were mounted with Fluoroshield containing DAPI (Sigma-Aldrich) and stored at 4°C. All samples were analyzed and quantified using a Carl-Zeiss confocal microscope LSM 700, and all quantifications were processed using ZEN 2.3 black software (Carl Zeiss).

V. *ex vivo* cell-based apoptosis assay

$CD39^+CD9^+$ IMs (5×10^4 cells/well) sorted using flow cytometry were seeded and cultured *ex vivo* in Dulbecco's Modified Eagle's Medium (DMEM; Lonza) on chamber slides (Nunc Lab-TEK II 8 Chamber slide system, Sigma-Aldrich). Recombinant IL-23 (1μg/ml, R&D Systems) or anti-IL-23 receptor antibody (1μg/ml, R&D Systems) was added to the wells simultaneously with $CD39^+CD9^+$ IMs for 1 h. The slides were stained using Annexin V-FITC Apoptosis Detection Kit (Biovision, CA, USA). The stained slides were fixed with 4% PFA and mounted with Fluoromount aqueous mounting medium (Sigma-Aldrich). All samples were analyzed and quantified using a Carl-Zeiss confocal microscope LSM 700, and all quantifications were processed using ZEN 2.3 black software (Carl Zeiss).

W. Preparation and analysis of samples from patients with CRS or IBD

Human ethmoid sinus mucosa from chronic rhinosinusitis (CRS) patients (n = 25) were collected during endoscopic sinus surgery under general anesthesia between January 2021 and April 2021 in the department of Otorhinolaryngology at Severance Hospital in Yonsei University College of Medicine. This study was approved by the Institutional Review Board of the Yonsei University College of Medicine (IRB no. 4-2016-0902). Patients were diagnosed with CRS according to the European position paper on rhinosinusitis and nasal polyps 2020 guidelines[78]. Paranasal sinus CT findings of patients were evaluated using the Lund-Mackay score (LMS), which ranges from 0 to 24, and patients with LMS larger than 10 (n = 12) were classified as those having moderate to severe CRS[79]. Half of the ethmoid mucosa samples were used for flow cytometry while the other half were subjected to immunofluorescence staining as described above.

We investigated the protein expression ratio of CD9 or CD39 to CD45 in the colon mucosa of 14 IBD patients, including ulcerative colitis

(UC; n=7) and Crohn's disease (CD; n=7), along with healthy controls (HC; n=7), using the proteome data we previously reported[80,81]. For immunofluorescence staining, colon samples were obtained from HC (n = 8) and patients with UC (n = 5) and CD (n = 5). This study was approved by the Institutional Review Board of Yonsei University College of Medicine (IRB No: 2012-0039-030). The colon mucosa samples were fixed in paraffin block and subjected to immunofluorescence staining, as described above.

X. Human ethmoid mucosa single-cell dissociation

Human ethmoid mucosa biopsies were collected in DMEM-F12 (Lonza) supplemented with 1% P/S. The tissues were transferred to 6-well plates and chopped into small pieces, and then dissociated using 5% collagenase type II and 0.1 M calcium chloride dihydrate in 5 ml of HBSS at 37°C for 1 h. The dissociated cells were strained and processed to remove the RBCs. Next, the samples were used for flow cytometry as described above.

Y. Statistical analysis

Comparisons of samples between two groups were processed by an unpaired Student's t-test. However, when the data do not meet the normality assumption due to the small sample size (Fig. 8c, d, f, g), the samples were compared between two groups using a Mann-Whitney test. On the other hand, for comparison of samples among multiple groups, we performed one-way ANOVA with Tukey's post hoc correction. Furthermore, for comparisons of samples among multiple groups defined by two variables (e.g., time point and experimental condition in Fig. 1g), we performed two-way ANOVA with Sidak's post hoc correction. The

statistical significance cutoff of $P < 0.05$ was used. All statistical analyses were performed using the GraphPad PRISM 8 software (GraphPad, San Diego, CA, USA). For all graphs, data are displayed as mean ± s.e.m. All these pieces of information are indicated in the figure legends.

III. RESULTS

Part 1. Alveolar macrophage recruitment is responsible for attenuation of neutrophilic inflammation upon *Staphylococcus aureus* (*S. aureus*) infection

1. NOX4 is responsible for attenuation of lung inflammation at 24 h after *S. aureus* lung infection

To identify the immunologic role of NOX4 in bacterial lung infection, we examined the concentration of BALF proteins as a lung injury index in WT or NOX4 KO mice after *S. aureus* lung infection. In WT mice, BALF protein levels significantly increased at 12 h and then subsequently decreased until 120 h after infection. Conversely, in NOX4 KO mice, BALF protein levels exhibited a significant increase at 12 h, remained elevated at 24 h, and then decreased until 120 h after infection (Fig. 1A). Notably, although the levels in NOX4 KO mice were similar to those in WT mice at 12 h, they were three times higher than those in WT mice at 24 h (Fig. 1A). Furthermore, BALF protein levels showed a decline in WT mice after 12 h and in NOX4 KO mice after 24 h. Importantly, these levels tended to be higher in NOX4 KO mice than in WT mice from 48 h to 120 h after infection, although these differences did not reach statistical significance (Fig. 1A). To determine whether the lung injury in NOX4 KO mice was accompanied by an increased bacterial burden after infection, we quantified the number of remaining bacteria in BALF. The bacterial burden in BALF increased at 12 h and subsequently decreased until 120 h in WT mice (Fig. 1B). However, in contrast to the pattern of BALF protein levels, there was no discernible difference in bacterial burden between WT and NOX4 KO mice up to 120 h after infection (Fig. 1B). The levels of TNFα, a pro-inflammatory cytokine, increased at 12 h and subsequently decreased until 120 h in WT mice (Fig. 1C). Notably, at 24 h, TNFα levels were

significantly higher in NOX4 KO mice than in WT mice (Fig. 1C). Therefore, these results showed that NOX4 KO mice had more inflammation than WT mice at 24 h after infection, and the increased inflammation was not derived from the difference in bacterial load.

Next, we investigated H&E staining images to identify the invasion of cells into the lung after *S. aureus* infection. The inflammatory score, based on H&E staining, indicated that immune cell infiltration in lung tissues peaked at 24 h after infection and then gradually decreased until 120 h in both WT and NOX4 KO mice (Fig. 1D and E). Moreover, NOX4 KO mice exhibited more extensive immune cell infiltration than WT mice at 24 h after infection (Fig. 1D and E). Furthermore, we performed immunofluorescence staining of neutrophils (Ly6G) and macrophages (F4/80) to examine the infiltrated cell types in the lung after infection (Fig. 1F-H). The immunofluorescence staining of neutrophils displayed a pattern similar to that observed in the H&E staining (Fig. 1E and G). At 24 h after infection, NOX4 KO mice exhibited significantly higher neutrophil infiltration into the lung compared to WT mice (Fig. 1F and G). However, the infiltration of macrophages was not as extensive as that of neutrophils, and there were no discernible differences between WT and NOX4 KO mice after infection (Fig. 1F and H). These results suggest that NOX4 is responsible for attenuation of neutrophilic inflammation at 24 h after *S. aureus* lung infection. Furthermore, the inflammation induced by *S. aureus* was resolved more rapidly in WT mice than in NOX4 KO mice from 24 to 120 h, implying that the absence of NOX4 delayed the resolution of inflammation.

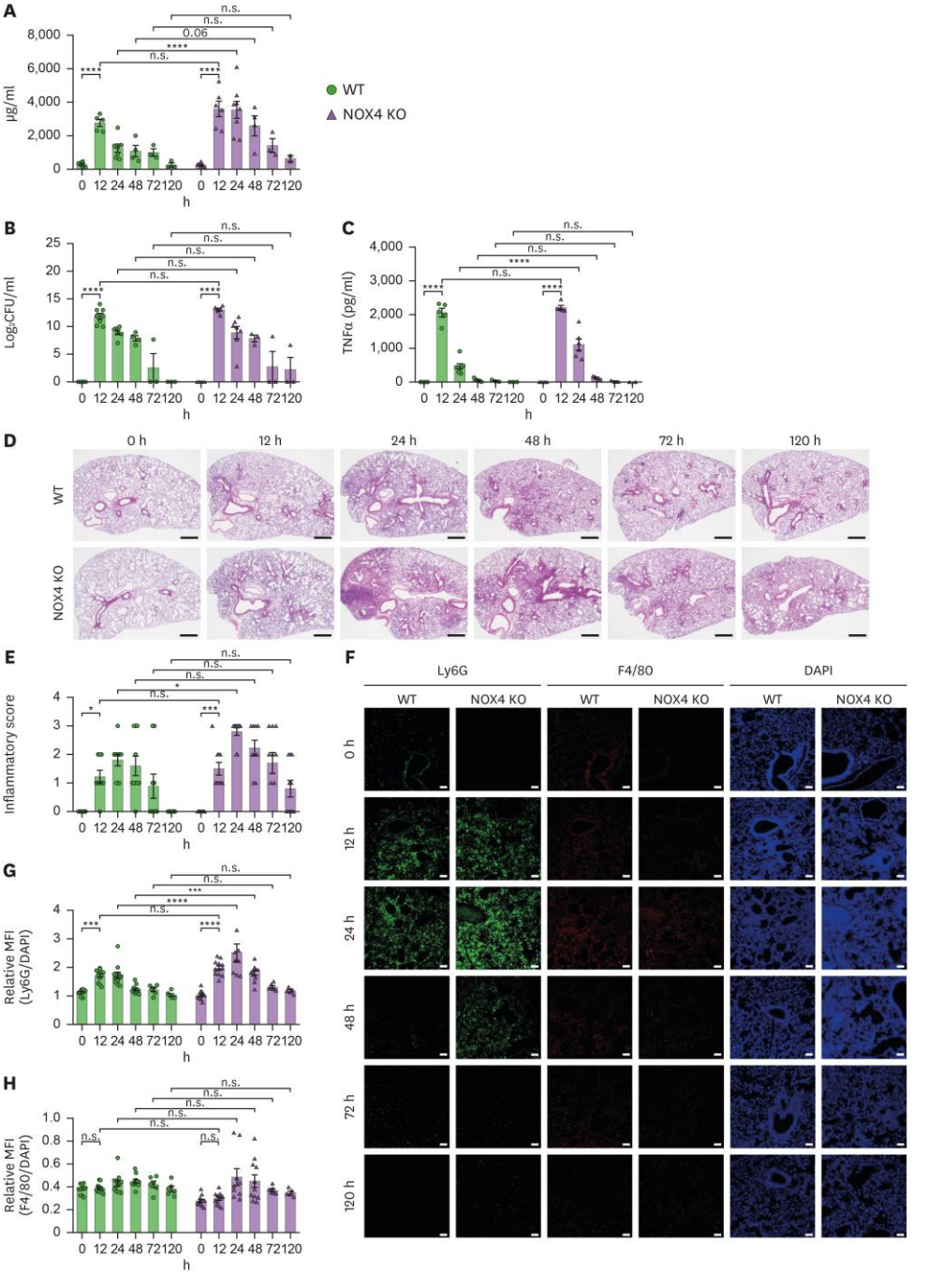

Figure 1. NOX4 is responsible for attenuation of lung inflammation at 24 h after *S. aureus* lung infection (n=2–9). WT and NOX4 KO mice were intranasally infected with *S. aureus* (3×10^7 CFU) until 120 h. (A) Protein concentration in BALF after infection. (B) *S. aureus* CFU in the BALF. (C) Concentration of TNFα in the BALF. (D) Representative H&E images and (E) inflammatory scores of lung tissue (scale bar=500 μm). (F) Representative immunofluorescence staining images of Ly6G (green), F4/80 (red), and DAPI (blue). MFI of (G) Ly6G or (H) F4/80 relative to DAPI (scale bar=100 μm). All data were presented as mean ± SEM. The p-value using a two-way ANOVA (A-C, E, G, H). $^{*}p<0.05$, $^{**}p<0.01$, $^{***}p<0.001$, $^{****}p<0.0001$.

2. NOX4 is responsible for AM recruitment at 24 h after *S. aureus* lung infection

Next, we examined the number of total cells in BALF in WT or NOX4 KO mice at 12 h and 24 h after *S. aureus* lung infection because NOX4 KO mice showed higher inflammation than WT mice at 24 h after infection. The number of cells in BALF increased in both WT and NOX4 KO mice at 12 h (Fig. 2A). Even though infiltrated cells in BALF were similar between WT and NOX4 KO mice at 12 h, the recruited cells in NOX4 KO mice were two times higher than those in WT mice at 24 h (Fig. 2A). Next, we performed flow cytometry analysis to examine the infiltrated cell types in the BALF after infection (Fig. 3). In BALF from NOX4 KO mice, the number of neutrophils is almost the same as that of total cells (Fig. 2A and B), and the percentage of neutrophils was almost 80% of total cells at 24 h after infection (Fig. 4A). Moreover, the number of neutrophils in NOX4 KO mice was similar to that in WT mice at 12 h, whereas the cells in NOX4 KO mice were three times higher than those in WT mice at 24 h (Fig. 2B). Although the number of monocytes and monocyte-derived macrophages was too small compared to that of neutrophils, the number of these cells increased in WT mice at 12 and 24 h after infection (Fig. 2C). In contrast, in NOX4 KO mice, the number of these cells increased at 12 h but decreased at 24 h (Fig. 2C). Furthermore, NOX4 KO mice had a lower count of these cells than WT mice at 24 h after infection (Fig. 2C). However, the percentages of monocytes and monocyte-derived macrophages did not exhibit significantly increases at 12 h in either WT or NOX4 KO mice (Fig. 4B and C). Nevertheless, at 24 h after infection, the percentages of these cells were lower in NOX4 KO mice than in WT mice (Fig. 4B and C). These findings suggest that the neutrophil population is the main cellular type that is infiltrated in NOX4 KO mice's lungs, as well as that the neutrophil population is sustained in NOX4 KO mice at 24 h following infection.

AMs have been reported to be differentiated from monocytes[11] and to play an important role in the early host response to bacterial lung infections by regulating the inflammatory response, removing neutrophils, and promoting tissue repair[12,82]. Therefore, we checked the number of AMs in WT or NOX4 KO mice at 12 and 24 h after *S. aureus* infection (Fig. 2D). The number of AMs in BALF was similar between WT and NOX4 KO mice in the absence of infection. At 12 h after infection, the number of AMs in both WT and NOX4 KO mice was almost the same. Interestingly, the number of AMs decreased in NOX4 KO mice compared to that in WT mice at 24 h after infection (Fig. 2D). Following infection, the total cell count in BALF increased due to inflammation, mainly attributed to the recruitment of neutrophils (Fig. 2A and B, Fig. 4A). Consequently, the percentage of AMs in BALF appeared to decrease at 12 and 24 h after infection (Fig. 2E). Although it may appear that the percentage of AMs decreases at 12 and 24 h, it was significantly lower in NOX4 KO mice than in WT mice at 24 h after infection (Fig. 2E). To investigate the cause of the reduction of AMs in NOX4 KO mice after infection, we examined *in vivo* flow cytometry-based apoptosis analysis (Annexin V & DAPI) in AM population. The percentage of necrotic cells (Annexin V^+ $DAPI^+$) in AMs increased in WT mice at 12 and 24 h after infection (Fig. 2F). The percentage of necrotic cells in AMs was comparable between WT and NOX4 KO mice at 12 and 24 h after infection (Fig. 2F). Therefore, the reduction of AM in NOX4 KO mice at 24 h after infection was not due to increasing cell death. These results indicated that NOX4 is responsible for AM recruitment into the lung at 24 h after *S. aureus* lung infection. Moreover, the increased level of lung injury and neutrophil number in NOX4 KO mice at 24 h after *S. aureus* infection may be attributed to the decreased level of AMs in NOX4 KO mice at 24 h after infection.

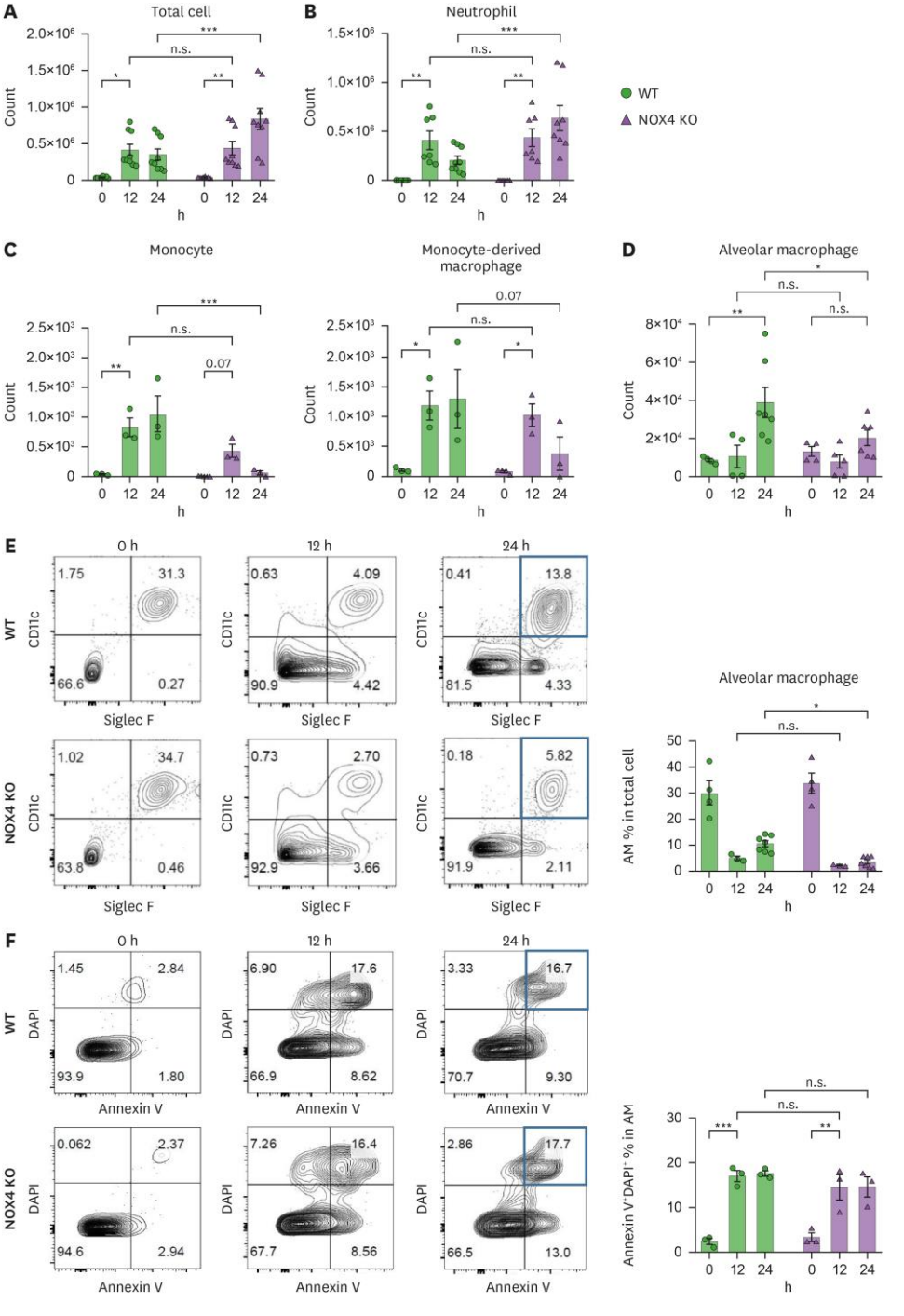

Figure 2. NOX4 is responsible for alveolar macrophage recruitment at 24 h after *S. aureus* lung infection (n=3–9). WT and NOX4 KO mice were intranasally infected with *S. aureus* (3×10^7 CFU). (A) Total cell and (B) neutrophil counts ($CD45^+CD11b^+CD11c^-Ly6G^+$ $SiglecF^-$) in BALF. (C) Monocyte (left; $CD45^+CD11b^+CD11c^-Ly6G^-SiglecF^-CD64^+F4/80^-$) and monocyte- derived macrophage (right, $CD45^+CD11b^+CD11c^-Ly6G^-SiglecF^-CD64^+F4/80^+$) counts in BALF. (D) AM counts ($CD45^+CD11c^+$ $SiglecF^+$). (E) Gate and percentages of AM in BALF. (F) Gate and Percentage of Annexin V^+DAPI^+ in AM gate ($CD45^+CD11c^+SiglecF^+$). The data showed three or more experiments, as in the symbol indicating individual mice. All data were presented as mean ± SEM. The p-value using a two-way ANOVA (A-F). $^*p<0.05$, $^{**}p<0.01$, $^{***}p<0.001$, $^{****}p<0.0001$.

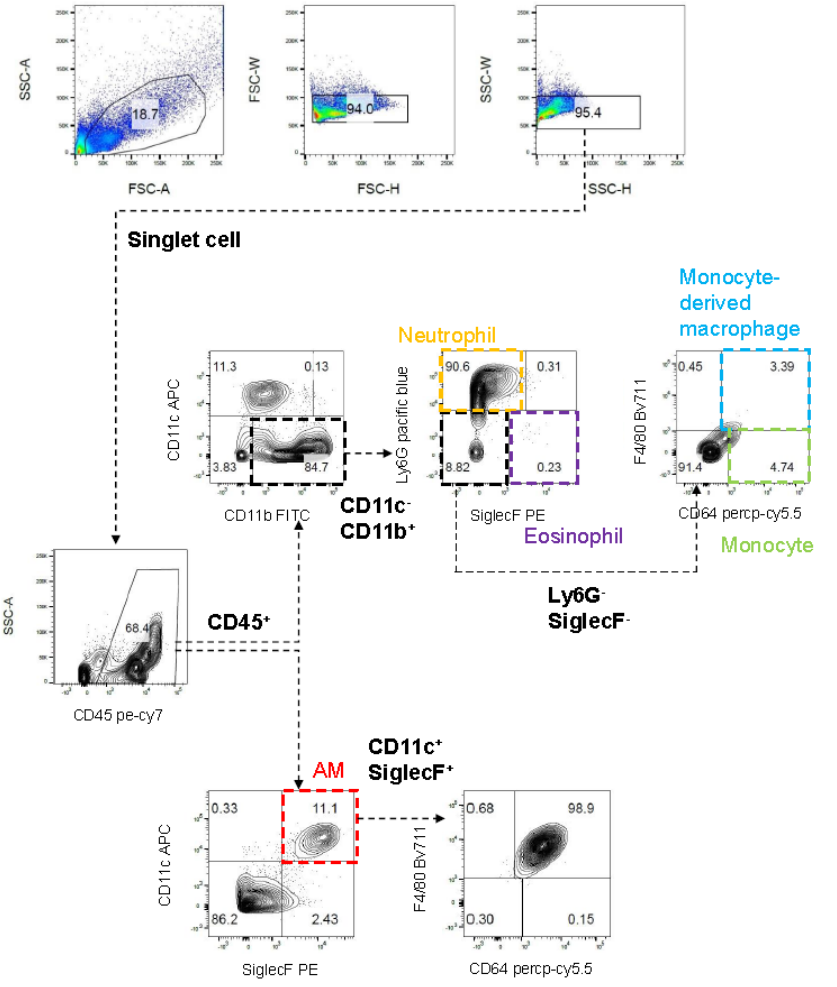

Figure 3. The gating strategy for isolating immune cells in BALF. The gating strategy defined the neutrophil ($CD45^+CD11b^+CD11c^-$ $Ly6G^+SiglecF^-$), eosinophil ($CD45^+CD11b^+CD11c^-Ly6G^-SiglecF^+$), monocyte ($CD45^+CD11b^+CD11c^-Ly6G^-SiglecF^-CD64^+F4/80^-$), mono cyte-derived macrophage ($CD45^+CD11b^+CD11c^-Ly6G^-SiglecF^-CD64^+F4/80^+$), and AM ($CD45^+CD11c^+SiglecF^+CD64^+F4/80^+$) populations.

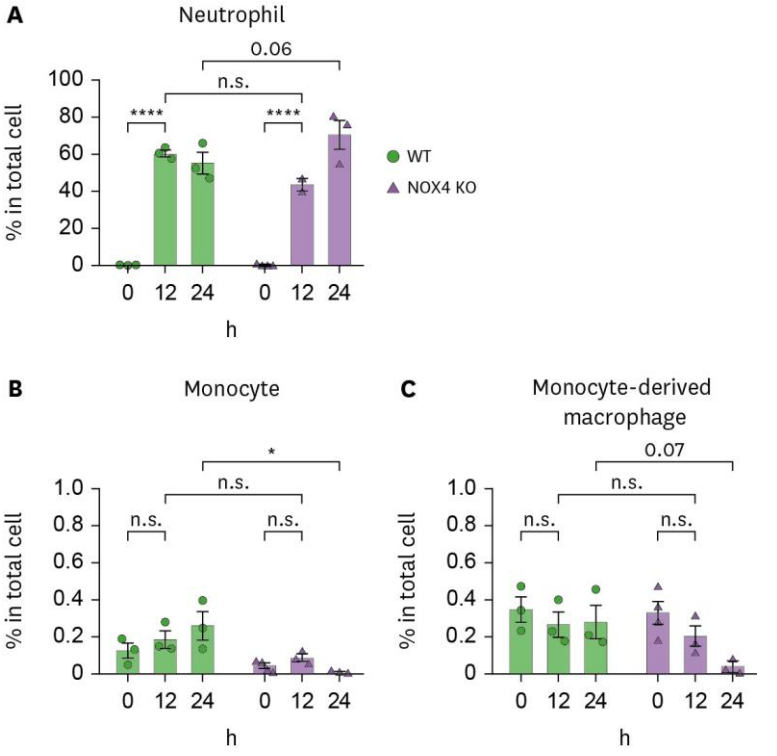

Figure 4. The frequency of immune cells in BALF after *S. aureus* lung infection (n=3). WT and NOX4 KO mice were intranasally infected with *S. aureus* (3×10^7 CFU). (A) Percentages of neutrophil population ($CD45^+CD11b^+CD11c^-Ly6G^+SiglecF^-$). (B) Percentages of monocyte population ($CD45^+CD11b^+CD11c^-Ly6G^-SiglecF^-CD64^+F4/80^-$). (C) Percentages of monocyte-derived macrophage population ($CD45^+CD11b^+CD11c^-Ly6G^-SiglecF^-CD64^+F4/80^+$). The data showed two or more experiments, as in the symbol indicating individual mice. All data were presented as mean ± SEM. The p-value using a two-way ANOVA (A-C). $^*p<0.05$, $^{****}p<0.0001$.

3. NOX4 is not involved in the antibacterial activity of neutrophils and AMs upon *S. aureus* infection

We questioned whether intrinsic NOX4 affected the function of neutrophils after *S. aureus* infection. To investigate the phagocytic capacity of neutrophils, we isolated bone-marrow derived neutrophils (BMDN) from WT or NOX4 KO mice using MACS. In BMDN from WT and NOX4 KO mice, there were no differences in the uptake of GFP-tagged *S. aureus* at different time points within 1 h (Fig. 5A). The percentages of apoptotic and necrotic cell death were also similar in both WT and NOX4 KO BMDN after GFP-tagged *S. aureus* infection (Fig. 5B and C). Moreover, BMDN isolated from both WT and NOX4 KO mice exhibited similar bacterial killing ability with MOI 5 or 20 at 30 min (Fig. 5D).

Next, we investigated whether intrinsic NOX4 directly influenced the function of AMs after infection. To examine the phagocytic capacity and killing ability of AMs, we isolated them from WT or NOX4 KO mice using FACS. AMs from WT or NOX4 KO mice showed similar patterns in bacterial uptake and bacterial killing ability at different time points and doses (Fig. 5E and F). Additionally, we conducted *ex vivo* flow cytometry-based apoptosis analysis (Annexin V & PI) in AMs with *S. aureus* (MOI 10). AMs isolated from WT or NOX4 KO mice exhibited that no significant differences in necrotic cell death in response to *S. aureus* infection (Fig. 5G). These findings suggest that intrinsic NOX4 has no discernible effect on neutrophil and AM function, including antibacterial activity and cell death, in response to *S. aureus* infection.

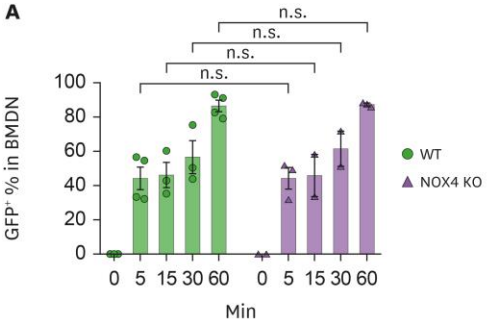

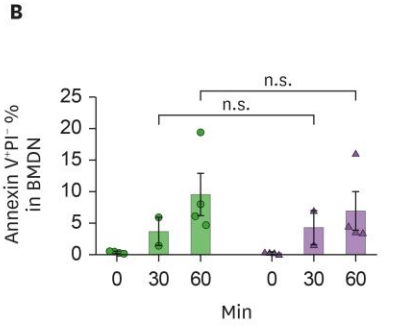

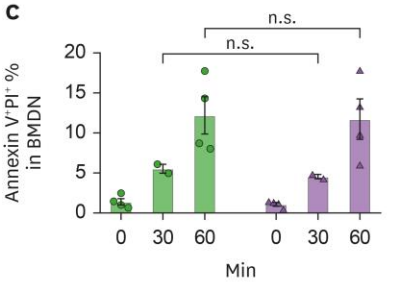

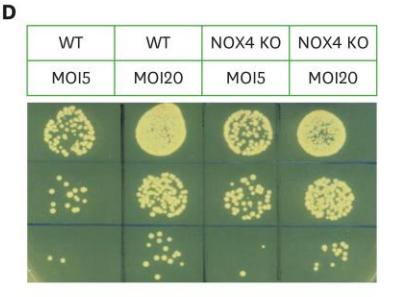

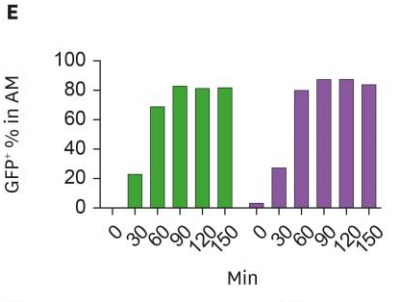

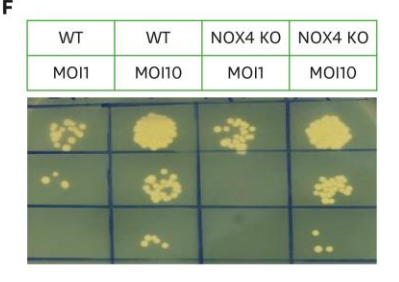

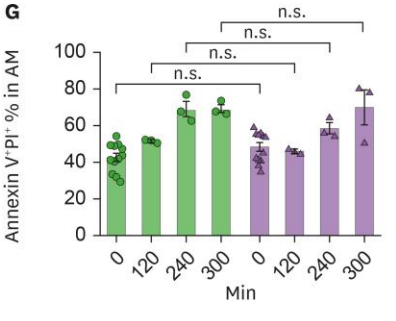

Figure 5. NOX4 is not involved in the antibacterial activity of neutrophils and AMs upon *S. aureus* infection. (A-D) *Ex vivo* BMDNs from WT or NOX4 KO mice were infected with *S. aureus* at the indicated time point. (A) Percentages of GFP^+ BMDNs with MOI 10. (B) Percentages of apoptotic cells (Annexin V^+PI^-) in BMDNs with MOI 10. (C) Percentage of necrotic cells (Annexin V^+PI^+) in BMDNs with MOI 10. (D) *S. aureus* CFU in media with MOI 5 or 20 at 30 min after infection. (E-G) *Ex vivo* AMs from WT or NOX4 KO mice were infected with *S. aureus*. (E) Percentages of GFP^+ AMs after infection with MOI 1. (F) *S. aureus* CFU in media at 60 min after infection with MOI 1 or 10. (G) Percentage of necrotic cells (Annexin V^+PI^+) in AMs with MOI 10. All data were presented as mean ± SEM. Two-way ANOVA (A-C, G).

4. NOX4 is necessary to induce ICAM1 expression on endothelial cells after *S. aureus* infection

Given that NOX4 is not intrinsically involved in the antibacterial activity of neutrophils and AMs, we hypothesized that NOX4 could operate in cells other than neutrophils and AMs to control their numbers upon *S. aureus* infection. Since NOX4 is reported to be expressed in lung endothelial cells[23,25], and lung endothelium is responsible for monocyte recruitment from blood to alveoli[9,83], we focused on the role of NOX4 in lung endothelial cells upon *S. aureus* infection. We isolated lung $CD31^+$ endothelial cells from WT or NOX4 KO mice using MACS and examined the expression of NOX4 after *S. aureus* infection. In the WT endothelial cell, we observed a significant increase in NOX4 gene expression at 12 h, followed by a decrease at 24 h after infection (Fig. 6A). To investigate whether NOX4 in endothelial cells could be involved in the recruitment of AMs into the lung after infection, we examined the expression level of endothelial adhesion molecules such as ICAM1 which are known to play an important role in monocyte recruitment on endothelial cells[9,83]. The level of ICAM1 mRNA expression in WT mice endothelial cells increased at 12 h and decreased at 24 h after *S. aureus* infection (Fig. 6B), which were similar patterns to NOX4 expression (Fig. 6A). Interestingly, the mRNA expression level of ICAM1 in endothelial cells from NOX4 KO mice was lower than that in endothelial cells from WT mice at 12 h after infection (Fig. 6B). Similar to the alteration pattern of mRNA expression, the protein level of ICAM1 in NOX4 KO mice endothelial cells was lower than that in WT mice endothelial cells at 12 h after infection (Fig. 6C). The protein level of vascular cell adhesion molecule-1 was also known to be associated with monocyte recruitment[10,84]. However, there was no difference in the protein level of VCAM1 in the endothelial cells from WT and NOX4 KO mice after infection (Fig. 6C). Taken together, we showed that NOX4 is necessary to induce the

expression of ICAM1, but not VACM1, in endothelial cells upon *S. aureus* infection, suggesting that NOX4 might induce recruitment of AMs by controlling ICAM1 expression in lung endothelial cells.

Previous studies have reported that VEGF can induce ICAM1 expression in various endothelial cells[85-87], and that NOX4 colocalizes with and interacts with a VEGF receptor 2 (VEGFR2) in the endothelium[88]. Furthermore, NOX4 can stabilize VEGFR2 and promote endothelial cell function[89]. These reports suggest that VEGF may regulate NOX4-mediated ICAM1 expression in endothelial cells after *S. aureus* infection. Thus, we investigate whether VEGF regulates the ICAM1 expression by NOX4. We first inactivated NOX4 activity using GLX351322, NOX4 inhibitor, in a stable human endothelial cell line such as Ea.hy926 cells. We next measured ICAM1 expression at 3 and 6 h after treatment with $rhVEGF_{165}$ in the presence or absence of GLX35122. At 6 h after $rhVEGF_{165}$ treatment, ICAM1 expression increased, and increased ICAM1 expression was reduced by GLX35122 treatment (Fig. 6D), indicating that VEGF can induce endothelial ICAM1 expression in a NOX4-dependent manner.

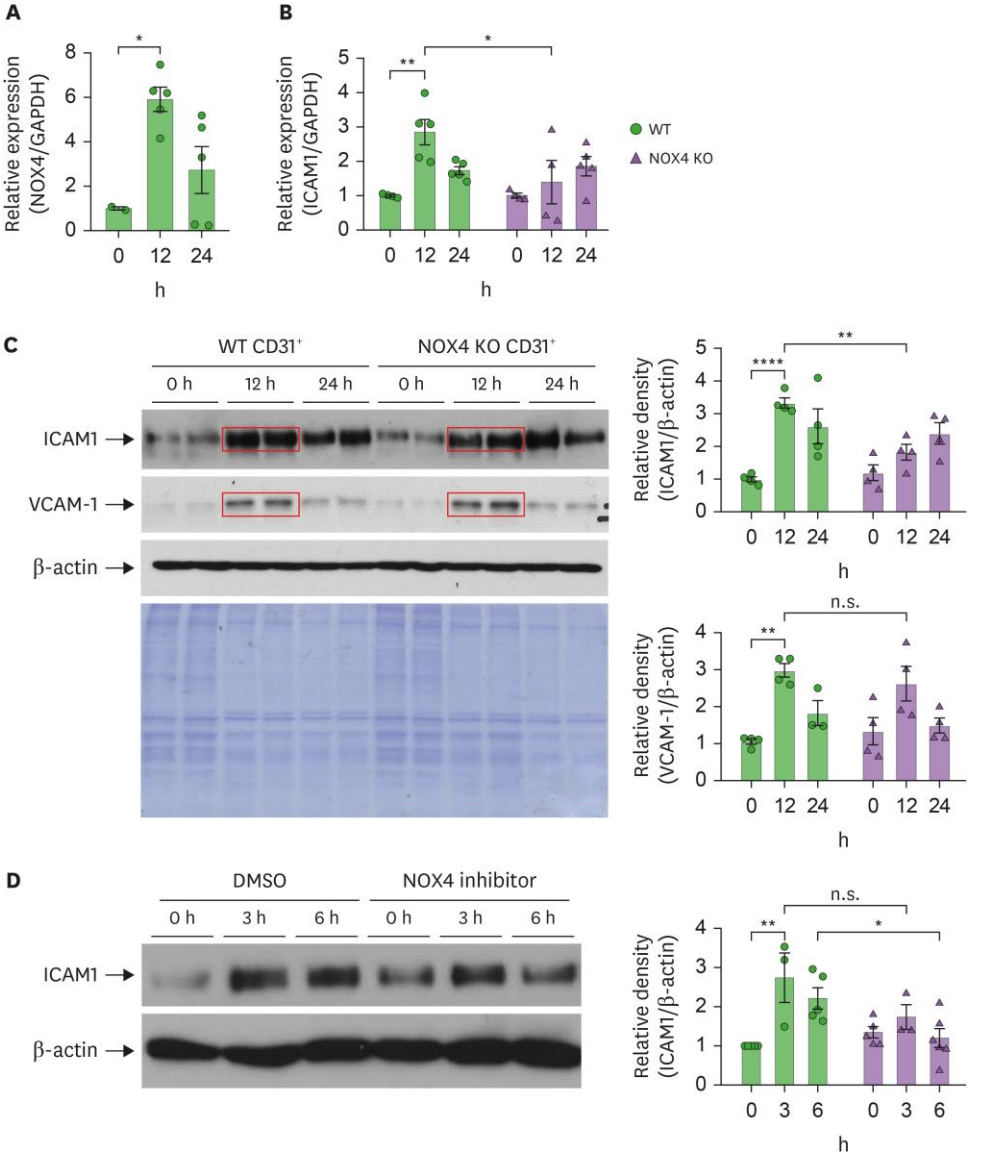

Figure 6. NOX4 is necessary to induce ICAM1 expression on endothelial cells after *S. aureus* infection (n=3–5). (A-C) $CD31^+$ endothelial cells were isolated using MACS from WT or NOX4 KO mice lungs at 0, 12, and 24 h after *S. aureus* infection. (A) Expression of NOX4 mRNA in $CD31^+$ endothelial cells. (B) Expression of ICAM1 mRNA in endothelial cells by real-time PCR. (C) Immunoblot of ICAM1, VCAM-1, β-actin, and Coomassie staining. Representative image (left) and relative density quantified from immunoblot (right). (D) Ea.hy926 cells were pretreated with 10 μM GLX351322 to inhibit NOX4 prior to $rhVEGF_{165}$ treatment. Immunoblot of ICAM1. Representative image (left) and relative density quantified from immunoblot (right). All data were presented as mean ± SEM. The p-value using a one-way ANOVA (A) and two-way ANOVA (B-D). $^{*}p<0.05$, $^{**}p<0.01$, $^{****}p<0.0001$.

5. VEGF attenuates lung inflammation via inducing AM recruitment after *S. aureus* infection

We wondered whether VEGF is induced in WT mice upon *S. aureus* infection. Therefore, we examined the concentration of VEGF in BALF after *S. aureus* infection. We found that the level of VEGF was increased at 12 h and decreased at 24 h after lung infection in WT mice (Fig. 7A). In addition, the increased level of VEGF in NOX4 KO mice was almost the same as that in WT mice (Fig. 7A), indicating that VEGF is increased upon *S. aureus* infection in a NOX4-independent manner.

Next, we investigated the functional role of VEGF in AM recruitment upon *S. aureus* infection. To test this, we intranasally treated WT and NOX4 KO mice with anti-VEGF Abs together with *S. aureus* to block local VEGF in alveoli. We then examined the ratio and number of AMs in BALF at 24 h post-infection in the presence of control IgG or anti-VEGF Abs. Anti-VEGF treatment significantly reduced the ratio and number of AMs in WT mice, which were similar to those in IgG-treated NOX4 KO mice (Fig. 7B and C). Furthermore, the ratio and number of AMs in IgG-treated NOX4 KO mice did not differ from those in anti-VEGF-treated NOX4 KO mice (Fig. 7B and C). These results suggest that VEGF, increased by *S. aureus* infection, can recruit AMs in NOX4-dependent manner. In this context, we wondered whether increased VEGF is responsible for the attenuation of neutrophilic inflammation and lung injury upon *S. aureus* infection. Anti-VEGF treatment increased the levels of BALF protein (Fig. 7D), BALF cells (Fig. 7E), and neutrophils (Fig. 7F) in WT mice, which were similar to those in IgG- or anti-VEGF-treated NOX4 KO mice (Fig. 7D-F). However, bacterial loads were not affected in all groups (fig. 7G). Taken together, our results demonstrate that VEGF in the alveoli is essential for protecting against *S. aureus* infection by recruiting AMs in NOX4-dependent manner.

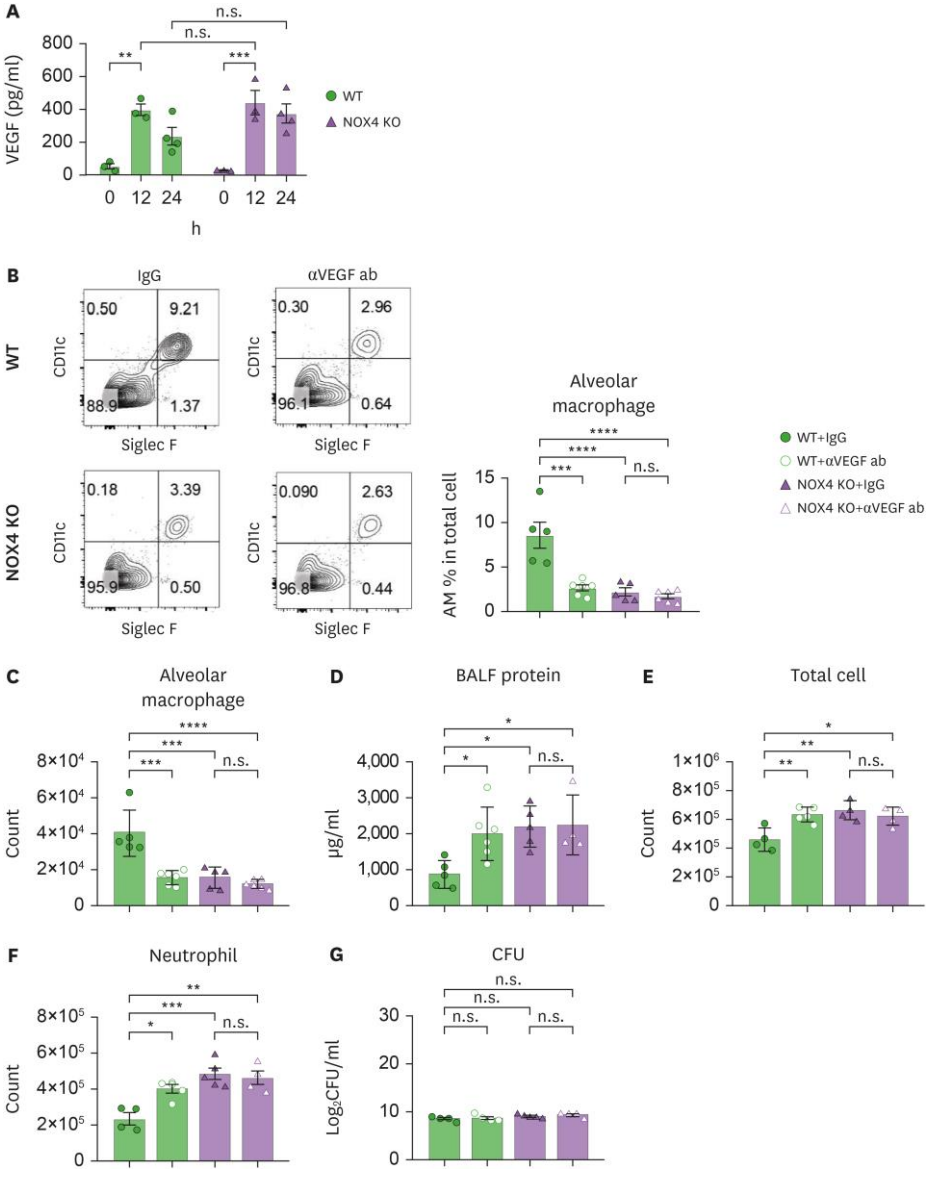

Figure 7. VEGF attenuates lung inflammation via inducing AM recruitment at 24 h after *S. aureus* lung infection (n=3–6). (A) VEGF concentration in BALF from WT and NOX4 KO mice. (B-G) WT and NOX4 KO mice intranasally treated with IgG or anti-VEGF Abs, and they were infected with 3×10^7 CFU of *S. aureus* at the same time. The inflammatory responses were assessed at 24 h after the infection. (B) Representative flow cytometry plots (left), and percentages of AM in total BALF cell (right). (C) AM counts in BALF. (D) Protein concentration in BALF. (E) Total cell counts in BALF. (F), neutrophil counts in BALF. (G) *S. aureus* CFU in BALF. The data showed 3 experiments, with the symbol representing individual mice. All data were presented as mean ± SEM. The p-value using two-way ANOVA (A) and one-way ANOVA (B-G). $^{*}p<0.05$, $^{**}p<0.01$, $^{***}p<0.001$, $^{****}p<0.0001$.

6. NOX4 attenuates lung inflammation via inducing AM recruitment after *S. aureus* infection

To investigate the functional role of AMs in neutrophilic inflammation and lung injury upon *S. aureus* infection, we intranasally treated mice with clodronate liposome to deplete AMs at 48 h prior to *S. aureus* infection[90]. Clodronate liposome treatment significantly reduced the ratio and number of AMs in WT mice, similar to those in isotype liposome-treated NOX4 KO mice (Fig. 8A and B). Moreover, the ratio and number of AMs in isotype liposome-treated NOX4 KO mice were not different from those in clodronate liposome-treated NOX4 KO mice (Fig. 8A and B). Clodronate liposome treatment increased the levels of BALF protein (Fig. 8C), BALF cells (Fig. 8D), and neutrophils (Fig. 8E) in WT mice, similar to those in isotype liposome- or clodronate liposome-treated NOX4 KO mice (Fig. 8C-E). However, bacterial loads were not affected in all groups (Fig. 8F). These results demonstrate that AM recruitment is required for the resolution of neutrophilic inflammation in a NOX4-dependent manner after *S. aureus* infection.

In this study, *S. aureus* lung infection simulates the production of VEGF in alveoli. When NOX4 is present, the elevated VEGF levels induce endothelial ICAM1 expression in a NOX4-dependent manner, facilitating the recruitment of AMs to the alveoli. These recruited AMs play a crucial role in reducing neutrophilic inflammation. However, in the absence of NOX4, increased VEGF is unable to significantly enhance endothelial ICAM1 expression, leading to insufficient recruitment of AMs to the alveoli. This deficiency in AMs results in excessive neutrophilic inflammation (Fig. 9).

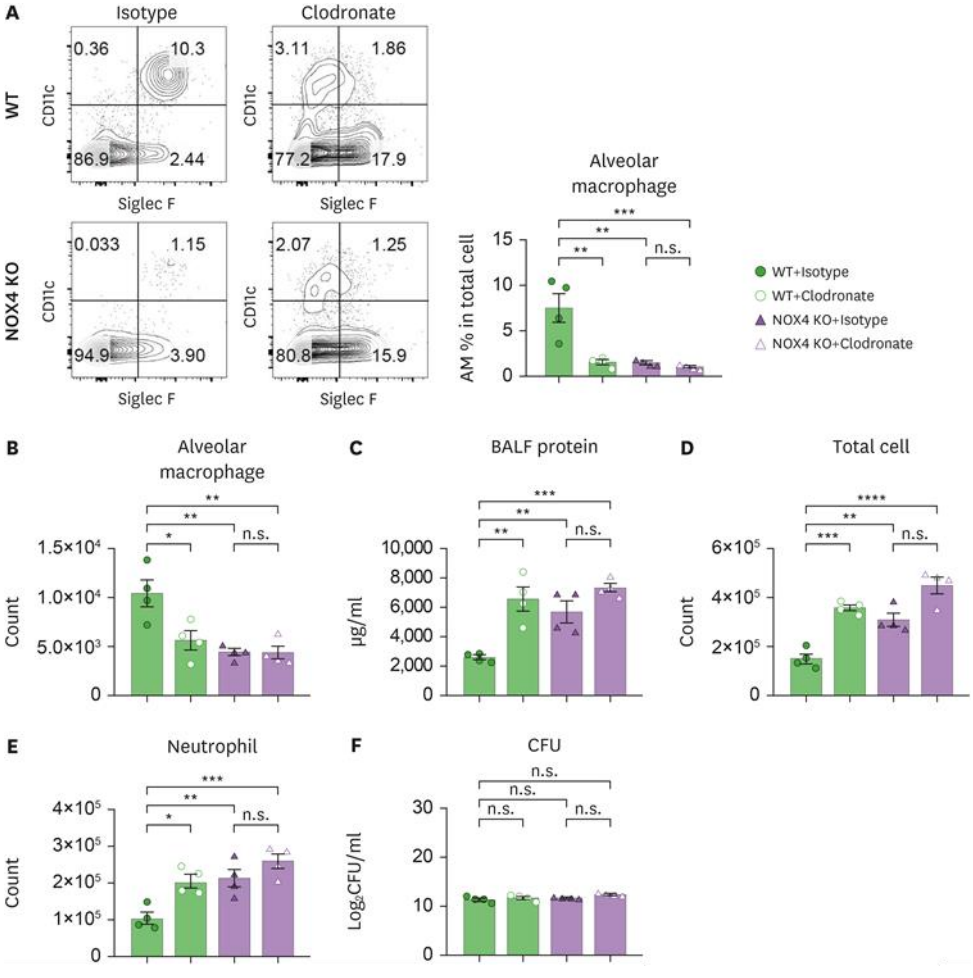

Figure 8. NOX4 attenuates lung inflammation via inducing AM recruitment at 24 h after *S. aureus* lung infection (n=4–6). WT and NOX4 KO mice were intranasally administrated with clodronate liposome or isotype liposome 48 h before *S. aureus* infection. They were infected with *S. aureus* (3×10^7 CFU) and sacrificed after 24 h. (A) Representative flow-cytometry plots (left), and percentages of AM in BALF cells (right). (B) AM counts in BALF. (C) Protein concentration in BALF. (D) Total cell counts and (E) neutrophil counts in BALF. (F) *S. aureus* CFU in BALF. The data showed two or more experiments, as in the symbol indicating individual mice. Bars represented means ± SEM. The p-value using one-way ANOVA was used for (A-F). $^{*}p<0.05$, $^{**}p<0.01$, $^{***}p<0.001$, $^{****}p<0.0001$.

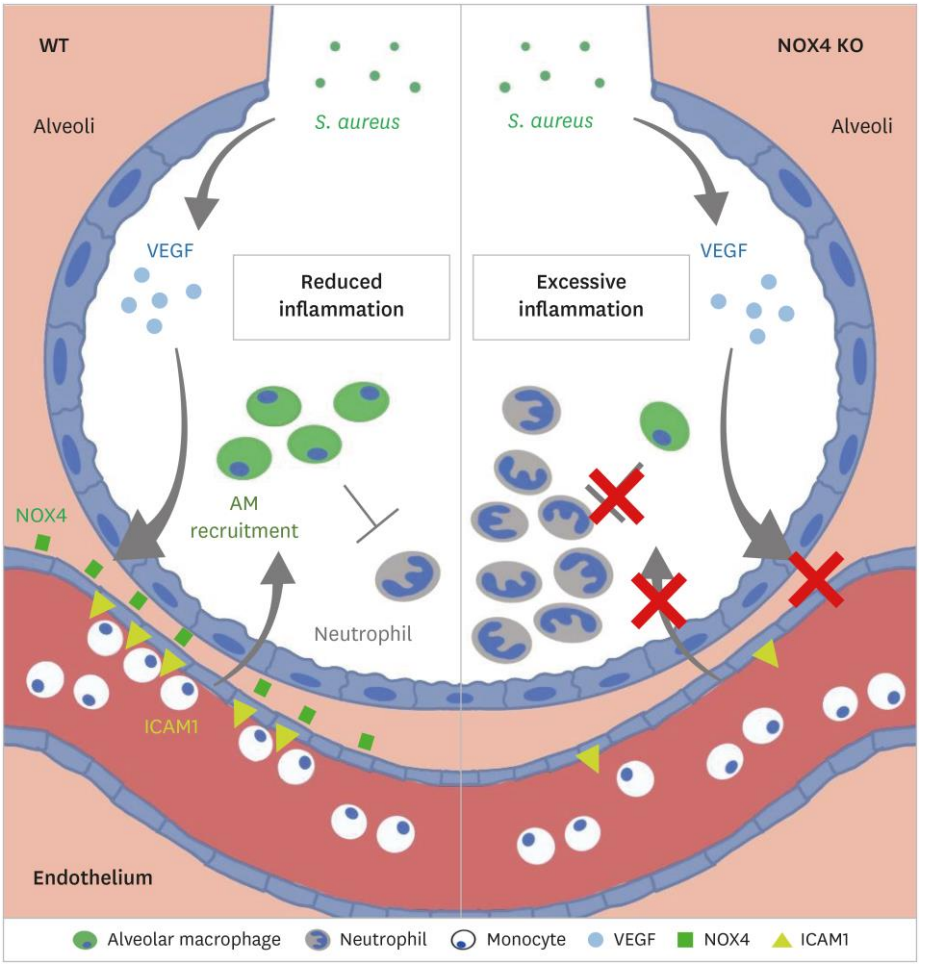

Figure 9. Schematic of the study. *S. aureus* lung infection triggers the production of VEGF in the alveoli. In WT mice, elevated levels of VEGF can stimulate the expression of endothelial ICAM1 in a NOX4-dependent manner. Consequently, the AMs were recruited to the alveoli through the increased endothelial ICAM1, and they reduced neutrophilic inflammation. However, in NOX4 KO mice, the increased VEGF is not able to induce appropriate endothelial ICAM1 expression, resulting in insufficient AM recruitment in the alveoli. As a result, the insufficient AMs cause excessive neutrophilic inflammation.

Part 2. Distinctive CD39$^+$CD9$^+$ lung interstitial macrophages suppress IL-23/Th17-mediated neutrophilic asthma by inhibiting NETosis

1. IL-23 inhibitor suppresses Th17-mediated neutrophilic inflammation in NDA mouse lungs

To establish the ovalbumin (OVA)-driven neutrophil-dominant asthma (NDA) model, mice were sensitized with OVA (75 μg) and LPS (10 μg) on days 0, 1, 2, 7. Mice were then challenged at 7 days after the fourth sensitization with only OVA (100 μg) on days 14, 15, 21, 22, and sacrificed on day 24. The sensitization/challenge scheme is summarized in Fig. 1A. Total cell and neutrophil counts in the bronchoalveolar lavage fluid (BALF) were significantly increased in OVA+LPS/OVA than in phosphate-buffered saline (PBS)/PBS or OVA+LPS/PBS (Fig. 1B).

We next determined which T helper (Th) cells were predominantly activated in OVA+LPS/OVA through fluorescence-activated cell sorting (FACS) analysis using antibodies against RORγt (Th17), T-bet (Th1), and GATA3 (Th2). Although all three types of T cells were increased in OVA+LPS/OVA compared to in PBS/PBS or OVA+LPS/PBS, the increase of RORγt$^+$ T cells (~6x10^4 cells) was much higher than those of T-bet$^+$ (~1.5x10^4) and GATA3$^+$ T cells (~2x10^3) (Fig. 1C). Correspondingly, Th17-related cytokines (IL-17 and IL-22) were significantly increased in OVA+LPS/OVA compared to in PBS/PBS or OVA+LPS/PBS (Fig. 1D). Cytokines related to Th1 (IFN-γ) and Th2 (IL-5) were also increased, consistent with the increased T-bet$^+$ and GATA3$^+$ T cells. Moreover, hematoxylin and eosin (H&E)-stained lung sections showed the increased immune cell recruitment into lung tissue in OVA+LPS/OVA, compared to that in PBS/PBS or OVA+LPS/PBS (Fig. 1E, F). Furthermore, the enhanced pause (P_{enh}) using whole-body plethysmography (WBP) showed significantly higher P_{enh} values (i.e., worse respiratory function)

in OVA+LPS/OVA than in PBS/PBS or OVA+LPS/PBS (Fig. 1G), which was further confirmed by measuring R_{rs} values (i.e., respiratory resistance) using an invasive ventilated respiratory resistance method (Fig. 2A).

Next, we investigated the effects of Dexamethasone (Dex), a corticosteroid medication, on attenuation in our NDA model (Fig. 1A). Dex treatment had no significant effect on the increased counts of total cells and neutrophils in BALF (Fig. 1B), and RORγt^+ and T-bet$^+$ T cells in lung tissues in OVA+LPS/OVA, but attenuated the increase of GATA3$^+$ T cells (Fig. 1C). Dex treatment led to no changes in the increased IL-17 and IL-22 in OVA+LPS/OVA, but attenuated the increase of IFN-γ and IL-5 (Fig. 1D). Of note, the alteration pattern of IFN-γ was found to be inconsistent with that of T-bet$^+$ T cells after Dex treatment, indicating that IFN-γ is not entirely specific to T-bet$^+$ T cells, which may also explain its unexpected higher level in OVA+LPS/OVA. Immune cell infiltration (Fig. 1E, F) and P_{enh} (Fig. 1G) and R_{rs} values (Fig. 2A) were also not attenuated by Dex treatment. These results indicate that NDA mice are a Dex-resistant model with Th17 activation and neutrophilic inflammation.

IL-23 cytokine secreted from inflammatory DCs is critical for Th17 activation[41]. To test the contribution of IL-23 to Th17 activation and neutrophilic inflammation in NDA mice, we treated NDA mice with αIL-23p19 (Fig. 1A). The increased BALF cells and neutrophils in OVA+LPS/OVA were significantly reduced by αIL-23p19 (Fig. 1B). The increased RORγt^+, T-bet$^+$, and GATA3$^+$ T cells and levels of their cytokines (Fig. 1C, D), as well as the increased immune cell infiltration and P_{enh} and R_{rs} values (Fig. 1E-G and Fig. 2A), were also attenuated by αIL-23p19. These results indicate that IL-23 is required for Th17 activation, neutrophilic inflammation, and pathophysiology in OVA+LPS/OVA.

The above results collectively indicate that our NDA model induces neutrophil-dominant asthma, which is driven mainly by Th17 cell activation though mixed with Th1 and Th2 cell activation. To further verify the major contribution of Th17 cells to neutrophilic inflammation, we next inhibited the effect of Th17 cell activation by IL-17 neutralizing antibody (αIL-17) treatment in OVA+LPS/OVA. αIL-17 treatment significantly reduced the increased total cells and neutrophils (Fig. 1H and Fig. 2B) and cytokine (IL-17, IL-22, and IFN-γ) levels (Fig. 1I) in BALF, as well as the increased immune cell infiltration in lung tissues (Fig. 2C, D) and P_{enh} values (Fig. 2E), in OVA+LPS/OVA, thus supporting the major role of Th17 cells in neutrophilic inflammation in NDA model.

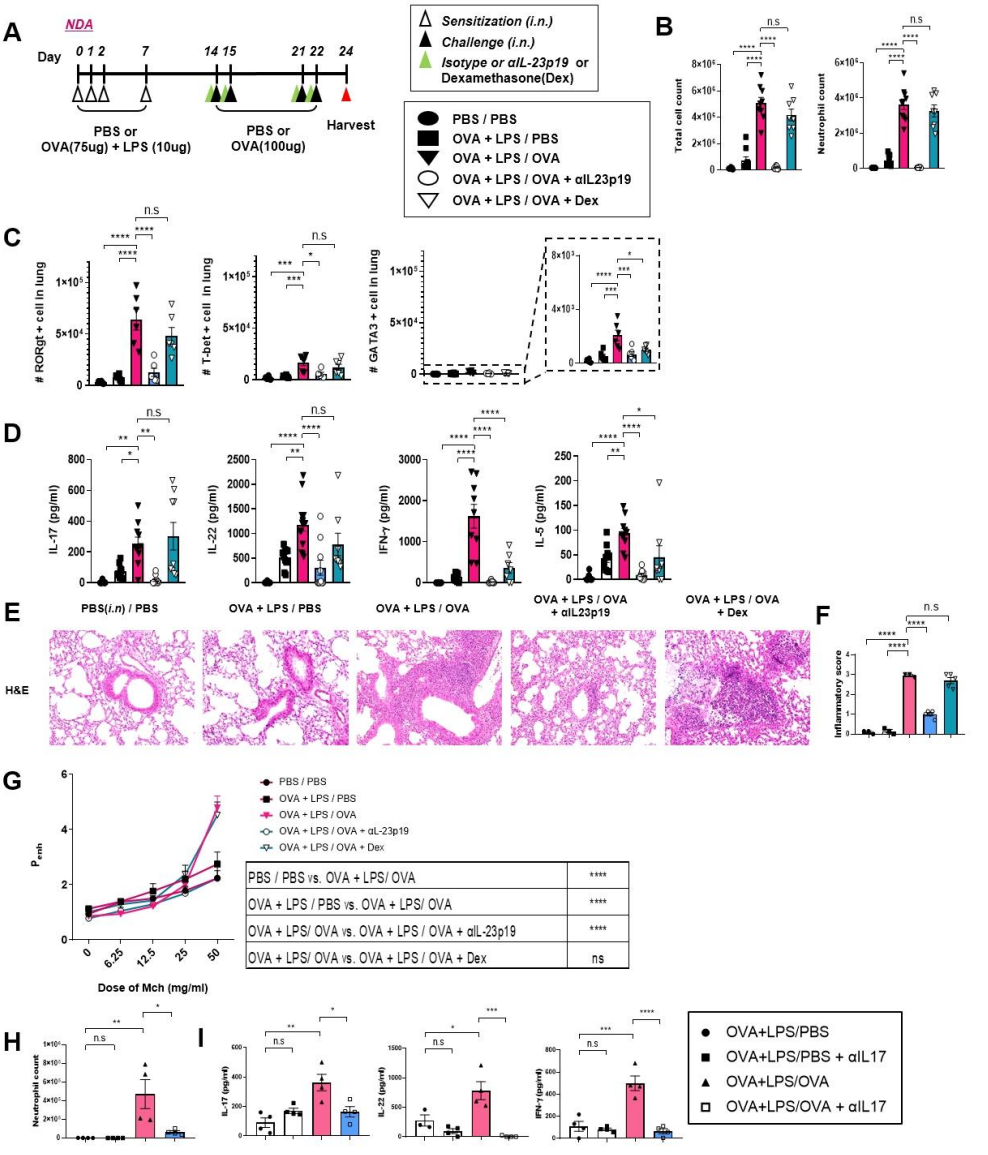

Figure 1. IL-23 inhibitor suppresses Th17-mediated neutrophilic inflammation in NDA mice. (A) Schematic diagram of allergen sensitization and challenge protocol. In NDA mouse model, sensitization with PBS or OVA+LPS intranasally (i.n.) was followed by challenge with PBS or OVA (i.n.) at the indicated days. Isotype control, αIL-23p19, or dexamethasone (Dex) was treated at 1 h before every challenge period. The inflammatory response was assessed at 48 h after the last challenge. (B) Total cell and neutrophil counts in BALF measured using flow cytometry. (C) $RORgt^+$, $T\text{-}bet^+$, and $GATA3^+$ cell counts in $CD4^+$ T cells ($Live,Dump^-FOXP3^-CD44^+CD4^+TCRb^+$) measured using flow cytometry. (D) Levels of Th17 (IL-17 and IL-22), Th1 (IFN-γ), and Th2 cell-related cytokines (IL-5) measured in BALF. (E) Representative hematoxylin and eosin (H&E) staining of lung section. (F) Inflammatory scores quantified from H&E staining images. (G) Dynamic airway resistance on methacholine (Mch) inhalation measured over multiple doses of Mch using whole body plethysmography. Neutrophil counts (H) and levels of Th1/2/17 cell-related cytokines (I) in BALF after treatment of αIL-17 antibodies at 1 h before every challenge period. n = 4–10 mice per group (B-I). Data are shown as mean ± s.e.m. *$P < 0.05$, ** $P < 0.01$, *** $P < 0.001$, and **** $P < 0.0001$ using one-way analysis of variance (ANOVA) with Tukey's post hoc correction (B-D, F, H, I) and two-way ANOVA with Sidak's post hoc correction (G).

A

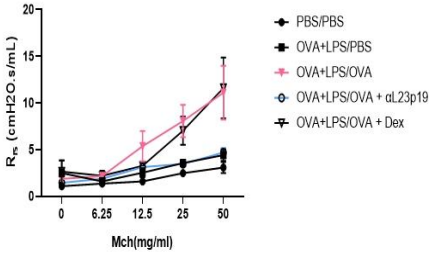

PBS/PBS vs. OVA+LPS/OVA	***
OVA+LPS/PBS vs. OVA/OVA	**
OVA+LPS/OVA vs. OVA+LPS/OVA + αIL23p19	**
OVA+LPS/OVA vs. OVA+LPS/OVA + Dex	ns

B

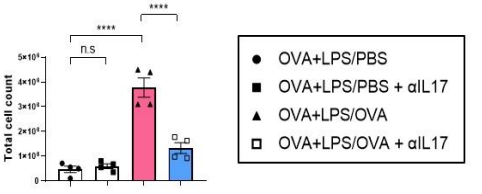

C

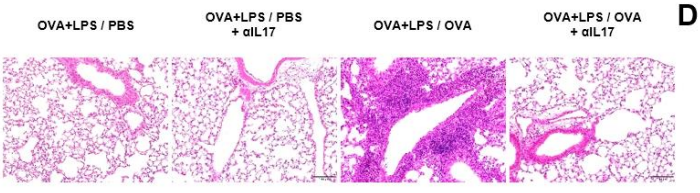

D

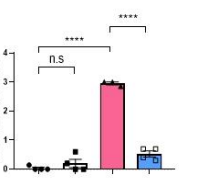

E

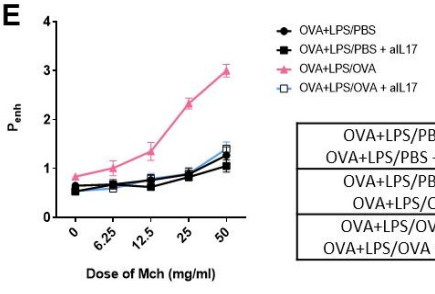

OVA+LPS/PBS vs. OVA+LPS/PBS + αIL17	ns
OVA+LPS/PBS vs. OVA+LPS/OVA	****
OVA+LPS/OVA vs. OVA+LPS/OVA + αIL17	****

Figure 2. Th17 cell activation is required for neutrophilic inflammation in NDA mice. (A) R_{rs} values measured using an invasive ventilated lung resistance method at multiple does of methacholine (Mch) in the indicated conditions. (B) Total cell counts in BALF after treatment of αIL-17 antibodies at 1 h before every challenge period. (C) Representative hematoxylin and eosin (H&E) staining of lung section. (D) Inflammatory scores quantified from H&E staining images. (E) Dynamic airway resistance on Mch inhalation measured over multiple doses of Mch using whole body plethysmography. n = 4–10 mice per group (A-E). Data are shown as mean ± s.e.m. *$P < 0.05$, ** $P < 0.01$, *** $P < 0.001$, and **** $P < 0.0001$ using one-way analysis of variance (ANOVA) with Tukey's post hoc correction (B, D) and two-way ANOVA with Sidak's post hoc correction (A, E).

2. Single cell analyses identify myeloid cell subpopulations associated with therapeutic effects of αIL-23p19 in NDA mouse lungs

To identify immune cell populations associated with therapeutic effects of αIL-23p19, we performed scRNA-seq analysis of $CD45^+$ cells isolated from NDA mouse lungs in OVA+LPS/PBS (n=2), OVA+LPS/OVA (n=3), OVA+LPS/OVA+Dex (n=2), and OVA+LPS/OVA+αIL-23p19 (n=3). A total of 75,369 cells were selected from these four conditions based on previously reported criteria[62] (Fig. 4A, B). With the transcriptome data of the selected cells, we identified 11 cell clusters (RNA C0–10) using Louvain clustering (Fig. 3A). After confirming no bias of each cluster toward a particular condition (Fig. 4C), we then identified marker genes significantly ($P < 0.01$) upregulated in each cluster, with respect to the other clusters, to examine functional characteristics of the cluster (Fig. 3B). We next annotated cell types for these clusters using the label transfer method (SingleR[64]) with the ImmGen reference dataset[63] (Fig. 3A and Fig. 4D, E) and confirmed the cell type annotation using the upregulated known immune cell marker genes: For example, *C1QB* and *ITGAM* for $CD11b^+$ macrophages (RNA C0; Fig. 3C); *S100A9* and *CD14* for neutrophil/monocyte (RNA C8; Fig. 3D); and *CD79A* for B cells and *CTLA4* for Treg cells (Fig. 4F).

In neutrophilic asthma, a variety of myeloid cells are co-recruited into the airways and interplay with each other to promote Th17 cell activation and neutrophil infiltration[91]. To identify the cells associated with therapeutic effects of αIL-23p19, we thus focused on the myeloid cell clusters- $CD11b^+$ macrophage (RNA C0, CM), alveolar macrophage (RNA C2, AM), dendritic cells (RNA C5, DC), monocytes (RNA C6, MO), and neutrophil/monocyte (RNA C8, NM). Since only a subset of cells in each cluster might be associated with therapeutic effects of αIL-23p19, we next identified subclusters of these clusters (Fig. 3E, F and Fig. 4G-I), examined proportions of the cells in each subcluster originated from the four conditions, and selected potential candidates

associated with therapeutic effects of αIL-23p19 as the following subclusters having higher proportions of cells from OVA+LPS/OVA+αIL-23p19 and OVA+LPS/PBS than those from OVA+LPS/OVA and OVA+LPS/OVA+Dex (Fig. 3G, H and Fig. 4J-L): 1) Subcluster C3 of $CD11b^+$ macrophages (RNA CM-C3), Subcluster C2 of alveolar macrophage (RNA AM-C2), Subcluster C2 of dendritic cells (RNA DC-C2), Subcluster C0 of monocytes (RNA MO-C0), and Subcluster C1 of neutrophil/monocytes (RNA NM-C1). The inverse correlation of the cell proportion with Th17 cell activation and neutrophilic inflammation represents therapeutic effects of αIL-23p19. To characterize these selected subclusters, we identified their marker genes (Fig. 3I, J and Fig. 4M-O) and cellular pathways represented by these genes (Fig. 3K). Based on the enriched pathways, among the subclusters, we further selected RNA CM-C3 and RNA NM-C1 strongly associated with neutrophil migration/chemotaxis, a representative cellular process for neutrophilic inflammation. Finally, for the subsequent functional studies of RNA CM-C3 and RNA NM-C1, among their marker genes, we selected the ones whose proteins are localized on plasma membrane for their isolation using FACS with anti-inflammatory functions for associations with therapeutic effects of αIL-23p19 with low amount in OVA+LPS/OVA, but high amount in OVA+LPS/OVA+αIL-23p19. We then prioritized the merged set of the selected marker genes for RNA CM-C3 and RNA NM-C1 based on the mean percentage of cells expressing each marker gene in RNA CM-C3 and RNA NM-C1 (Fig. 3L). Among the top genes, we finally selected CD9, a known anti-inflammatory adhesion molecule[92], and CD39, an ATPase inhibiting ATP-dependent inflammation[93].

Epigenetic mechanisms also play pivotal roles in asthma pathogenesis[94]. We thus performed scATAC-seq of $CD45^+$ cells from NDA mouse lungs under the same conditions. A total of 96,823 cells were selected based on previously reported criteria[65] (Fig. 5A). We identified 15 cell clusters

(ATAC C0–14) using the peak intensities by SLM clustering[95] (Fig. 5B). After confirming no bias of each cluster toward a particular condition (Fig. 5C), we annotated cell types for the clusters by transferring the labels from scRNA-seq data to scATAC-seq data (Fig. 5D). We next selected differentially accessible peaks (DAPs) for each cluster (Fig. 5E) and categorized the DAPs into promoter and distal DAPs (Fig. 5F). Motif analysis of transcription factors (TFs) in the regions of these DAPs revealed that the motifs of TFs, previously known to be associated with each cell type, were enriched in the corresponding clusters [e.g., Mafb for macrophage (ATAC C1), TBX21 for NK cell (ATAC C4), and RORC for Treg cell (ATAC C2 and C13) in Fig. 5G, H]. Because of more distal DAPs than promoter DAPs, the distal DAPs were more strongly enriched with the TFs associated with the corresponding cell types than promoter DAPs, consistent with the previous findings[96,97]. Intriguingly, several enriched TFs were also identified as marker genes for the corresponding cell types, suggesting their functional importance in transcriptional regulation of the cell type. For example, Mafb was identified as a marker gene for $CD11b^+$ macrophages (RNA C0), and its binding motif was enriched in the distal DAPs for $CD11b^+$ macrophages (ATAC C1) (Fig. 5H).

To confirm the validity of the selected RNA CM-C3 and NM-C1 from scATAC-seq data, we then identified ATAC subclusters for $CD11b^+$ macrophages (ATAC C1) and neutrophil/monocytes (ATAC C6) and selected the subclusters corresponding to RNA CM-C3 (ATAC CM-C2) and RNA NM-C1 (ATAC NM-C1) (Fig. 6A-D) based on the transferred labels. The proportions of the cells in these ATAC subclusters originated from the four conditions were relatively higher in OVA+LPS/OVA+αIL-23p19 and OVA+LPS/PBS than in OVA+LPS/OVA and OVA+LPS/OVA+Dex (Fig. 6E, F), consistent with those observed in RNA CM-C3 and NM-C1. To characterize these ATAC CM-C2 and NM-C1, we identified for promoter and distal DAPs

for them (Fig. 6G) and then performed peak-level gene ontology enrichment analysis for the DAPs using GREAT. The enriched cellular pathways were largely consistent with those from RNA CM-C3 and NM-C1 (Fig. 3K and Fig. 6H). Moreover, the motif analysis also revealed that three (*NR4A2*, *MITF*, and *EGR2*) and five TFs (*CEBPB*, *NFE2L2*, *FOS*, *FOSL2*, and *JDP2*) were identified as marker genes for RNA CM-C3 and NM-C1, respectively, and their binding motifs were consistently enriched in the DAPs for ATAC CM-C2 and NM-C1, respectively (Fig. 6I). A majority of these TFs (*NR4A2*[98], *MITF*[99] , *EGR2*[100], *CEBPB*[101], *NFE2L2*[102], and *FOS*[103]) have anti-inflammatory functions in macrophages, supporting their associations with therapeutic effects of αIL-23p19. Finally, we then examined the mean peak intensities of the two selected markers CD9 and CD39 in RNA CM-C3 and NM-C1 and found that the gene body peaks showed higher intensities in OVA+LPS/OVA+αIL-23p19 and OVA+LPS/PBS than in OVA+LPS/OVA and OVA+LPS/OVA+Dex, consistent with therapeutic effects of αIL-23p19 (Fig. 6J-M). All these results collectively support the validity of RNA CM-C3 and NM-C1, as well as their marker genes CD9 and CD39.

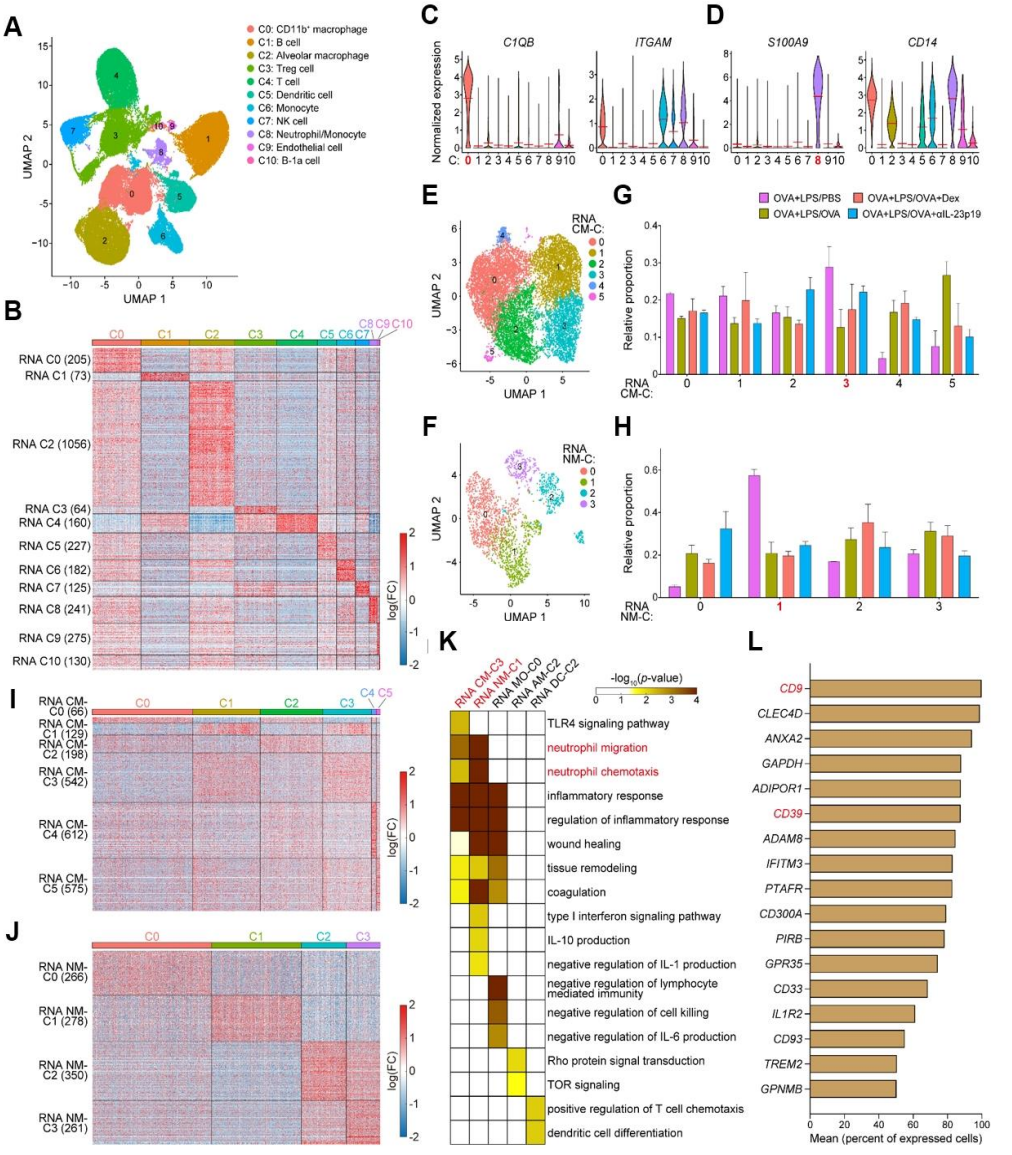

Figure 3. Myeloid cell subpopulations expressing anti-inflammatory genes were increased by αIL-23p19 treatment in NDA mouse lungs. (A) Uniform manifold approximation and projection (UMAP) plot showing 11 clusters (RNA C0-10) of CD45^{+} immune cells. (B) Heat map showing marker genes significantly upregulated in RNA C0-10. Red and blue colors represent

increased and decreased log(fold change) of marker genes (row) identified for each cluster (number of marker genes in parenthesis), respectively, with respect to their median expression across all samples (column). Color bar, gradient of the log(fold change). (C, D) Violin plots showing distributions of expression levels of the indicated genes across RNA C0–10. Red highlighted, clusters for which the indicated marker genes were identified. Red line, mean value. (E, F) UMAP plots showing six (RNA CM-C0–5, E) and four (RNA NM-C0-3, F) subclusters of $CD11b^+$ macrophage (RNA C0) and neutrophil/monocyte (RNA C8) clusters, respectively. (G, H) Relative proportions of cells originated from four conditions in RNA CM-C0–5 (G) or RNA NM-C0-3 (H). n = 2, 3, 2, and 3 samples for OVA+LPS/PBS (PBS), OVA+LPS/OVA (OVA), OVA+LPS/OVA+DEX (DEX), and OVA+LPS/OVA+αIL-23p19 (P19), respectively. Proportions per clusters in each sample were normalized for their sum to be one, which are shown under each condition as mean ± s.e.m. (I, J) Heat maps showing marker genes significantly upregulated in RNA CM-C0–5 (I) and RNA NM-C0–3 (J). (K) Heat map showing gene ontology biological processes (GOBPs) enriched by marker genes for RNA CM-C3, RNA NM-C1, RNA MO-C0, RNA AM-C2, and RNA DC-C2 and their enrichment significance (*p*) from the DAVID software as $-\log_{10}$(*p*-value). Red labeled, GOBPs related to neutrophilic inflammation and subclusters in which those GOBPs are enriched. (I) Bar plot showing mean percentage of cells expressing the indicated anti-inflammatory genes whose proteins are localized on plasma membrane in RNA CM-C3 and RNA NM-C1. Red labeled, candidate genes associated with therapeutic effects of αIL-23p19.

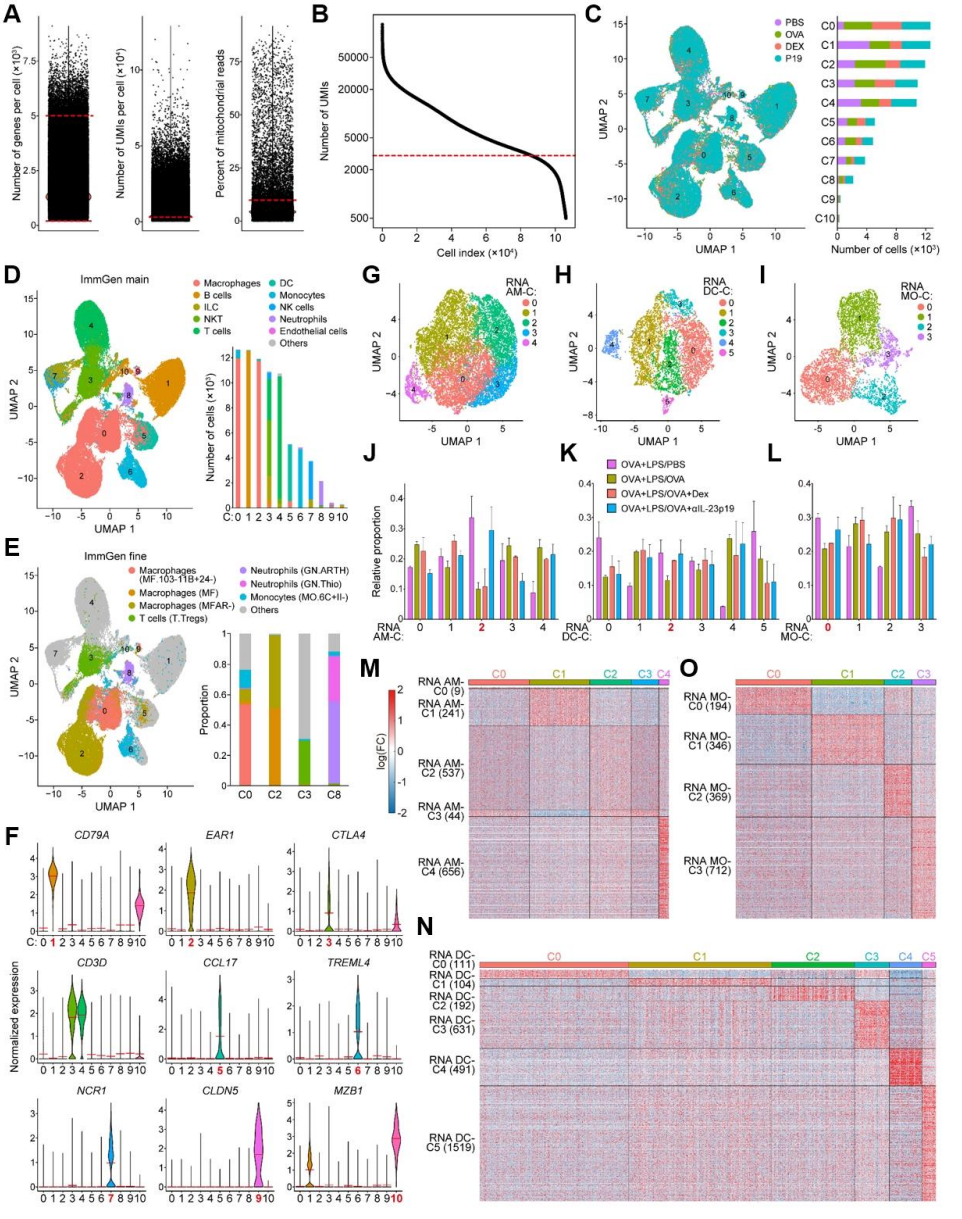

Figure 4. Characteristics of immune cell clusters identified from scRNA-seq data. (A) Distributions of the number of genes per cell, the number of unique molecular identifiers (UMIs) per cell, and percent of mitochondrial reads. Red dashed lines, cutoffs used for selecting cells. (B) A plot showing the number of

UMIs (i.e., total UMIs) in individual cells sorted in a descending manner. Red dashed line, cutoff used for selecting cells. (C) Uniform manifold approximation and projection (UMAP) plot (left) showing which of the following four conditions individual cells in 11 clusters (RNA C0-10) were originated from: PBS, OVA+LPS/PBS; OVA, OVA+LPS/OVA; DEX, OVA+LPS/OVA+DEX; and P19, OVA+LPS/OVA+αIL-23p19. The bar plot (right) shows the numbers of cells originated from the conditions. (D, E) UMAP plots (left) showing ImmGen main (D) and fine (E) cell types predicted by label transfer. The bar plots (right) show the numbers of cells in RNA C0-10 predicted to each cell type (D) and the relative proportion of cells in RNA C0, 2, 3, and 8 predicted to the indicated cell types (E). (F) Violin plots showing distributions of expression levels of the indicated genes across RNA C0-10. Red highlighted, clusters for which the indicated marker genes were identified. Red line, mean value. (G-I) UMAP plots showing five (RNA AM-C0-4, G), six (RNA DC-C0-5, H), and four (RNA MO-C0-3, I) subclusters of the alveolar macrophage (RNA C2), dendritic cell (RNA C5), and monocyte (RNA C6) clusters, respectively. (J-L) Relative proportions of cells originated from four conditions in RNA AM-C0-4 (J), RNA DC-C0-5 (K), and RNA MO-C0-3 (L). n = 2, 3, 2, and 3 samples for PBS, OVA, DEX, and P19, respectively. Proportions per clusters in each sample were normalized for their sum to be one, which are shown under each condition as mean ± s.e.m. (M-O) Heat maps showing marker genes significantly upregulated in RNA AM-C0–4 (M), RNA DC-C0-5 (N), and RNA MO-C0–3 (O). Red and blue colors represent increased and decreased log(fold change) of marker genes (row) identified for each cluster (number of marker genes in parenthesis), respectively, with respect to their median expression across all samples (column). Color bar, gradient of the log(fold change).

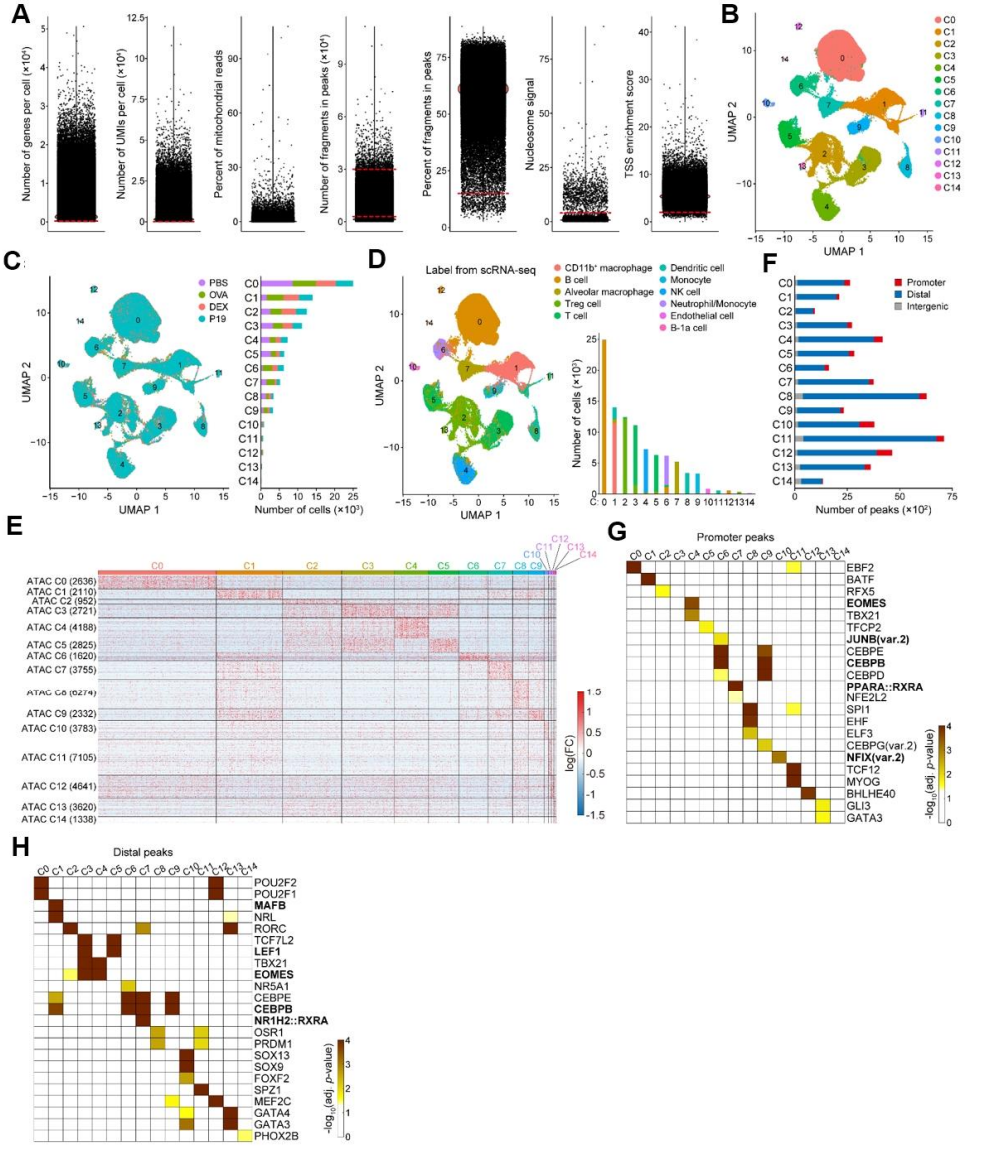

Figure 5. Characteristics of immune cell clusters identified from scATAC-seq data. (A) Distributions of the number of genes per cell, the number of UMIs per cell, percent of mitochondrial reads, the number of fragments in peaks, percent of fragments in peaks, nucleosome signal, and transcription start site (TSS) enrichment score. Red dashed lines, cutoffs used for selecting cells. (B) UMAP plot showing 15 clusters (ATAC C0-14) of $CD45^+$ immune cells. (C) UMAP plot (left) showing which of the four conditions individual cells in ATAC C0-14 were originated from. The bar plot (right) shows the numbers of cells originated from the conditions. (D) UMAP plot (left) showing RNA clusters predicted by label transfer from the scRNA-seq data. The bar plot (right) shows the numbers of cells in ATAC C0-14 predicted to RNA clusters. (E) Heat map showing differentially accessible peaks (DAPs) for ATAC C0-14. Red and blue colors represent increased and decreased log(fold change) of DAPs (row) identified for each cluster (number of DAPs in parenthesis), respectively, with respect to their median intensity across all samples (column). Color bar, gradient of the log(fold change). (F) Numbers of differentially accessible promoter, distal, and intergenic peaks for ATAC C0-14. (G, H) Heat maps showing motifs enriched by differentially accessible promoter (G) and distal (H) peaks for ATAC C0-14 and their enrichment significance (*p*) from 'FindMotifs' function in Signac as $-\log_{10}$(adjusted *p*-value). Bold labeled, transcription factors that had their motifs enriched and were also identified as marker genes in the corresponding RNA clusters.

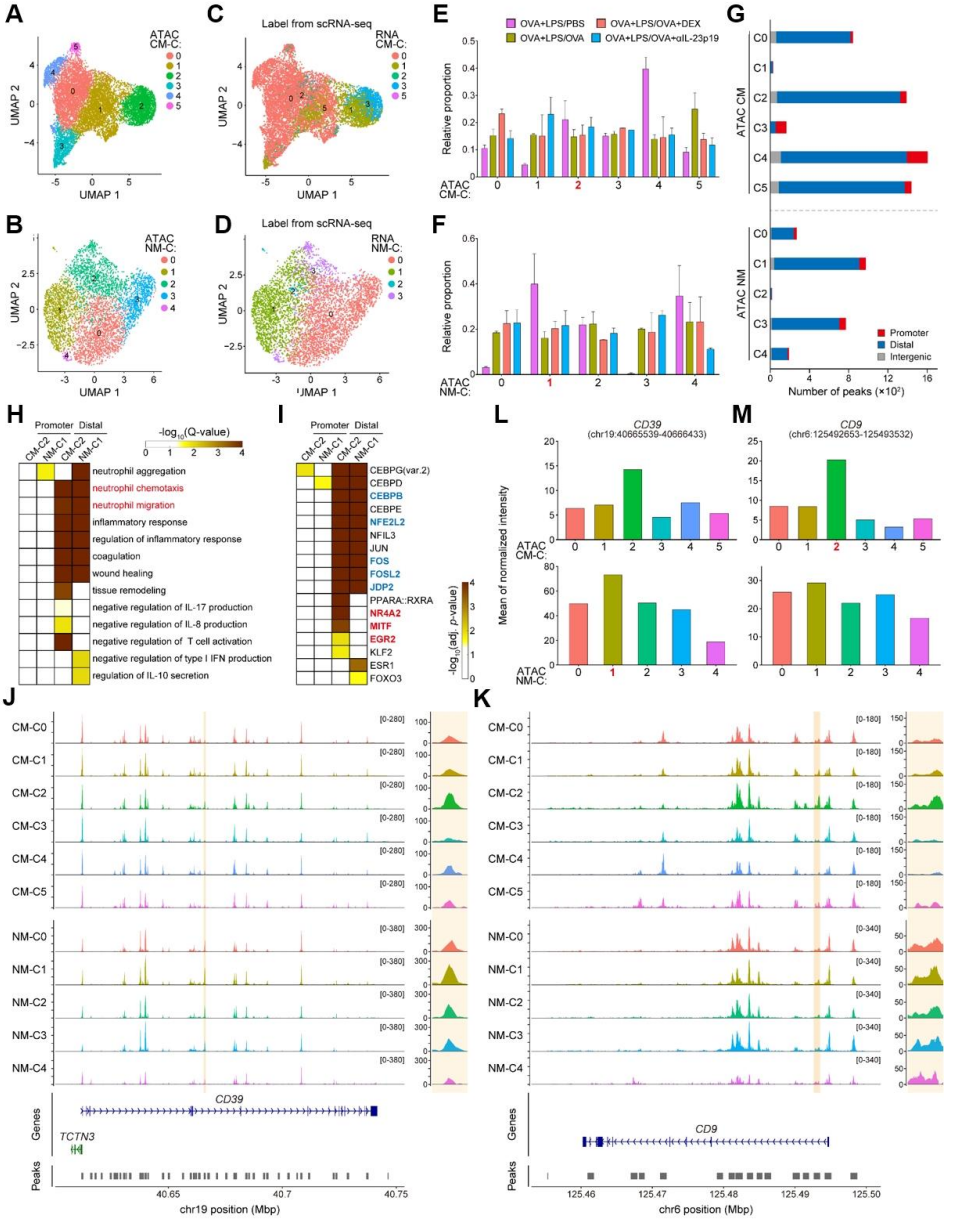

Figure 6. Characteristics of CD11b^{+} macrophage and neutrophil/monocyte subpopulations. (A, B) UMAP plots showing six (ATAC CM-C0-5, A) and five (ATAC NM-C0-4, B) subclusters of ATAC C1 and ATAC C6 clusters, respectively. (C, D) UMAP plots showing RNA CM (C) and NM (D)

subclusters predicted by label transfer from the scRNA-seq data. (E, F) Relative proportions of cells originated from four conditions in ATAC CM-C0-5 (E) and ATAC NM-C0-4 (F). n=3, 3, 2, and 2 samples for PBS, OVA, DEX, and P19, respectively. Data are shown under each condition as mean ± s.e.m. (G) Numbers of differentially accessible promoter, distal, and intergenic peaks for ATAC CM-C0-5 and ATAC NM-C0-4. (H) Heat map showing gene ontology biological processes (GOBPs) enriched by differentially accessible promoter and distal peaks for ATAC CM-C2 and ATAC NM-C1 and their enrichment significance (Q) from the GREAT software as $-\log_{10}$(Q-value). Red labeled, GOBPs related to neutrophilic inflammation. (I) Heat map showing motifs enriched by differentially accessible promoter and distal peaks for ATAC CM-C2 and ATAC NM-C1 and their enrichment significance (*p*) from the FindMotifs function in Signac as $-\log_{10}$(adjusted *p*-value). Red and blue labels in bold indicate transcription factors that had their motifs enriched and were also identified as marker genes in RNA CM-C3 and RNA NM-C1, respectively. (J, K) Read distributions in the *CD39* (J) and *CD9* (K) loci across ATAC CM-C0-5 and ATAC NM-C0-4. The maximum y-axis scale is noted in parenthesis at the top right of each plot. Gene structure, peak regions, chromosome number, and coordinates are shown in the bottom. Highlighted orange box, gene body peak of CD39 (J) or CD9 (K) with higher intensities in both ATAC CM-C2 and ATAC NM-C1 compared to the other subclusters (enlarged view on the right). Mbp, megabase pair. (L. M) Bar plots showing the mean of normalized intensities of the indicated gene body peaks of *CD39* (L) and *CD9* (M) in ATAC CM-C0-5 (top) and ATAC NM-C0-4 (bottom). Red highlighted, clusters for which the indicated peaks were identified as DAPs.

3. Myeloid cells expanded by αIL-23p19 treatment are Ly6G-negative CD39$^+$CD9$^+$ interstitial macrophages

The above results suggest myeloid cell subpopulations expressing the anti-inflammatory genes *CD39* and *CD9* (RNA CM-C3 and NM-C1) potentially associated with therapeutic effects of αIL-23p19. To test this finding, we gated CD45$^+$CD11b$^+$CD11c$^-$ cells isolated from NDA mouse lungs into Ly6G$^+$ (neutrophils) and Ly6G$^-$ cells and further into Ly6G$^-$CD39$^+$CD9$^+$CD11b$^+$CD11c$^-$ and Ly6G$^+$CD39$^+$CD9$^+$CD11b$^+$CD11c$^-$ cells, which are considered to correspond to RNA CM-C3 and NM-C1, respectively (Fig. 8A, B). The percentages of Ly6G$^+$CD11b$^+$CD11c$^-$ neutrophils were increased in OVA+LPS/OVA in the lung, and such increase was reduced by αIL-23p19 (Fig. 7A), confirming the findings from BALF (Fig. 1B). The percentage of Ly6G$^-$CD39$^+$CD9$^+$CD11b$^+$CD11c$^-$ cells was decreased significantly in OVA+LPS/OVA, compared to that in OVA+LPS/PBS, which was restored in OVA+LPS/OVA+αIL-23p19 (Fig. 7B). On the other hand, Ly6G$^+$CD39$^+$CD9$^+$ CD11b$^+$CD11c$^-$ cells were relatively less abundant than Ly6G$^-$CD39$^+$ CD9$^+$CD11b$^+$CD11c$^-$ cells in OVA+LPS/OVA+αIL-23p19 (Fig. 7B, C), consistent with the cell counts of RNA CM-C3 (2127 cells) and RNA NM-C1 (673 cells) detected from scRNA-seq. Moreover, Ly6G$^+$CD39$^+$CD9$^+$CD11b$^+$ CD11c$^-$ cells showed a weaker alteration trend than Ly6G$^-$CD39$^+$CD9$^+$CD11b$^+$ CD11c$^-$ cells with no statistical significance over the conditions (Fig. 7C). These data suggest the presence of cells in RNA CM-C3 and NM-C1, but that Ly6G$^-$CD39$^+$CD9$^+$CD11b$^+$CD11c$^-$ cells (RNA CM-C3) showed a stronger correlation with therapeutic effects of αIL-23p19 than Ly6G$^+$CD39$^+$CD9$^+$ CD11b$^+$CD11c$^-$ cells (RNA NM-C1).

To explore the identity of these cells, we examined their morphology by cytospin preparation. The majority of Ly6G$^-$CD39$^+$CD9$^+$CD11b$^+$CD11c$^-$ cells (94.2%) and Ly6G$^+$CD39$^+$CD9$^+$CD11b$^+$ CD11c$^-$ (90.1%) were

mononuclear (MN) and polymorphonuclear (PMN) cells, respectively (Fig. 7D). Although scRNA-seq annotated RNA CM-C3 with $CD11b^+$ macrophages, we further tested whether the $Ly6G^-CD39^+CD9^+CD11b^+CD11c^-$ cells would be interstitial macrophages (IMs) or other cells (monocytes or $CD11b^+$ dendritic cells). To this end, we gated $Ly6G^-CD39^+CD9^+CD11b^+CD11c^-$ and $Ly6G^-CD39^-CD9^-CD11b^+CD11c^-$ cells using the expression of F4/80 and MHC class II (MHCII)[104] and found that $Ly6G^-CD39^+CD9^+CD11b^+CD11c^-$ cells showed higher expression of both F4/80 and MHCII in OVA+LPS/OVA +αIL-23p19 than $Ly6G^-CD39^-CD9^-CD11b^+CD11c^-$ cells (Fig. 7E), which was further confirmed in lung tissues through immunofluorescence staining (Fig. 8C). These results suggest that $Ly6G^-CD39^+CD9^+CD11b^+CD11c^-$ cells are $CD39^+CD9^+$ IMs while $Ly6G^-CD39^-CD9^-CD11b^+CD11c^-$ cells are $CD39^-CD9^-$ monocytes. Previously, IL-10-producing IMs were reported to inhibit allergen-induced neutrophilic asthma by inhibiting Th2 and Th17 responses[104]. However, in the lung of our NDA model, IL-10-producing $CD39^+CD9^+$ IMs were not detected in OVA+LPS/PBS or OVA+LPS/OVA+αIL-23p19 (Fig. 8D), and IL-10 levels in BALF were not changed by αIL-23p19 (Fig. 8E), indicating that $CD39^+CD9^+$ IMs function in an IL-10-independent manner.

To further confirm the similarity of $CD39^+CD9^+$ IMs with RNA CM-C3, we performed bulk RNA-seq analysis of $CD39^+CD9^+$ IMs (n=3) and $CD39^-CD9^-$ monocytes (n=3) isolated from OVA+LPS/OVA+αIL-23p19 (Fig. 8B). We then performed cell type deconvolution analysis for the bulk RNA-seq data with marker genes of the initial five subcluster candidates (Fig. 3K) to be associated with therapeutic effects of αIL-23p19 using CIBERSORTx[71]. Cells in RNA CM-C3 were the most highly abundant in $CD39^+CD9^+$ IMs, but almost absent in $CD39^-CD9^-$ monocytes (Fig. 7F), whereas cells in RNA MO-C0 were highly abundant in $CD39^-CD9^-$ monocytes, but low in $CD39^+CD9^+$ IMs. Cells in these other clusters were found to be almost absent in both $CD39^+CD9^+$ IMs

and $CD39^{-}CD9^{-}$ monocytes, although alveolar macrophages in RNA-AM-C2 were found present in both cells, but relatively lower than those in RNA CM-C3 or RNA MO-C0, probably due to their shared characteristics to both cells. These data suggest that $CD39^{+}CD9^{+}$ IMs contained mainly the cells in RNA CM-C3, consistent with the abundance differences of these cells (Fig. 7B, C).

We next questioned how the increased IL-23 leads to decrease of $CD39^{+}CD9^{+}$ IMs population. To answer this question, we hypothesized that IL-23 cytokine increased in NDA condition could induce cell death of $CD39^{+}CD9^{+}$ IMs present in normal untreated mice. To test this hypothesis, we obtained $CD39^{+}CD9^{+}$ IMs from normal untreated mouse lungs using FACS sorting, and then analyzed the cell death of $CD39^{+}CD9^{+}$ IMs in the presence or absence of recombinant IL-23 (rIL-23). rIL-23 treatment increased the late apoptosis (AnnexinV+/PI+) of $CD39^{+}CD9^{+}$ IMs (Fig. 7G, H). Moreover, IL-23 receptor neutralizing antibody (αIL-23r) treatment reversed the increased rIL-23-induced death of $CD39^{+}CD9^{+}$ IMs into the basal level (Fig. 7G, H). In support, the bulk RNA-seq data of $CD39^{+}CD9^{+}$ IMs further confirmed the expression of IL-23 receptor gene (*IL23R*) in $CD39^{+}CD9^{+}$ IMs isolated from OVA+LPS/OVA+αIL-23p19 (mean read count of triplicates = 1.67). Unlike $CD39^{+}CD9^{+}$ IMs, the IL23R gene was not expressed in $CD39^{-}CD9^{-}$ monocytes (read count =0 in all triplicates). Accordingly, $CD39^{-}CD9^{-}$ monocytes showed no significant responses to IL-23 or αIL-23r (Fig. 7G, I). These data suggest that the increased IL-23 in OVA+LPS/OVA reduces $CD39^{+}CD9^{+}$IMs by inducing cell death.

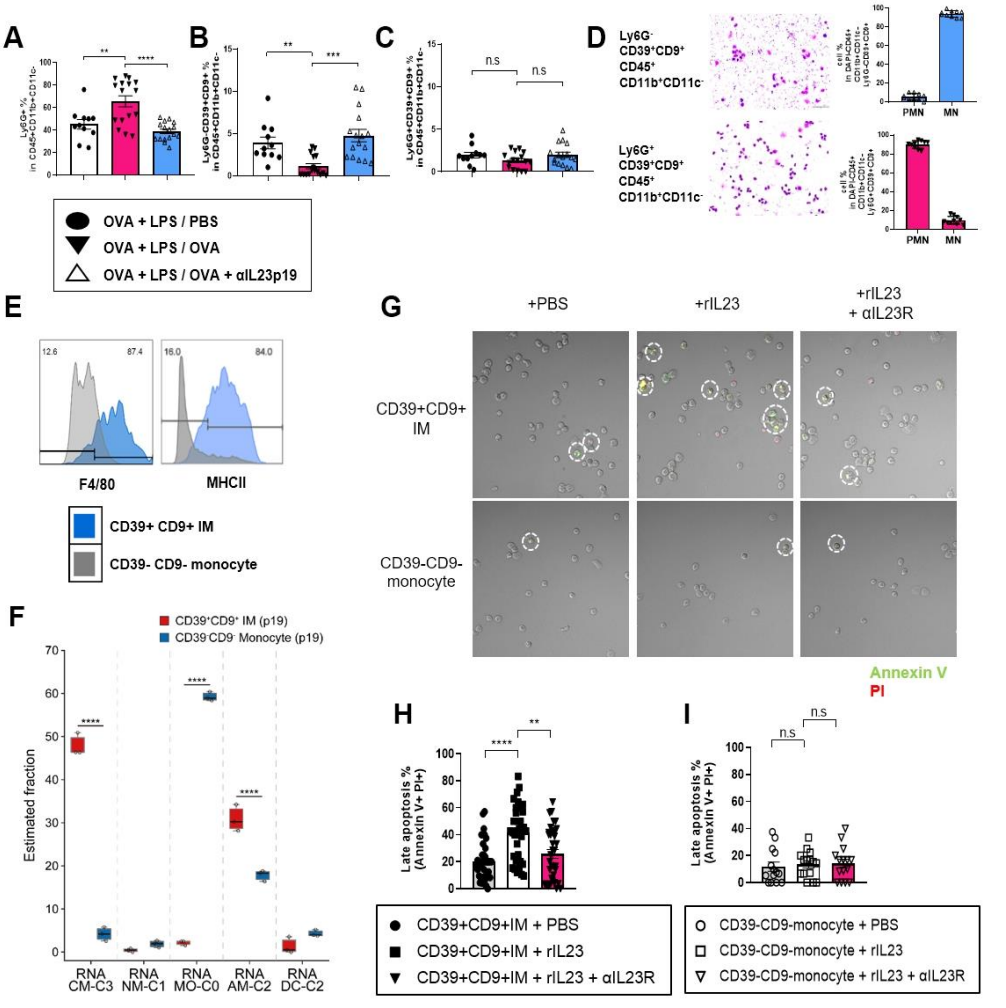

Figure 7. Myeloid cell subpopulations identified by single cell analyses were $CD39^+CD9^+$ interstitial macrophages. (A-C) Percentages of $Ly6G^+$ neutrophils (A), $Ly6G^-CD39^+CD9^+$ IMs (B), and $Ly6G^+CD39^+CD9^+$ neutrophils (C) in $CD45^+CD11b^-CD11c^-$ cells of lung under the indicated conditions. (D) Percentages of mononuclear (MN) and polymorphonuclear (PMN) cells in $CD39^+CD9^+$ IMs (blue bars) or $Ly6G^+$ neutrophils (red bars) measured by Wright–Giemsa staining (right). Representative staining images are shown (left). (E) Histograms of F4/80 and MHCII expression levels of $CD39^+CD9^+$ IMs (blue) or $CD39^-CD9^-$ monocytes (gray). (F) Estimated fractions of RNA CM-C3, RNA NM-C1, RNA MO-C0, RNA AM-C2, and RNA DC-C2 in $CD39^+CD9^+$ IMs and $CD39^-CD9^-$ monocytes. In the box plots, the center line and box limits indicate median value and upper/lower quartiles, respectively. (G) Representative images of lung immunostaining for PI (red), Annexin V-FITC (green), and T-PMT (light). (H, I) Percentage of $CD39^+CD9^+$ IMs (H) or $CD39^-CD9^-$ monocytes (I) undergoing late apoptosis (Annexin V+/PI+) in field of view (FOV). n = 10–15 mice (A-C) and 4–6 mice per group (D-I). Data are shown as mean ± s.e.m. *$P < 0.05$, ** $P < 0.01$, *** $P < 0.001$, and **** $P < 0.0001$ using one-way ANOVA with Tukey's post hoc correction (A-C, H, I) and two-way ANOVA with Sidak's post hoc correction (F).

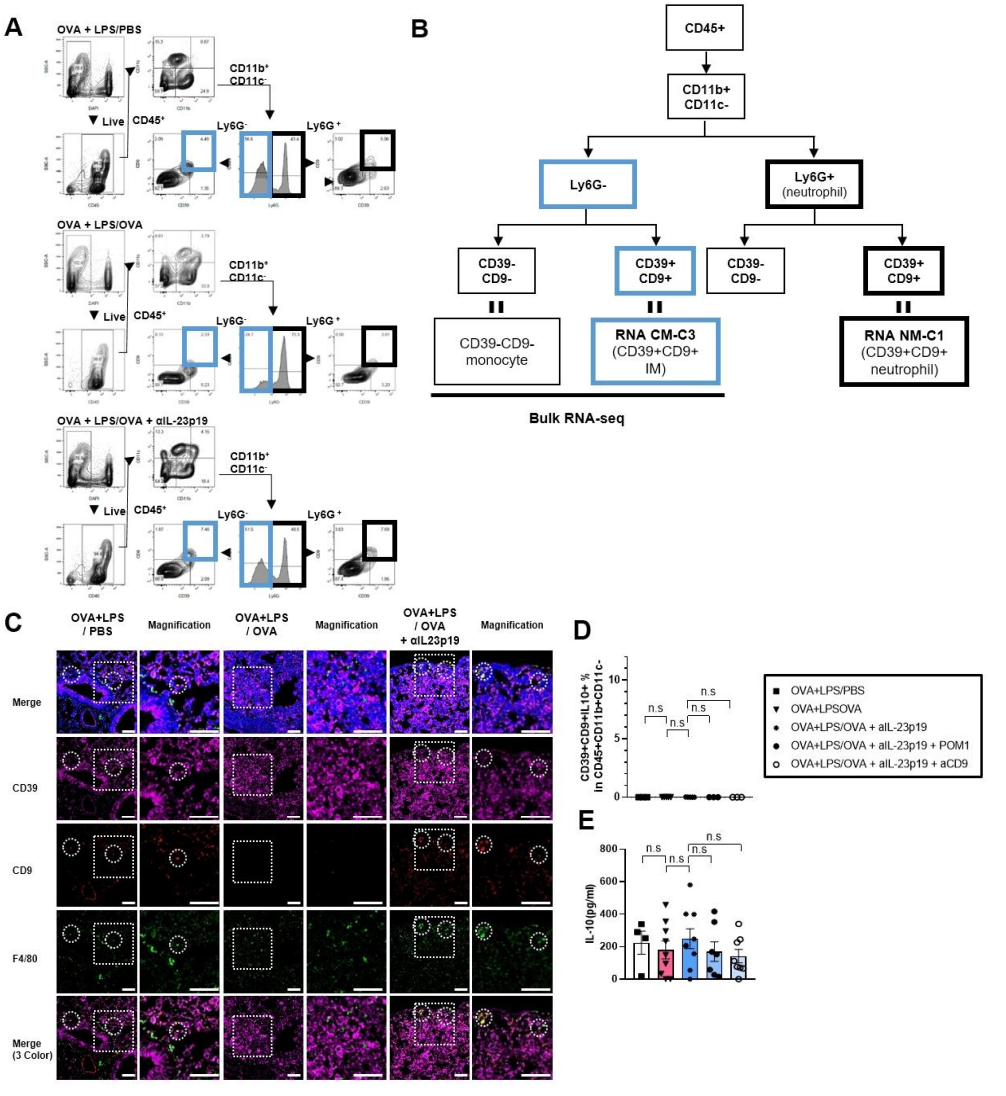

Figure 8. Myeloid cells expanded by αIL-23p19 treatment are Ly6G-negative CD39$^+$CD9$^+$ IMs. (A) Flow cytometry gating strategy to identify CD39$^+$CD9$^+$ immune cells in lungs. (B) Schematic diagram showing how the flow cytometry gating in (A) results in CD39$^-$CD9$^-$ monocytes, CD39$^+$CD9$^+$ IMs, and CD39$^+$CD9$^+$ neutrophils. (C) Representative confocal microscopy images of immunostaining for CD9 (red), CD39 (purple), and F4/80 (green). Merged F4/80$^+$CD39$^+$CD9$^+$ cells are indicated by circles. (D) Percentage of IL10$^+$CD39$^+$CD9$^+$ IMs in the lung. (E) IL-10 levels in BALF measured in the indicated conditions. n = 4–10 mice per group (A, C-E). Data are shown as mean ± s.e.m. n.s., not significant by one-way ANOVA with Tukey's post hoc correction (D, E).

4. CD39 and CD9 are responsible for αIL-23p19-dependent suppression of Th17 cell activation and neutrophilic inflammation in NDA mice

To examine functional roles of CD39 and CD9 on $CD39^+CD9^+$ IMs, POM1, a CD39 inhibitor, or a CD9 neutralizing antibody (αCD9) was treated in OVA+LPS/OVA+ αIL-23p19. Intriguingly, the increased percentage of $CD39^+CD9^+$ IMs by αIL-23p19 was returned to the level in OVA+LPS/OVA by POM1 or αCD9 treatment (Fig. 9A). Correspondingly, the decreased percentages of neutrophils in the lung and also the decreased counts of total cells and neutrophils in BALF, as well as the decreased levels of Th17-related cytokines (IL-17 and IL-22) in BALF, after αIL-23p19 treatment were returned to the levels before αIL-23p19 treatment (OVA+LPS/OVA) by POM1 or αCD9 treatment (OVA+LPS/OVA+αIL-23p19+POM1 or αCD9 in Fig. 9B-E). Immune cell infiltration (Fig. 9F, G) and P_{enh} values (Fig. 9H) also showed the similar alteration patterns by POM1 and αCD9. Moreover, to examine the synergistic effect of POM1 and αCD9, we treated our NDA mice in OVA+LPS/OVA+αIL-23p19 simultaneously with POM1 and αCD9 (POM1+αCD9). The co-treatment showed the same alternation patterns with the individual treatment, but the abolishing extents of therapeutic effects of αIL-23p19 were found to be similar between the co-treatment and individual treatment (Fig. 10A-I). These data indicate no synergistic effect, implying that both CD39 and CD9 are required for therapeutic effects of αIL-23p19. In contrast, without αIL-23p19 treatment, the percentage of $CD39^+CD9^+$ IMs was not significantly affected by POM1 or αCD9 (OVA+LPS/OVA+POM1 or αCD9 in Fig. 9A), neither were the percentage of neutrophils in the lung, the cytokine levels in BALF, immune cell infiltration, and P_{enh} values (Fig. 9B, E-H). Taken together, these data suggest that CD39 and CD9 together contribute to therapeutic effects of αIL-23p19. Of note, consistent with the above finding that

$CD39^{+}CD9^{+}$ IMs had no expression of IL-10, POM1 or αCD9 treatment had no effect on IL-10 level in BALF (Fig. 8D, E).

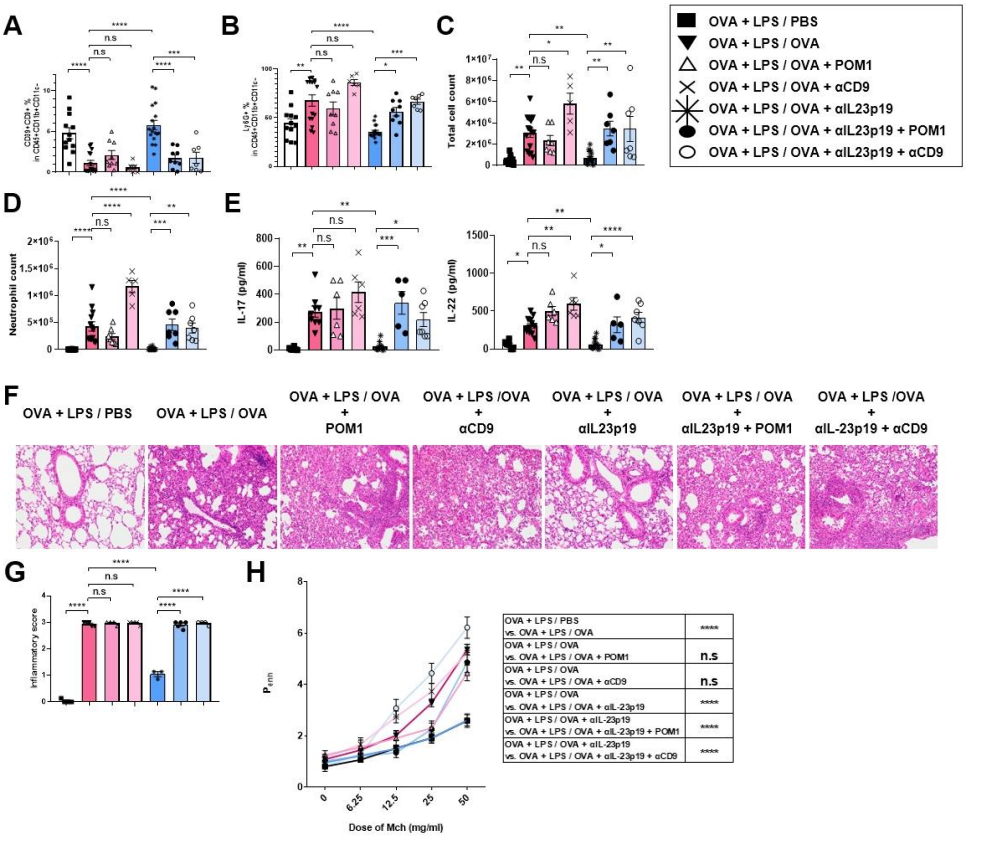

Figure 9. CD39 and CD9 are responsible for αIL-23p19-dependent suppression of Th17 cell activation and neutrophilic inflammation in NDA mice. (A, B) Percentages of $CD39^{+}CD9^{+}$ IMs (A) and $Ly6G^{+}$ neutrophils (B) in $CD45^{+}CD11b^{-}CD11c^{-}$ cells of lung under the indicated conditions. (C-E) Total cell (C) and neutrophil (D) counts and IL-17 and IL-22 levels (E) in BALF under the indicated conditions. (F, G) Representative images of H&E staining (F) and inflammatory scores quantified from H&E staining (G). (H) Dynamic airway resistance on methacholine inhalation measured over multiple doses of Mch under the indicated conditions. n = 5–22 mice per group (A-H). Data are shown as mean ± s.e.m. $*P < 0.05$, $**P < 0.01$, $***P < 0.001$, and $****P < 0.0001$ using one-way ANOVA with Tukey's post hoc correction (A-E, G) and two-way ANOVA with Sidak's post hoc correction (H).

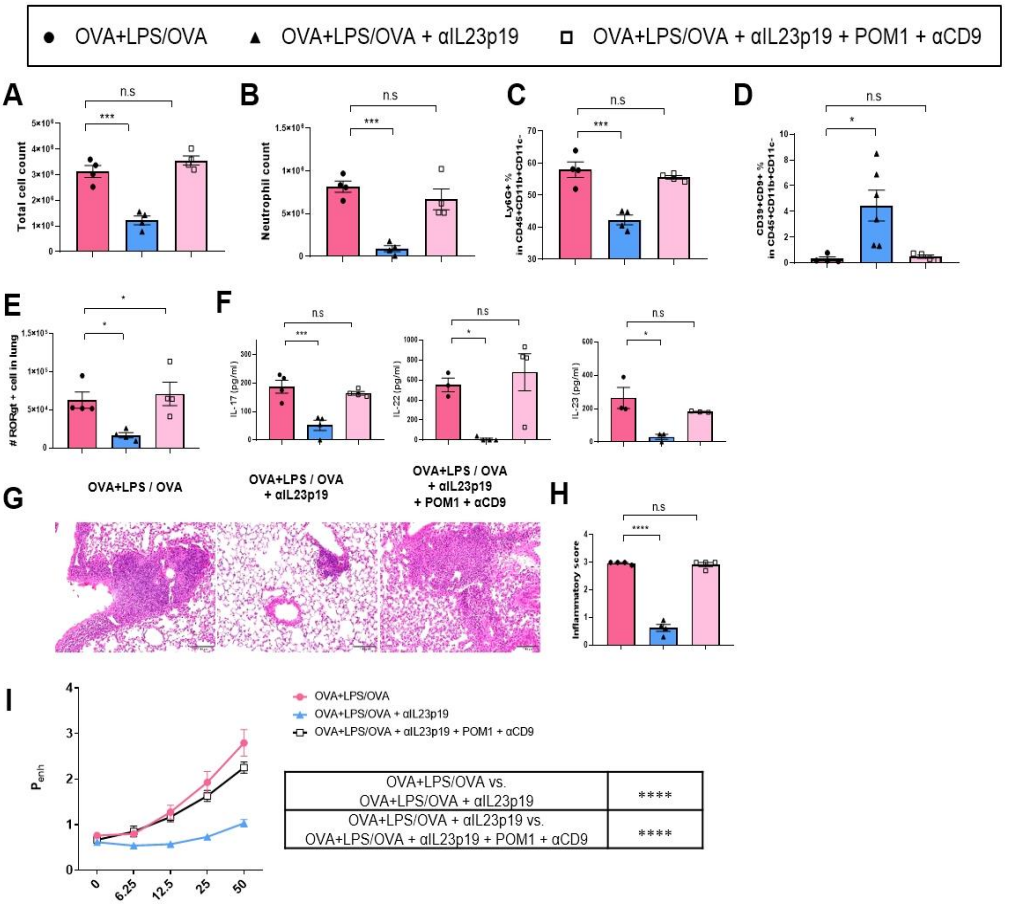

OVA+LPS/OVA vs. OVA+LPS/OVA + αIL23p19	****
OVA+LPS/OVA + αIL23p19 vs. OVA+LPS/OVA + αIL23p19 + POM1 + αCD9	****

Figure 10. Both CD39 and CD9 are responsible for αIL-23p19-dependent suppression of Th17 cell activation and neutrophilic inflammation in NDA mice. (A-F) Total cell (A) and neutrophil (B) counts in BALF, percentages of $Ly6G^+$ neutrophils (C) and $CD39^+CD9^+$ IMs (D), and $RORgt^+$ cells in $CD4^+$ T cells (E) in the lung, and levels of IL-17, IL-22, and IL-23 in BALF (F). (G-H) Representative images of H&E staining (G) and inflammatory scores quantified from H&E staining (H). (I) Dynamic airway resistance on methacholine inhalation measured over multiple doses of Mch under the indicated conditions. n = 3–8 mice per group (A-I). Data are shown as mean ± s.e.m. $*P < 0.05$, $**P < 0.01$, $***P < 0.001$, and $****P < 0.0001$ using one-way ANOVA with Tukey's post hoc correction (A-F, H) and two-way ANOVA with Sidak's post hoc correction (I).

5. Adoptive transfer of $CD39^+CD9^+$ IMs ameliorates Th17 cell activation and neutrophilic inflammation in NDA mouse lungs

The above results from POM1 and αCD9 inhibition experiments suggest the possibility that $CD39^+CD9^+$ IMs inhibit Th17 cell activation and neutrophilic inflammation. To directly test this possibility, we intravenously injected 1) $CD39^+CD9^+$ IMs isolated from OVA+LPS/OVA+αIL-23p19 mice, 2) $Ly6G^+CD39^+CD9^+CD11b^+CD11c^-$ cells ($CD39^+CD9^+$ neutrophils as negative control; Fig. 8B), and 3) PBS (non-cellular negative control) into NDA mice (Fig. 11A). The transfer of $CD39^+CD9^+$ IMs, but not $CD39^+CD9^+$ neutrophils, significantly reduced total cell and neutrophil counts in BALF, neutrophil percentage in the lung, $ROR\gamma t^+$ Th17 cell count, and the levels of Th17-related cytokines (IL-17 and IL-22) (Fig. 11B-E), as well as IL-23 level (Fig. 11F) and neutrophil infiltration (Fig. 11G, H). Transferred $CD39^+CD9^+$ IMs also enhanced respiratory function such as P_{enh} values (Fig. 11I). The transfer of $CD39^+CD9^+$ IMs isolated from untreated control mice (PBS/PBS) also showed similar effects to those from OVA+LPS/OVA+αIL-23p19 mice. Together with the results from POM1 and αCD9 treatments (Fig. 9), these results indicate that $CD39^+CD9^+$ IMs increased after αIL-23p19 treatment or present in basal state alleviate Th17 cell activation and neutrophilic inflammation in NDA mice in CD39 and CD9-dependent manners.

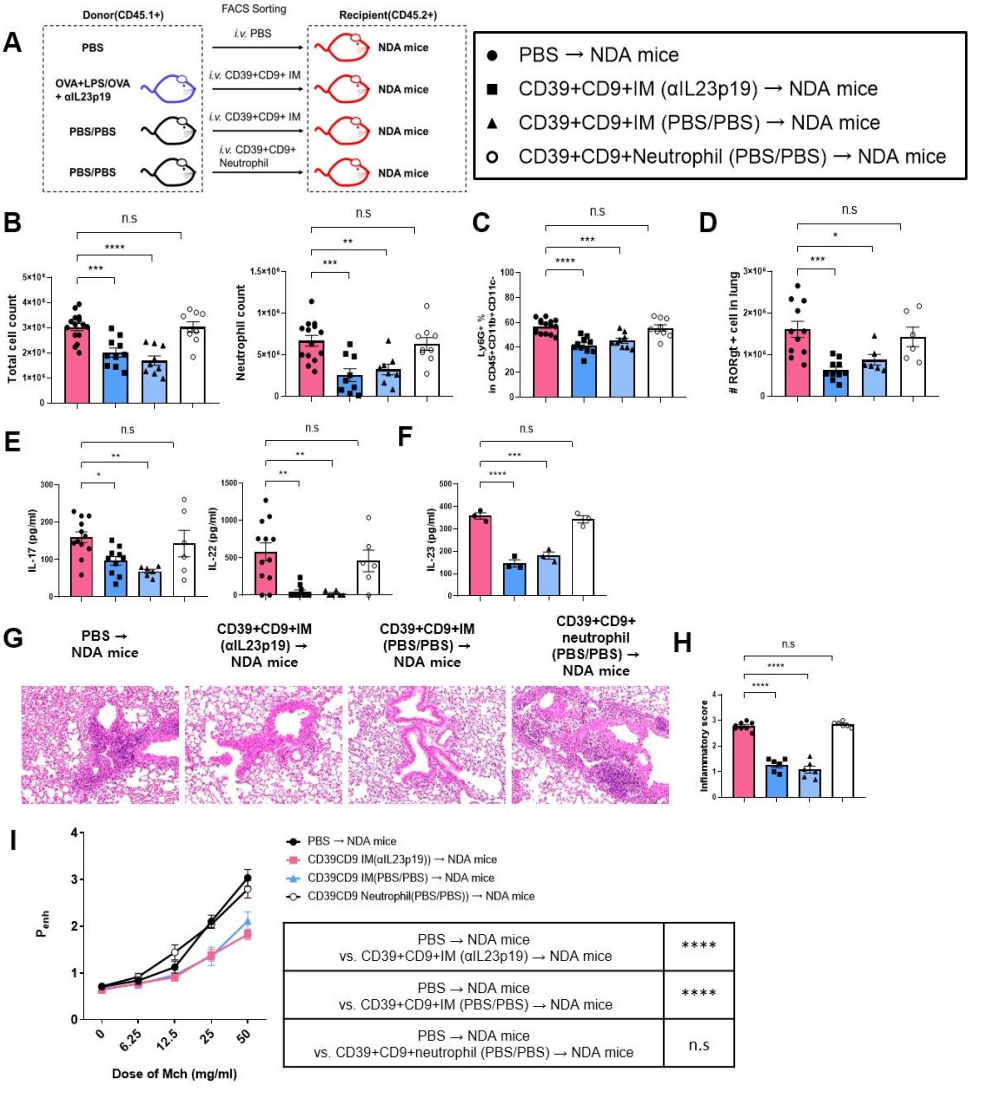

PBS → NDA mice vs. CD39+CD9+IM (αIL23p19) → NDA mice	****
PBS → NDA mice vs. CD39+CD9+IM (PBS/PBS) → NDA mice	****
PBS → NDA mice vs. CD39+CD9+neutrophil (PBS/PBS) → NDA mice	n.s

Figure 11. $CD39^+CD9^+$ IMs from PBS/PBS or OVA+LPS/OVA+αIL-23p19 suppress Th17-mediated neutrophilic inflammation in NDA mice. (A) Schematic diagram of adoptive transfer protocol. $CD39^+CD9^+$ IMs or $Ly6G^+CD39^+CD9^+$ neutrophils were sorted from OVA+LPS/OVA+αIL-23p19 or PBS/PBS mice on day 24, which were intravenously transferred on every challenge to the NDA mouse model. (B-F) Total cell and neutrophil counts (B) in BALF, percentages of $Ly6G^+$ neutrophils (C) and $RORgt^+$ cells in $CD4^+$ T cells (D) in the lung, and levels of IL-17 and IL-22 (E) and IL-23 (F) in BALF measured at 48 h after the last challenge under the indicated conditions. (G, H) Representative images of H&E staining (G) and inflammatory scores quantified from H&E staining (H). (I) Dynamic airway resistance on methacholine inhalation measured over multiple doses of Mch under the indicated conditions. n = 3–15 mice per group (A-I). Data are shown as mean ± s.e.m. $*P < 0.05$, $**P < 0.01$, $***P < 0.001$, and $****P < 0.0001$ using one-way ANOVA with Tukey's post hoc correction (B-F, H) and two-way ANOVA with Sidak's post hoc correction (I).

6. $CD39^+CD9^+$ IMs suppress IL-23-mediated Th17 cell activation and neutrophilic inflammation by inhibiting NETosis

We next investigated how $CD39^+CD9^+$ IMs suppress IL-23-mediated neutrophilic inflammation in NDA mice. CD39 is reported to suppress formation of neutrophil extracellular traps, called NETosis, in venous thrombosis mouse models[105], suggesting the association of CD39 with NETosis in NDA model. To test this possibility, we first compared the extent of NETosis in the lungs by measuring citrullinated histone H3 (citH3)- and MPO-positive NET-stained areas in OVA+LPS/PBS, OVA+LPS/OVA, OVA+LPS/OVA +GSK484 (NETosis inhibitor), and OVA+LPS/OVA+αIL-23p19. NETosis was increased in OVA+LPS/OVA, compared to in OVA+LPS/PBS, which was significantly attenuated by GSK484 or αIL-23p19 (Fig. 12A, B). Moreover, the attenuated NETosis in OVA+LPS/OVA+αIL-23p19 was increased back to the level in OVA+LPS/OVA by POM1 treatment, which was re-attenuated by GSK484 treatment (OVA+LPS/OVA+αIL-23p19+POM1+GSK484 in Fig. 12A, B). Although CD9 has not been reported to be involved in NETosis in allergic airway inflammation, αCD9 treatment led to similar results to POM1 treatment (Fig. 12A, B). Moreover, co-treatment of POM1 and αCD9 showed the same increasing effect on NETosis with the individual treatment, and the extent was similar between co-treatment and individual treatment (Fig. 13A, B). Furthermore, the effects of POM1 or αCD9 on Th17 cell activation, neutrophilic inflammation, and P_{enh} values (Fig. 12C-I), as well as IL-23 level and $CD39^+CD9^+$ IM percentage (Fig. 12J, K), in OVA+LPS/OVA+αIL-23p19 were abolished by GSK484. These inhibition results suggest the possibility that $CD39^+CD9^+$ IMs inhibit NETosis. To test the possibility, we performed the aforementioned adoptive transfer of $CD39^+CD9^+$ IMs and found that transferred $CD39^+CD9^+$ IMs suppressed NETosis (Fig. 12L, M). Taken together, these

results suggest that $CD39^+CD9^+$ IMs suppress Th17 cell activation and neutrophilic inflammation by inhibiting NETosis.

We showed above that Th17 cell activation significantly contributed to neutrophilic inflammation. Thus, we questioned whether Th17 cell activation could also affect NETosis. αIL-17 treatment strongly reduced the increased NETosis in OVA+LPS/OVA (Fig. 13C, D), consistent with its inhibition of neutrophilic inflammation in the lung (Fig. 13E) and BALF (Fig. 1H, I). On the other hand, inhibition of NETosis in OVA+LPS/OVA by GSK484 decreased the IL-23 level in BALF (OVA+LPS/OVA+GSK484 in Fig. 12J). In addition, when the increased NETosis in OVA+LPS/OVA+αIL-23p19+POM1 or αCD9 was re-attenuated by GSK484 as described above (Fig. 12A, B), the IL-23 level was also decreased. These data suggest that NETosis positively regulates the IL-23 level. Intriguingly, αIL-17 treatment also increased $CD39^+CD9^+$ IMs in OVA+LPS/OVA (Fig. 13F), possibly due to the decreased NETosis and thus IL-23 level. Combining all these results, given that IL-23 inhibits $CD39^+CD9^+$ IMs that suppress NETosis, provides a model (Fig. 13G) describing regulatory relationships among the five components (IL-23, Th17 cell activation, neutrophilic inflammation, NETosis, and $CD39^+CD9^+$ IMs). This model demonstrates that $CD39^+CD9^+$ IMs serve as a regulatory axis that inhibits NETosis (Pathways 4-5 in the model) as a potent endogenous brake to suppress the IL-23-mediated Th17 cell activation-neutrophilic inflammation axis (Pathways 1-3 in the model). Importantly, $CD39^+CD9^+$ IMs are entangled for regulatory purpose with the other four components in the model, suggesting their importance as an endogenous brake comparable to that of the IL-23-Th17-neturophil pathway. Of note, Dex treatment showed no significant effect on NETosis, neutrophil percentage in the lung, and $CD39^+CD9^+$ IMs (Fig. 13H-K), indicating Dex resistance in NDA mice.

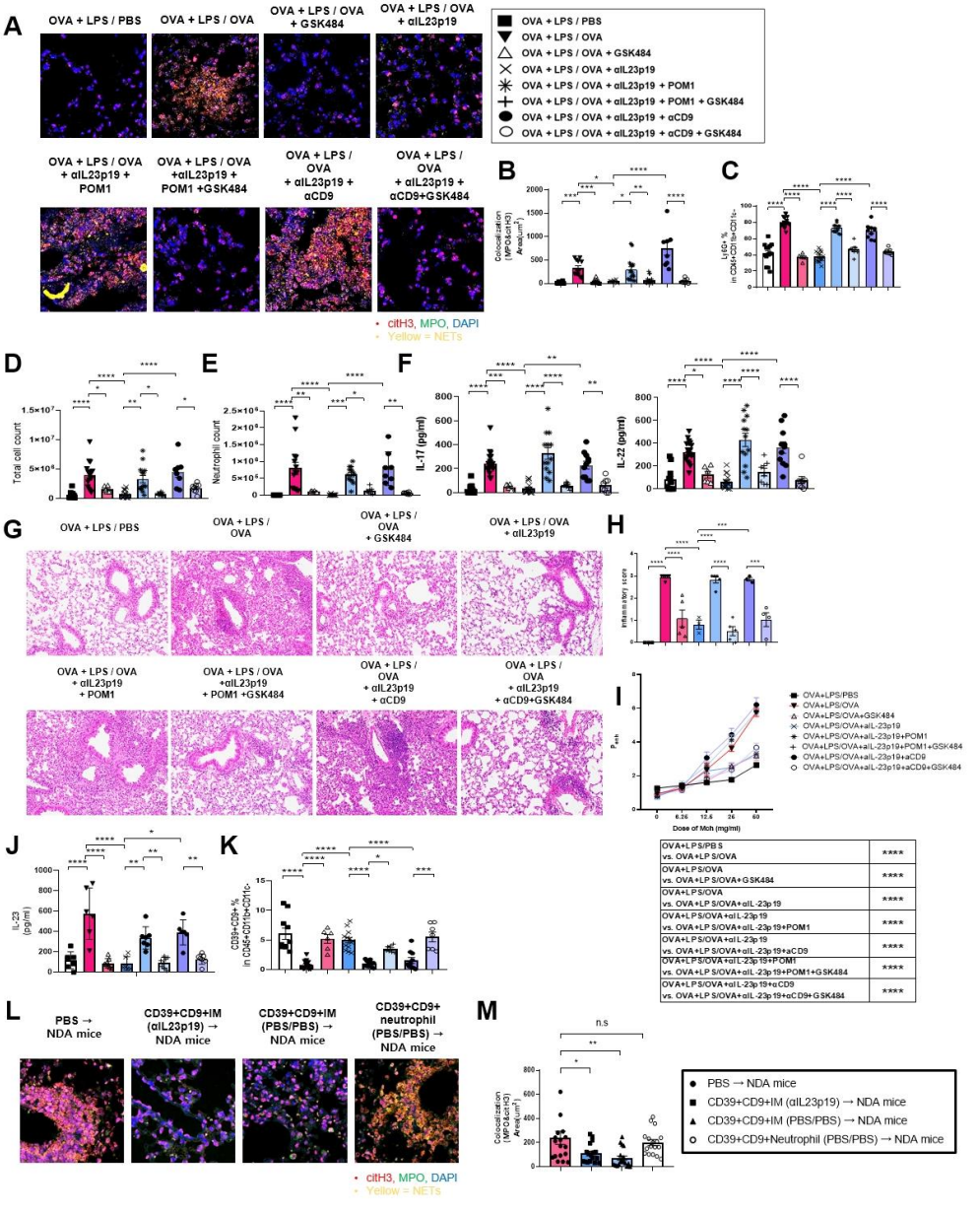

OVA+LPS/PBS vs. OVA+LPS/OVA	****
OVA+LPS/OVA vs. OVA+LPS/OVA+GSK484	****
OVA+LPS/OVA vs. OVA+LPS/OVA+αIL-23p19	****
OVA+LPS/OVA+αIL-23p19 vs. OVA+LPS/OVA+αIL-23p19+POM1	****
OVA+LPS/OVA+αIL-23p19 vs. OVA+LPS/OVA+αIL-23p19+αCD9	****
OVA+LPS/OVA+αIL-23p19+POM1 vs. OVA+LPS/OVA+αIL-23p19+POM1+GSK484	****
OVA+LPS/OVA+αIL-23p19+αCD9 vs. OVA+LPS/OVA+αIL-23p19+αCD9+GSK484	****

Figure 12. $CD39^+CD9^+$ IMs are critical for αIL-23p19-dependent suppression of neutrophilic inflammation via inhibition of NETosis. (A) Representative images of lung immunostaining for citrullinated histone H3 (citH3, red), MPO (green), and DAPI (blue). $citH3^+MPO^+$ NETs are shown in yellow. (B) Colocalization area (μm^2) of $citH3^+MPO^+$ NETs in each FOV quantified using Zen software. (C-F) $Ly6G^+$ neutrophil percentage in the lung (C), total cell (D) and neutrophil (E) counts in BALF, and IL-17 and IL-22 levels (F) in BALF. Representative images of H&E staining (G) and inflammatory scores quantified from H&E staining (H). (I) Dynamic airway resistance on methacholine inhalation measured under the indicated conditions. (J, K) IL-23 level in BALF (J) and percentages of $CD39^+CD9^+$ IMs in $CD45^+CD11b^+CD11c^-$ cells (K) in the lung under the indicated conditions. (L, M) Representative images of lung immunostaining (L) and colocalization area (μm^2) of $citH3^+MPO^+$ NETs (M) in adoptive transfer models. n = 5–12 mice per group (A-M). Data are shown as mean ± s.e.m. $^*P < 0.05$, $^{**}P < 0.01$, $^{***}P < 0.001$, and $^{****}P < 0.0001$ using one-way ANOVA with Tukey's post hoc correction (B-F, H, J, K, M) and two-way ANOVA with Sidak's post hoc correction (I).

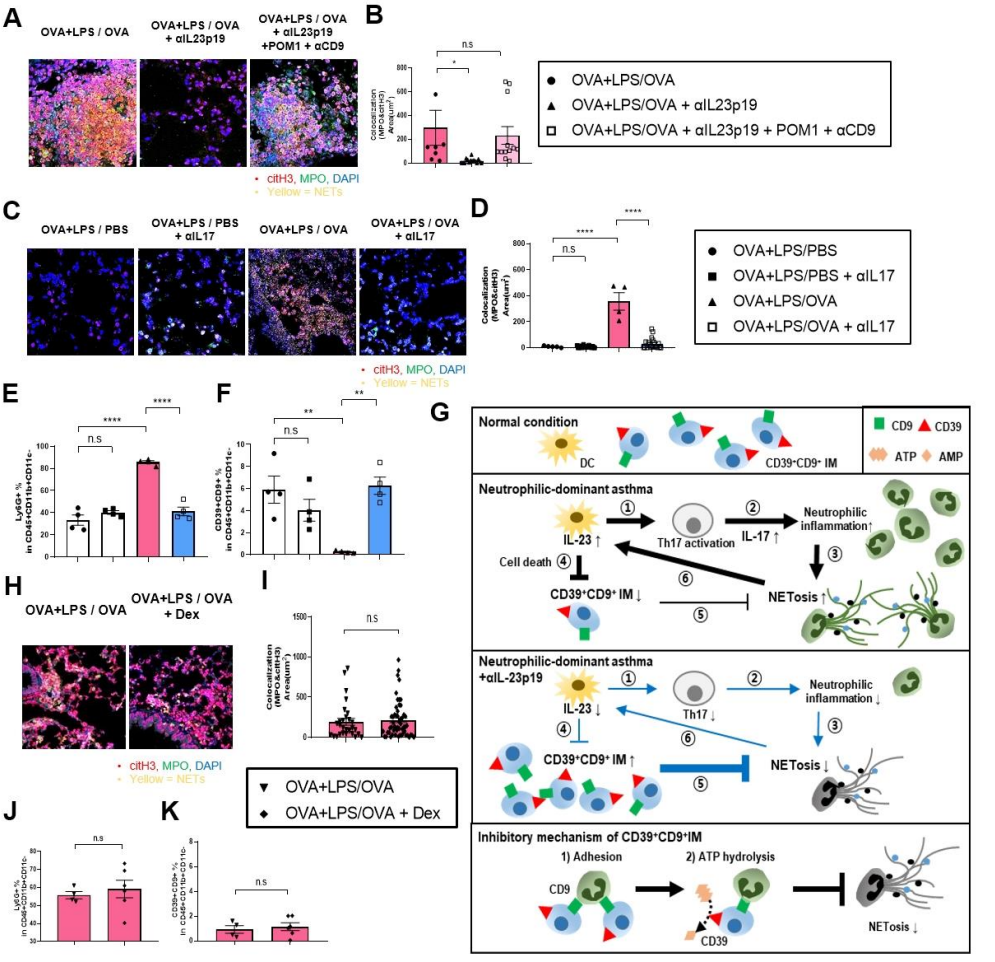

Figure 13. $CD39^+CD9^+$ IMs suppress IL-23-mediated Th17 cell activation and neutrophilic inflammation by inhibiting NETosis. (A, C, H) Representative confocal microscopy images of immunostaining for citH3 (red), MPO (green), and DAPI (blue). $citH3^+MPO^+$ NETs are shown in yellow. (B, D, I) Colocalization area (μm^2) of $CitH3^+MPO^+$ NETs in each FOV quantified using Zen software. (E, F, J, K) Percentages of $Ly6G^+$ neutrophils (E, J) and $CD39^+CD9^+$ IMs (F, K) in the lung. (G) A proposed model describing regulatory relationships among the five components (IL-23, Th17 cell activation, neutrophil inflammation, NETosis, and $CD39^+CD9^+$ IMs) in OVA+LPS/PBS, OVA+LPS/LPS, and OVA+LPS/OVA+αIL-23p19. A model describing potential roles of CD9 and CD39 in direct suppression of NETosis by $CD39^+CD9^+$ IMs is also shown in the bottom: CD9-mediated adhesion of $CD39^+CD9^+$ IMs to neutrophils, followed by CD39-mediated ATP hydrolysis that may contribute to suppression of NETosis. n = 4–8 mice per group (A-F, H-K). Data are shown as mean ± s.e.m. $*P < 0.05$, $**P < 0.01$, $***P < 0.001$, and $****P < 0.0001$ using one-way ANOVA with Tukey's post hoc correction (B, D-F) or Student's T-test (I-K).

7. $CD39^+CD9^+$ IMs directly inhibit NETosis of neutrophils derived from NDA mice in CD39 and CD9-dependent manner

We next investigated whether $CD39^+CD9^+$ IMs directly inhibit NETosis or via other indirect mechanisms. To this end, we isolated $Ly6G^+CD11b^+CD11c^-$ neutrophils and $CD39^+CD9^+$ IMs from mouse lungs in OVA+LPS/OVA and OVA+LPS/OVA+αIL-23p19, respectively. We then analyzed the NETosis of the isolated neutrophils in the presence or absence of $CD39^+CD9^+$ IMs (Fig. 15A). Interestingly, high levels of NETosis were observed in the absence of $CD39^+CD9^+$ IMs, whereas NETosis was significantly decreased in the presence of $CD39^+CD9^+$ IMs (Fig. 14A, B). As seen in the adoptive transfer (Fig. 12L, M), $CD39^+CD9^+$ IMs isolated from untreated control mice (PBS/PBS) also showed similar inhibition effects on NETosis to those from OVA+LPS/OVA+αIL-23p19 mice (Fig. 15B-D). However, the inhibition of NETosis by $CD39^+CD9^+$ IMs was abolished by POM1 treatment while it was not observed when $CD39^-CD9^-$ monocytes were used instead of $CD39^+CD9^+$ IMs (Fig. 14A, B). To examine whether $CD39^+CD9^+$ IM-mediated ectonucleotidase activity is responsible for suppressing NETosis *ex vivo*, we analyzed NETosis in the presence of $CD39^+CD9^+$ IMs after treatment with various concentrations of ATP. Suppression of NETosis by $CD39^+CD9^+$ IMs was reversed by 1 or 100 μM of ATP, but not by 0.01 or 0.1 μM of ATP (Fig. 14A, B). These data indicate that CD39 within $CD39^+CD9^+$ IMs directly inhibits NETosis through ATP hydrolysis. Moreover, we investigated whether CD9, a tetraspanin protein involved in cell adhesion, within $CD39^+CD9^+$ IMs also can directly suppress NETosis. To this end, we tested whether $CD39^+CD9^+$ IMs were attached to neutrophils 2 h after adding $CD39^+CD9^+$ IMs to neutrophils. MHCII-positive $CD39^+CD9^+$ IMs (red in Fig. 14C, D) were physically attached to neutrophils (non-red in Fig. 14C, D), while neutrophils were scattered in the absence of $CD39^+CD9^+$ IMs or in the presence of $CD39^-CD9^-$ monocytes (Fig.

14C, D). However, neutrophils held by $CD39^+CD9^+$ IMs were separated by αCD9 treatment (Fig. 14C, D). Moreover, the attachment of $CD39^+CD9^+$ IMs to neutrophils drastically decreased NETosis (Fig. 14E, F), while no attachment by $CD39^-CD9^-$ monocytes or the deceased attachment by αCD9 treatment led to the induction of NETosis (Fig. 14E, F). These data indicate that CD9 contributes to the attachment of $CD39^+CD9^+$ IMs to neutrophils, which is required for the inhibition of NETosis by $CD39^+CD9^+$ IMs. Although the attachment of $CD39^+CD9^+$ IMs to neutrophil was not blocked by POM1 treatment or ATP addition (Fig. 14C, D), high amounts of ATP nearby neturophils still induce NETosis (Fig. 14E, F). Taken together, our results indicate that both CD9 and CD39 on $CD39^+CD9^+$ IMs are required for the suppression of NETosis in NDA conditions: $CD39^+CD9^+$ IMs first attach to neutrophils in a CD9-dependent manner, and then remove ATP molecules near neutrophils in a CD39-dependent manner.

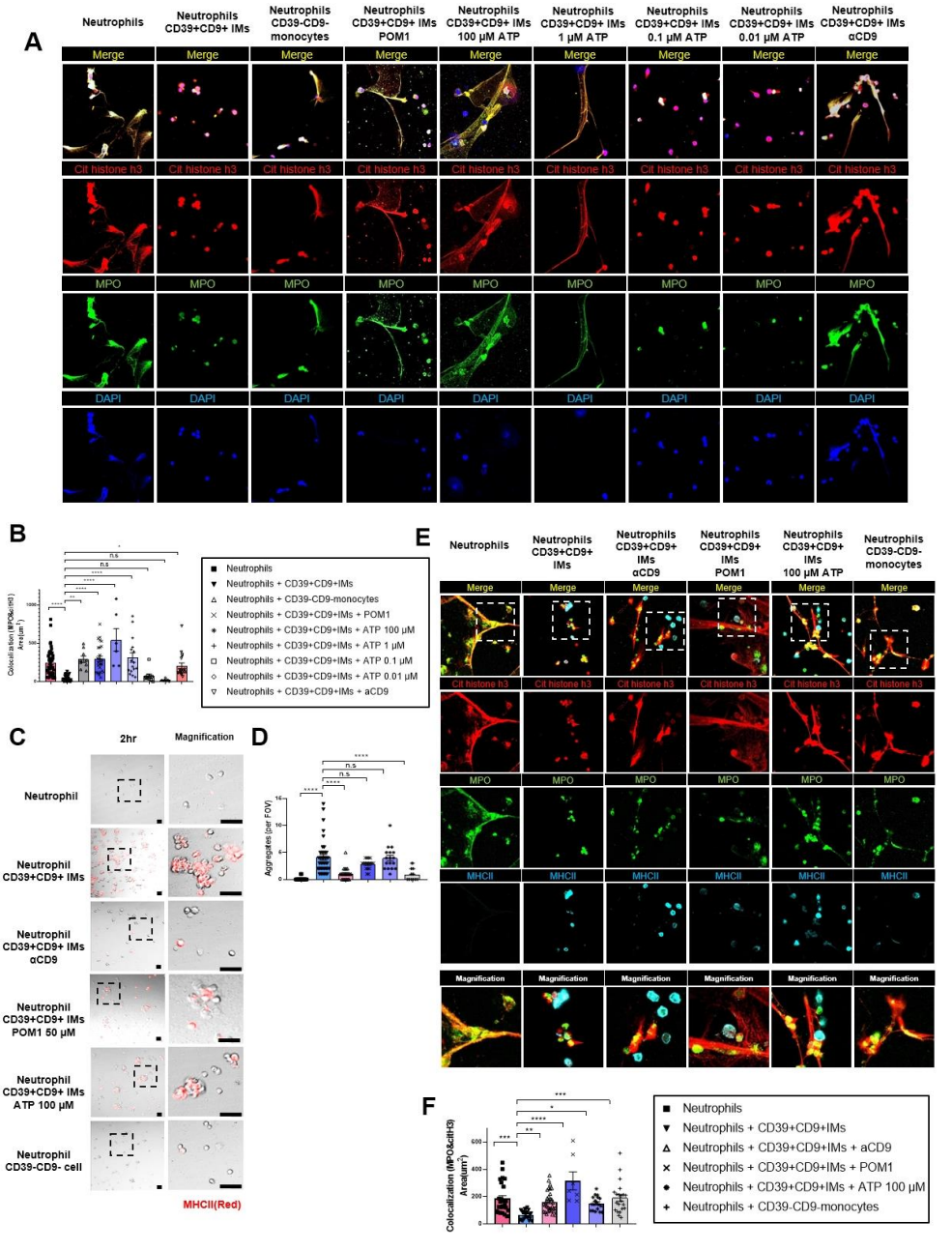

Figure 14. $CD39^+CD9^+$ IMs directly inhibit NETosis of neutrophils derived from NDA mice in CD39 and CD9-dependent manner. (A) Representative confocal microscopy images of immunostaining for citH3 (red), MPO (green), and DAPI (blue) in co-cultured slides. Merged $citH3^+MPO^+$ NETs are shown in yellow. $Ly6G^+$ neutrophils were co-cultured with $CD39^+CD9^+$ IMs or $CD39^-CD9^-$ monocytes on chamber slides. (B) Colocalization area (μm^2) of $citH3^+MPO^+$ NETs in each FOV quantified using Zen software. (C) Representative photomultiplier tube (PMT) images showing immunostaining for MHCII (red) taken after 2 h in the co-culture system. (D) Number of cell aggregates per FOV. Aggregates were defined as cells that adhered to at least five other cells. (E) Representative confocal microscopy images of immunostaining for citH3 (red), MPO (green), and MHCII (blue) in co-cultured slides. (F) Colocalization area (μm^2) of $citH3^+MPO^+$ NETs in each FOV. n = 4-10 samples per group (B, D, F). Data are shown as mean ± s.e.m. $*P < 0.05$, $**P < 0.01$, $***P < 0.001$, and $****P < 0.0001$ using one-way ANOVA with Tukey's post hoc correction.

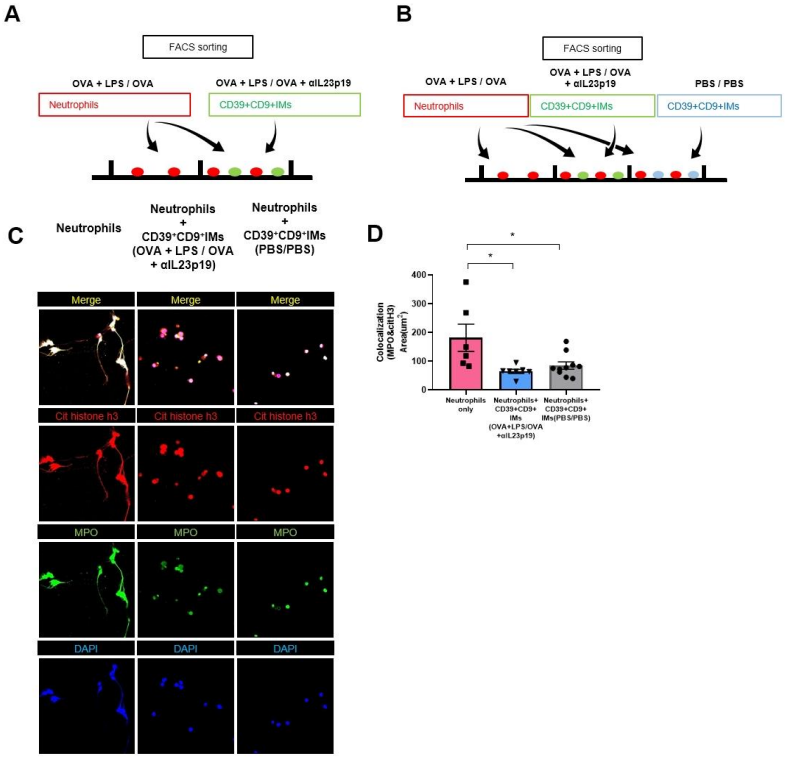

Figure 15. CD39$^+$CD9$^+$ IMs isolated from control mice lung directly inhibit neutrophils derived NETosis from NDA mice. (A) Schematic diagram of experiments from which the results are presented in Fig.7. (B) Schematic diagram of experiments from which the results are presented in (C, D**)**. In these experiments, neutrophils sorted from OVA+LPS/OVA were co-cultured with CD39$^+$CD9$^+$ IMs sorted from OVA+LPS/OVA+αIL-23p19 or CD39$^+$CD9$^+$ IMs sorted from PBS/PBS, and the co-cultured cells are then analyzed. (C) Confocal microscopy images of co-cultured slides immunostaining for citH3 (red), MPO (green), and DAPI (blue). Merged citH3+MPO+ NETs are shown in yellow. (D) Colocalization area (μm^2) of citH3$^+$MPO$^+$ NETs per FOV. Data are shown as mean ± s.e.m. *P < 0.05 using one-way ANOVA with Tukey's post hoc correction (D).

8. $CD39^+CD9^+$ IMs consistently regulate Th17 cell activation and neutrophilic inflammation by inhibiting NETosis in house dust mite (HDM)-driven asthma model

Recently, asthma models driven from allergen extracts, such as house dust mite (HDM), have been used widely instead of OVA-based models[106,107]. To examine the validity of the IL-23-$CD39^+CD9^+$ IMs-NETosis pathway for neutrophilic inflammation in these models, we established intra-nasal sensitization (HDM and LPS) and challenge (HDM) protocols for an HDM-driven asthma model as previously described[106,107]. Specifically, the doses of HDM (25 μg for sensitization and 6.25 μg for challenging) and LPS (10 μg for sensitization) were determined as those used to establish an HDM model showing Th17 inflammation and neutrophilic inflammation[107] (Fig. 16A). Total cell and neutrophil counts in BALF, $ROR\gamma t^+$, $T\text{-}bet^+$, and $GATA3^+$ T cell counts in lung tissues, and IL-17, IL-23, and IFN-γ levels in BALF, as well as immune cell infiltration (Fig. 16B-I), NETosis, and P_{enh} values (Fig. 16J-L), were significantly increased in HDM+LPS/HDM compared to in the control HDM+LPS/PBS. Although $ROR\gamma t^+$, $T\text{-}bet^+$, and $GATA3^+$ cells were increased in HDM+LPS/HDM, $ROR\gamma t^+$ cell count (~ 5×10^4) was much higher than those of $T\text{-}bet^+$ cells (~ 1×10^4), and $GATA3^+$ cells (~ 2.0×10^3) in HDM+LPS/HDM (Fig. 16D-F), suggesting the major contribution of Th17 cells to neutrophilic inflammation in the HDM model. These increases were attenuated by αIL-23p19, which were restored back to the level before αIL-23p19 treatment by treatment of POM1 or αCD9. All these results are consistent with those observed in our OVA-driven NDA mice. These results collectively suggest that $CD39^+CD9^+$ IMs regulate Th17 cell activation and neutrophilic inflammation by inhibiting NETosis in both OVA- and HDM-driven asthma models.

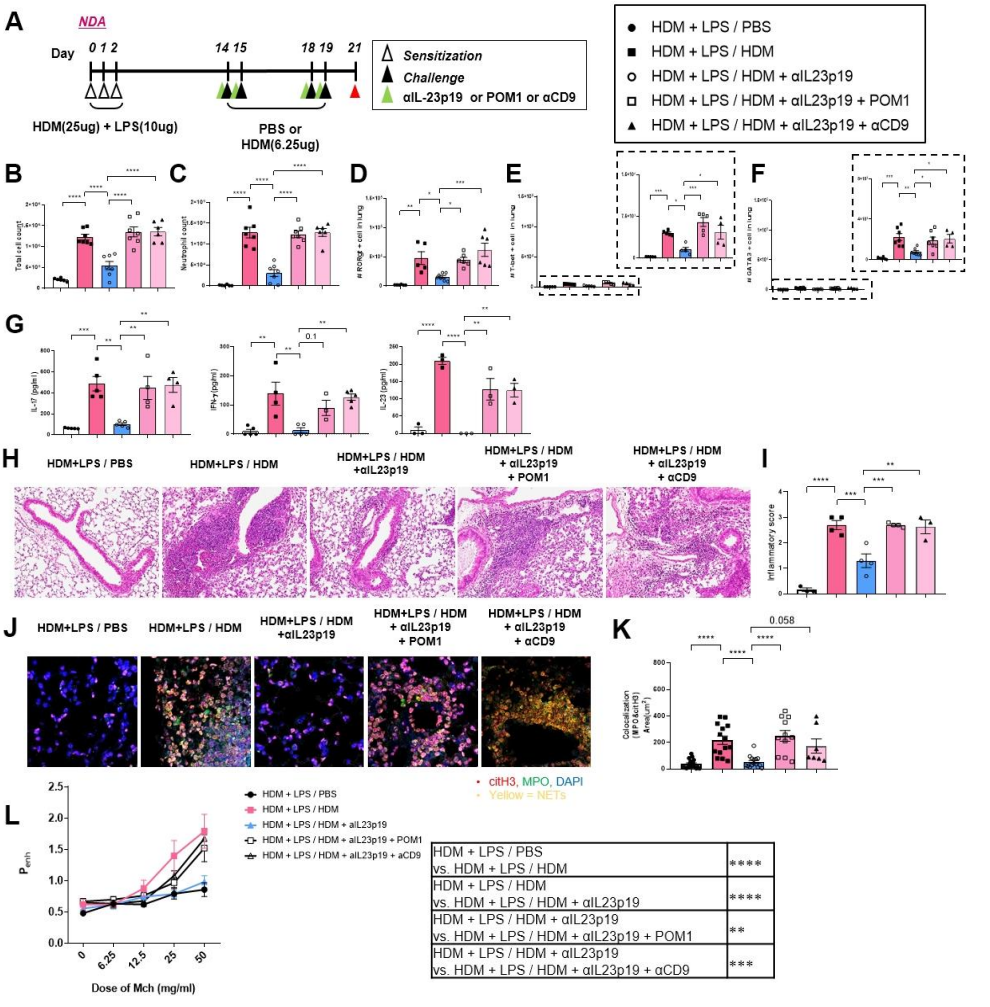

HDM + LPS / PBS vs. HDM + LPS / HDM	****
HDM + LPS / HDM vs. HDM + LPS / HDM + αIL23p19	****
HDM + LPS / HDM + αIL23p19 vs. HDM + LPS / HDM + αIL23p19 + POM1	**
HDM + LPS / HDM + αIL23p19 vs. HDM + LPS / HDM + αIL23p19 + αCD9	***

Figure 16. CD39$^+$CD9$^+$ IMs regulate Th17 cell activation and neutrophilic inflammation by inhibiting NETosis in house dust mite (HDM)-driven asthma models. (A) Schematic diagram of allergen sensitization and challenge protocol used for establishing an HDM-driven asthma model. In HDM-driven mouse model, sensitization with PBS or HDM+LPS intranasally (i.n.) was followed by challenge with PBS or HDM (i.n.) at the indicated days. αIL-23p19, POM1, or αCD9 was treated at 1 h before every challenge period. The inflammatory response was assessed at 48 h after the last challenge. (B-H) Total cell (B) and neutrophil (C) counts in BALF; RORgt$^+$ (D), T-bet $^+$ (E), and GATA3$^+$ (F) cells in CD4$^+$ T cell in the lung; and levels of IL-17, IFN-g, and IL-23 (G) in BALF measured in the indicated conditions. (H) Representative H&E staining of lung sections obtained from the indicated conditions. (I) inflammatory scores quantified from H&E staining. (J) Representative confocal microscopy images of immunostaining for citH3 (red), MPO (green), and DAPI (blue). Merged citH3+MPO+ NETs are shown in yellow. (K) Colocalization area (μm2) of citH3$^+$MPO$^+$ NETs in each FOV. (L) P_{enh} values over multiple doses of Mch measured in the indicated conditions. n = 3–7 mice per group (B-L). Data are shown as mean ± s.e.m. *P < 0.05, **P < 0.01, ***P < 0.001, and ****P < 0.0001 using one-way ANOVA with Tukey's post hoc correction (B-G, I, K) and two-way ANOVA with Sidak's post hoc correction (L).

9. CD39$^+$CD9$^+$ IMs or immune cells are inversely correlated with severity of airway inflammatory diseases

To investigate clinical relevance of CD39$^+$CD9$^+$ IMs, we first obtained three RNA expression profiles of lung tissues collected from asthma patients via bronchial biopsy [U-BIOPRED (GSE76225)] or endobronchial brushing [SARP (GSE63142) and IMSA (GSE158752)] from Gene Expression Omnibus (GEO) database. For each dataset, we then estimated the fractions of CD39$^+$CD9$^+$ IMs in individual samples through cell type deconvolution analysis based on DEGs for RNA CM-C3 representing CD39$^+$CD9$^+$ IMs (Fig. 3I) using CIBERSORTx[71]. Since the information for neutrophilic inflammation (e.g., blood neutrophil count) are not provided in these datasets by the original studies, we next examined the relationships of the estimated CD39$^+$CD9$^+$ IM fractions with asthma severity. The results revealed that severe asthmatic patients tended to have lower fractions of CD39$^+$CD9$^+$ IMs than mild/moderate asthmatic patients consistently in all three datasets (Fig. 17A, B).

CRS, another upper airway inflammatory disease, was shown to have high numbers of neutrophils and extracellular DNA[108]. Thus, we next analyzed the percentages of neutrophils or CD39$^+$CD9$^+$CD45$^+$ cells and their relationships with CRS severity in 25 CRS patients- 13 mild and 12 moderate-severe patients with Lund-Mackay score (LMS) less and larger than 10, respectively[79]. Moderate-severe CRSwNP patient group showed significantly higher percentages of neutrophils (CD45$^+$CD16$^+$ cells) in the ethmoid mucosa than mild patient group (Fig. 17C). In contrast, the percentage difference was not significant for eosinophils (CD45$^+$CD193$^+$ cells) (Fig. 17D). Correspondingly, the moderate-severe group showed a higher MPO-positive neutrophil count than the mild group (Fig. 17E), as previously reported[109]. Interestingly, the percentage of CD39$^+$CD9$^+$CD45$^+$ cells were inversely correlated with CRSwNP severity (Fig. 17F, G). IHC analysis further showed

the presence of $CD39^+CD9^+CD45^+$ cells in ethmoid mucosa of mild patients, but virtually no detection in moderate-severe patients (Fig. 17H). These results suggest that $CD39^+CD9^+CD45^+$ cells were reduced in severe CRSwNP patients with higher neutrophilic inflammation. Using a previously reported proteome dataset[80,81] generated from colon tissues of healthy controls (HC; n=7) and patients with ulcerative colitis (UC; n=7) and Crohn's disease (CD; n=7), examined the level of CD39 and CD9 and found that CD9 level tended to be lower in UC and CD samples than in HC samples (Fig. 18A, B). The IHC analysis showed that $CD39^+CD9^+CD45^+$ cells were reduced in UC and CD (Fig. 18C). Taken together, all these results suggest that $CD39^+CD9^+$ immune cells can serve as potential indicators of severity of airway neutrophilic inflammatory diseases.

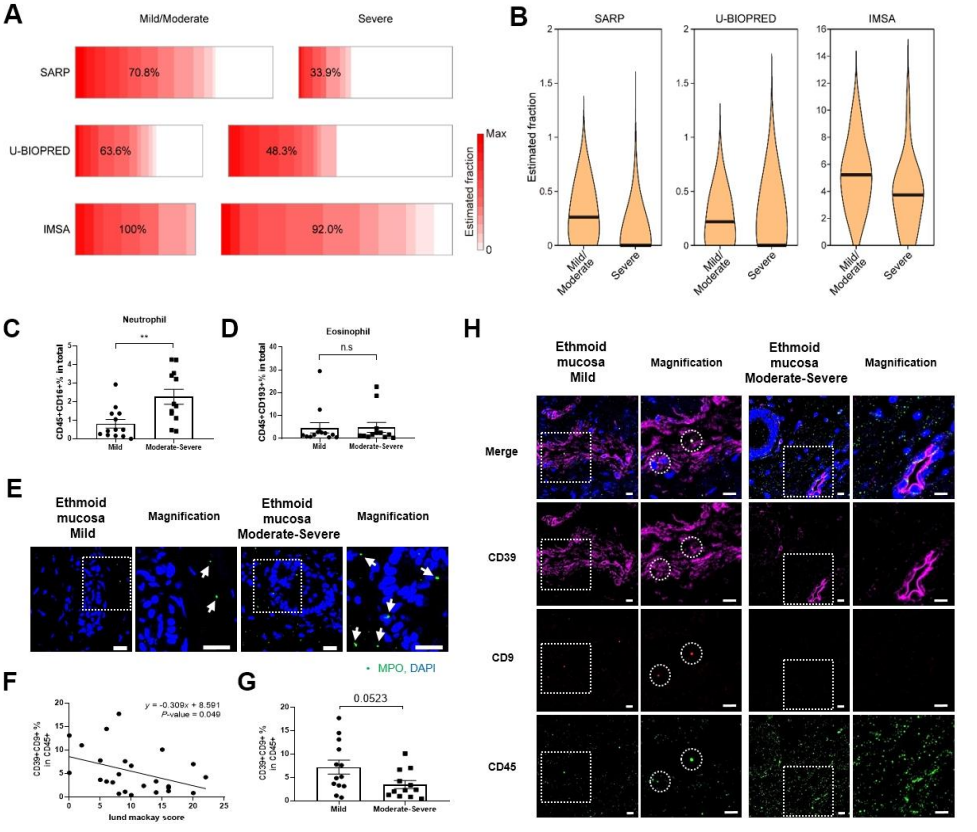

Figure 17. $CD39^+CD9^+$ IMs or immune cells are inversely correlated with severity of airway inflammatory diseases. (A) Heat maps showing the fractions of RNA CM-C3 estimated by CIBERSORTx in individual samples collected from mild/moderate (left) and severe (right) asthma patients in the three cohorts (SARP, U-BIOPRED, and IMSA). Color bar, gradient of the estimated fractions. The number on each heat map denotes the percentage of samples with non-zero estimated fraction. (B) Violin plots showing distributions of the estimated fractions of RNA CM-C3 in patient groups with mild/moderate and severe asthma in the three cohorts. Center line, median value. (C, D) Percentages of neutrophils ($CD45^+CD16^+$, C) and eosinophils ($CD45^+CD193^+$, D) in ethmoid mucosa cells in patients with mild (LMS< 10, n = 13) or moderate-severe (LMS > 10, n = 12) with CRS. (E) Representative confocal microscopy images of immunostaining for MPO (green) and DAPI (blue) over the severity. MPO^+ granules are shown as arrows. (F) Negative correlation between the percentage of $CD39^+CD9^+$ cells in $CD45^+$ cells and LMS. Linear regression results are shown. (G) Percentage of $CD39^+CD9^+$ cells in $CD45^+$ cells of ethmoid mucosa in mild or moderate-severe patients. (H) Representative confocal microscopy images of immunostaining for CD9 (red), CD39 (purple), and CD45 (green). Merged $CD45^+CD39^+CD9^+$ cells are shown as circles. Data are shown as mean ± s.e.m. $*P < 0.05$ and $**P < 0.01$ using a Mann-Whitney test (C, D, F, G).

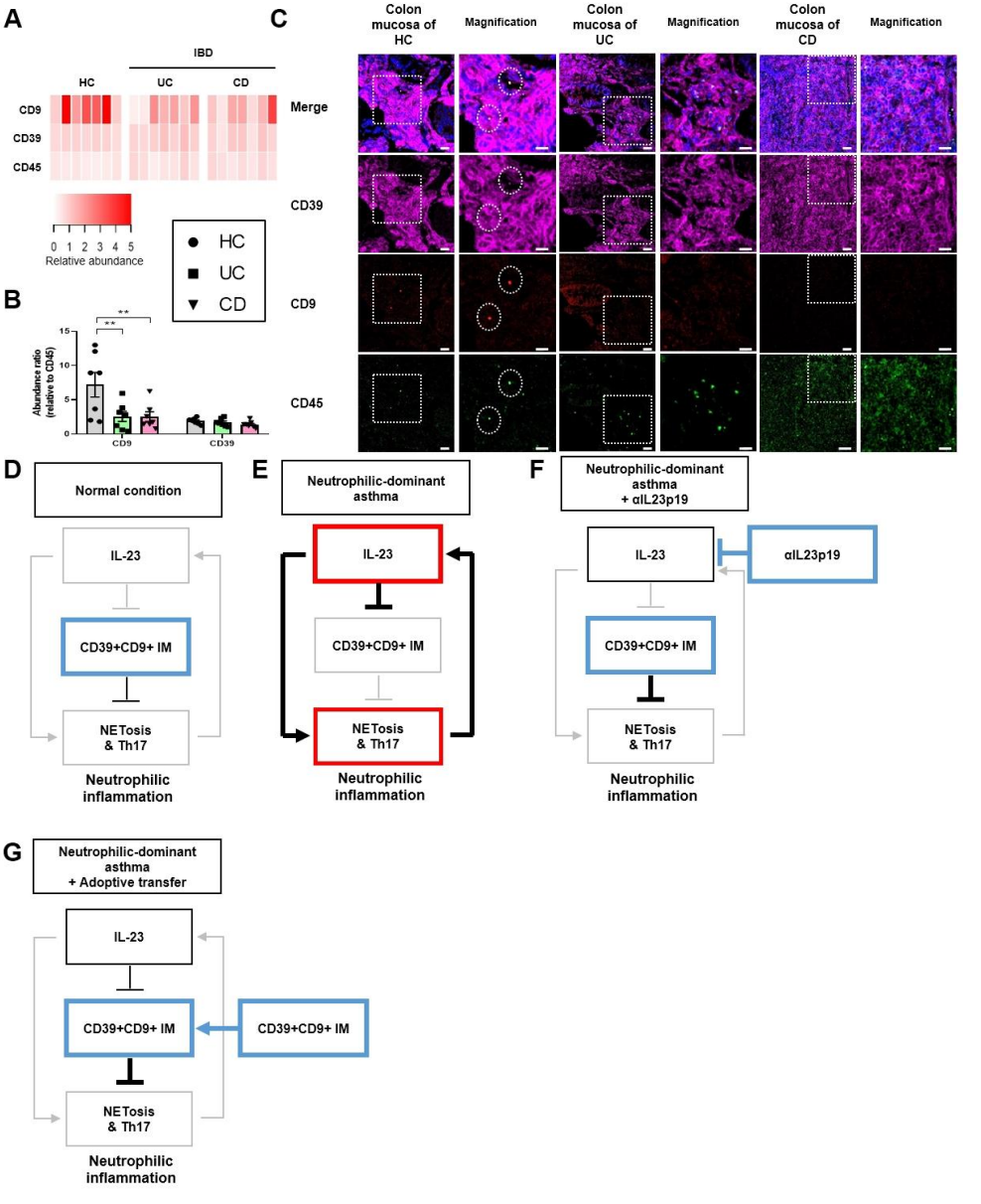

Figure 18. $CD39^+CD9^+$ immune cells are reduced in colon of IBD patients. (A) Heat map showing relative abundances of CD9, CD39, and CD45 proteins in the colon mucosa of seven healthy controls (HC) 14 IBD patients, including seven patients with ulcerative colitis (UC) and seven patients with Crohn's disease (CD). The protein abundances were obtained from the proteome data we previously reported. (B) Protein abundance ratios of CD9 or CD39 to CD45 in HC, UC, and CD groups. Data are shown as mean ± s.e.m. $*P < 0.05$ and $**P < 0.01$, using one-way ANOVA with Tukey's post hoc correction. (C) Representative confocal microscopy images of human colon mucosa from HC and patients with UC and CD immunostaining for CD9 (red), CD39 (purple), and CD45 (green). Merged $CD45^+CD39^+CD9^+$ cells are indicated by circle. (D-G), Schematic diagrams describing the regulatory relationships among IL-23, $CD39^+CD9^+$ IMs, and NETosis/Th17 cell activation in normal condition (D), neutrophilic-dominant asthmatic (NDA) condition (E), αIL23p19 treated NDA condition (F), and $CD39^+CD9^+$ IM transferred NDA condition (G). In each condition, the components promoting or inhibiting NETosis/Th17 cell activation are indicated by blue or red boxes, respectively, and the regulatory reactions strongly activated are indicated by thick lines (arrow for activation and inhibition symbol for suppression).

IV. DISCUSSION

In Part 1, our study found that *S. aureus* infection resulted in higher levels of neutrophil infiltration and lung injury in NOX4 KO mice compared to WT mice, indicating a protective role for NOX4 in the host response. NOX4 is a protein involved in both the production and sensing of ROS in various types of cells, including endothelial cells[110,111], epithelial cells[112,113], and monocytes[114,115]. NOX4 has been demonstrated to play a dual function in lung infections in different cell types. It can either contribute to or reduce host damage. For instance, following *P. aeruginosa* infection, NOX4 was found to increase nuclear ROS and trigger chromatin remodeling in lung epithelial cells, leading to host injury[116]. On the other hand, NOX4-mediated ROS has been reported to promote the production of macrophage migration inhibitory factor, which aids in resisting *T. gondii*, indicating a protective role for NOX4 in the host[28]. Thus, our study provides evidence supporting the protective role of endothelial NOX4 in the host during lung infection. The role of NOX4 in the immune response after infection has been a topic of debate in previous studies, and although its function has been examined in response to various pathogens, its interaction with endothelial NOX4 and *S. aureus* has not been explored until our study. Therefore, we discovered a novel finding: endothelial NOX4 plays a role in reducing lung injury after *S. aureus* infection. Nevertheless, more research is required using specific conditional KO mice for NOX4 deletion in endothelial cells to fully comprehend the immunological function of endothelial NOX4 against *S. aureus* infection.

Endothelial ICAM1 is an adhesion molecule that is responsible for the recruitment of monocytes and neutrophils[84,117-119]. Monocyte recruitment is dependent on ICAM1 expression in endothelial cells in response to specific pathogen or stimuli[117]. Moreover, N-glycosylation of endothelial ICAM1 has been shown to influence the recruitment of specific monocyte subsets to sites of

inflammation[120,121]. Specifically, high mannose ICAM1 exhibits a selective function in binding to $CD16^+$ monocytes, while not interacting with $CD16^-$ monocytes or neutrophils[9]. Furthermore, NOX4 has been associated with inducing specific binding between ICAM1 and monocytes in endothelial cells[26,84]. These studies lend support to our results and hypothesis that NOX4 induces ICAM1 expression and may modify the glycosylated structures on ICAM1. Such modifications could potentially create a distinct binding site for monocytes or monocyte-derived macrophages rather than neutrophils, although we did not investigate the NOX4-dependent N-glycosylation state of ICAM1 in our mouse model. In our study, TNFα expression in BALF was higher in NOX4 KO mice than in WT mice at 24 h after *S. aureus* infection, coinciding with the same time points at which neutrophil recruitment increased in NOX4 KO mice. Considering that TNFα serves as a potent chemoattractant for neutrophil recruitment into the lungs following bacterial infection[122,123], and that TNFα is not the primary cytokine responsible for AM recruitment during bacterial lung infection, the heightened neutrophil recruitment observed in NOX4 KO mice at 24 h may be attributed to the increased levels of TNFα or certain unidentified chemokines.

Furthermore, our study demonstrated that the AMs were required to repair the lung injury after *S. aureus* infection. We used AM depletion to show that the absence of AMs resulted in more severe lung inflammation and tissue damage in WT mice. AMs resolve lung inflammation and repair tissue damage by up-regulating matrix metallopeptidases, which are involved in tissue remodeling[124]. Previous research has indicated that AMs are proficient in phagocytosing neutrophils recruited during pathogenic infections, utilizing scavenging receptors like CD204 or surfactant protein A[125,126]. Additionally, the effective clearance of recruited apoptotic neutrophils by AMs plays a pivotal role in ameliorating inflammation stemming from bacterial or influenza virus

infections[126-128]. These findings collectively suggest that AMs may alleviate excessive inflammation and promote resolution by eliminating infiltrated lung neutrophils following pathogenic infections, thus contributing to tissue repair. In our study, NOX4 KO mice exhibited more pronounced neutrophilic inflammation than WT mice. However, in the context of AM depletion, both WT and NOX4 KO mice displayed similar levels of neutrophilic inflammation post-infection. Although the precise mechanisms underlying how AMs regulate inflammation following *S. aureu*s infection remain elusive, these results imply that the increased abundance of AMs in WT mice potentially plays a role in resolving excessive inflammation following *S. aureus* infection.

Previously, it has been reported that AMs are characterized as tissue-resident AMs or monocyte-derived AMs[3]. In states of infection or injury, resident AMs are immediately infiltrated by recruited monocyte-derived AMs that integrate into the alveoli by transmigration and differentiation, and these resident and recruited AMs play a role in resolving infection and repairing the lung[129,130]. Although our study did not determine the origin of AMs, we demonstrated that the recruited AMs were necessary for the resolution of inflammation after *S. aureus* infection.

In Part 2, Inhibition of NETosis by GSK484 decreased IL-23 level in neutrophilic asthmatic conditions (OVA+LPS/OVA and OVA+LPS/OVA +αIL-23p19+POM1 or αCD9), suggesting that NETosis increases IL-23 level. Several studies have demonstrated this positive regulation of IL-23 level by NETosis. For example, Domizio et al.[131] previously described that LL37, an antimicrobial peptide present in DNA strands of psoriatic NETs, directly activated toll-like receptor 9 (TLR9) or cytosolic STING in monocytes, which induced Th17-related cytokines, such as IL-6 and IL-23. Lande et al.[132] also reported that NET-driven antimicrobial peptide-DNA complex activated plasmacytoid dendritic cells via TLR9 in systemic lupus erythematosus, thereby

increasing pro-inflammatory cytokines. In neutrophilic asthma, Chen et al.[133] showed that NETs could activate macrophages to increase the secreted IL-23 level during co-culture of macrophages with NETs formed in NDA conditions. These data thus support our finding of the NETosis-mediated increase of IL-23 level. This positive feedback regulation of IL-23 by NETosis suggests a central role of NETosis in establishing the severe neutrophilic asthmatic status because Th17 cell activation/neutrophilic inflammation are further aggravated and sustained due to the increased IL-23 by NETosis. This also supports our focus on NETosis when we investigated functional roles of $CD39^+CD9^+$ IMs in neutrophilic inflammation.

In neutrophilic asthma, the IL-23-Th17 axis plays a critical role in recruitment and activation of neutrophils[134]. Our results identified a potent endogenous brake that could inhibit Th17 cell activation and was also suppressed itself by IL-23 (IL-23⊣ $CD39^+CD9^+$ IMs⊣ Th17 cell activation). What is then the value of having this brake? Together with the IL-23-Th17 pathway, $CD39^+CD9^+$ IM-mediated inhibition pathway forms a coherent type 4 feed forward loop (c4FFL)[135] (Fig. 18D). According to the characteristics of FFLs[135], c4FFL causes a delay in Th17 cell activation until $CD39^+CD9^+$ IMs are completely suppressed, which makes Th17 cell activation robust against non-systematic variations of IL-23 in the microenvironment under normal conditions. In NDA conditions, the increased IL-23 suppresses $CD39^+CD9^+$ IMs, which deactivates the endogenous brake as to activate the feedback loop between NETosis and IL-23 (Fig. 18E), thereby aggravating neutrophilic inflammation. When IL-23 blockade (e.g., αIL-23p19) is used, all pathways are deactivated except for $CD39^+CD9^+$ IMs (Fig. 18F). This pan-deactivation may cause potential side effects to patients with bacterial infection because IL-23-Th-17-neutrophil activation is critical for clearance of invading bacteria (e.g., *Klebsiella pneumonia*)[136-138] or in the situations where IL-23 is needed in

other parts of bodies. Alternatively, the endogenous brake ($CD39^+CD9^+$ IMs) can be used to directly modulate NETosis, which in turn reduces IL-23 level, Th17 cell activation, and neutrophilic inflammation (Fig. 18G). $CD39^+CD9^+$ IM-based cell therapy could be thus employed as an alternative therapeutic option, as demonstrated by adoptive transfer experiments. However, the therapeutic strength of $CD39^+CD9^+$ IMs can be relatively weaker than that of IL-23 blockade because only $CD39^+CD9^+$ IMs stably adapted to the microenvironment are therapeutically effective. Therefore, combinatorial therapeutic strategies using $CD39^+CD9^+$ IMs and IL-23 blockade can be developed for optimal control of neutrophilic inflammation in severe asthma.

There were several unexpected observations or the results whose interpretation is not straightforward. First, αCD9 treatment unexpectedly led to significant increase of neutrophil count without αIL-23p19 treatment (OVA+LPS/OVA+αCD9) beyond the level in OVA+LPS/OVA, while POM1 treatment showed no significant change of the count (OVA+LPS/OVA+POM1) compared to the level in OVA+LPS/OVA. In contrast, with αIL-23p19 treatment, both αCD9 and POM1 treatments (OVA+LPS/OVA+αIL-23p19+POM1 or αCD9) increased the neutrophil count similarly up to the level in OVA+LPS/OVA. These data suggest a potential difference in the effects of αCD9 and POM1 on neutrophil count between αIL-23p19 treated and untreated conditions. Despite the difference in neutrophil count, however, $CD39^+CD9^+$ IM count and IL-23, IL-17, and IL-22 levels were not significantly different from their levels in OVA+LPS/OVA after αCD9 and POM1 treatments, neither were they even in αIL-23p19 treated conditions, suggesting that the αCD9-mediated increase in neutrophil count is independent of $CD39^+CD9^+$ IMs, IL-23, and Th17 cell activation. Combing these implications, we presume that in OVA+LPS/OVA with decreased $CD39^+CD9^+$ IMs, the cells targeted by αCD9 are some unknown cells that express only CD9, but not CD39, and capable of

suppressing neutrophil infiltration in an IL-23-Th17 axis independent manner. In contrast, in OVA+LPS/OVA+αIL-23p19 with substantial $CD39^+CD9^+$ IM counts, $CD39^+CD9^+$ IMs appear to be a major target cell type of αCD9 and POM1. Second, co-treatment of POM1 and αCD9 abolished the effect of αIL-23p19 on neutrophil count, but the abolishing extent was similar to that observed after the individual treatment (POM1 or αCD9), indicating no synergistic effect and that both of CD9 and CD39 are thus required for $CD39^+CD9^+$ IMs to inhibit NETosis. Our *ex vivo* experiments suggest that CD9 attaches $CD39^+CD9^+$ IMs to neutrophils, and CD39 then hydrolyzes extracellular ATPs nearby the neutrophils attached to $CD39^+CD9^+$ IMs to inhibit NETosis, supporting the requirement of both CD9 and CD39 for NETosis suppression. Third, $CD39^+CD9^+$ IM count in OVA+LPS/OVA was increased by GSK484 to the level in OVA+LPS/OVA+αIL-23p19, while IL-17 and IL-22 levels and neutrophil count were decreased to their levels in OVA+LPS/OVA+αIL-23p19, suggesting therapeutic effects of GSK484 comparable to αIL-23p19. Our model (Fig. 13G and 18E) provides a possible explanation for this observation that NETosis increases IL-23 level through the aforementioned positive feedback regulation, and GSK484 treatment would thereby decrease the NETosis-mediated increase of IL-23 level, which in turn reduces IL-17 and IL-22 levels and neutrophil count.

We demonstrated that the $CD39^+CD9^+$ IM axis identified from our OVA-driven model is also present in an allergen extract-derived model HDM, its functional roles in αIL-23p19-dependent suppression of neutrophilic inflammation are valid by performing all key experiments in the HDM model. In addition, cell type deconvolution analysis, which predicts fractions of $CD39^+CD9^+$ IMs (RNA CM-C3) in the lung of asthma patients using bulk gene expression profiles, identified a potential significant association (i.e., inverse correlation) of $CD39^+CD9^+$ IM fractions with asthma severity. Moreover, the

results from patients with CRS, an upper airway inflammatory disease, additionally supported clinical implications of $CD39^+CD9^+$ immune cells as potential cellular targets for neutrophilic inflammatory diseases. The results from patients with IBD also suggest a possibility that the $CD39^+CD9^+$ IM axis may play a role in the pathophysiology of the inflammatory disease. Although further detailed functional experiments are needed, these data suggest that functions of $CD39^+CD9^+$ IMs might be valid in other inflammatory diseases because Ustekinumab, a human monoclonal antibody against shared p40 subunit of IL-12 and IL-23, is commonly used to treat psoriasis, psoriatic arthritis, and IBD[139], and αIL-23p19 (risankizumab) have demonstrated efficacy for CD in clinical studies[140,141]. However, the $CD39^+CD9^+$ IM axis and its functional role are needed to be confirmed in patients with severe neutrophil-associated asthma and further to be comparatively evaluated in a large cohort including patients with mild, moderate, and severe asthma. Moreover, after confirming their validity in severe asthma patients, how $CD39^+CD9^+$ IMs can be acquired for clinical use in practice is not straightforward. Adoptive transfer experiments demonstrated that $CD39^+CD9^+$ IMs isolated from PBS/PBS and OVA+LPS/OVA+αIL-23p19 conditions showed comparable therapeutic effects, suggesting a possible strategy for acquisition of $CD39^+CD9^+$ IMs in normal conditions, which should be further investigated in a large cohort of asthma patients.

In Part 1 and 2, neutrophilic inflammation was decreased by AMs and IMs under acute and chronic inflammation (Fig. 19). These results indicated that certain types of lung macrophages should be studied further in that they could regulate inflammation. Furthermore, alternative treatment strategies for neutrophilic airway inflammation have been critical. Therefore, our finding suggests subtypes of lung macrophages are potential therapeutic targets for neutrophilic inflammation.

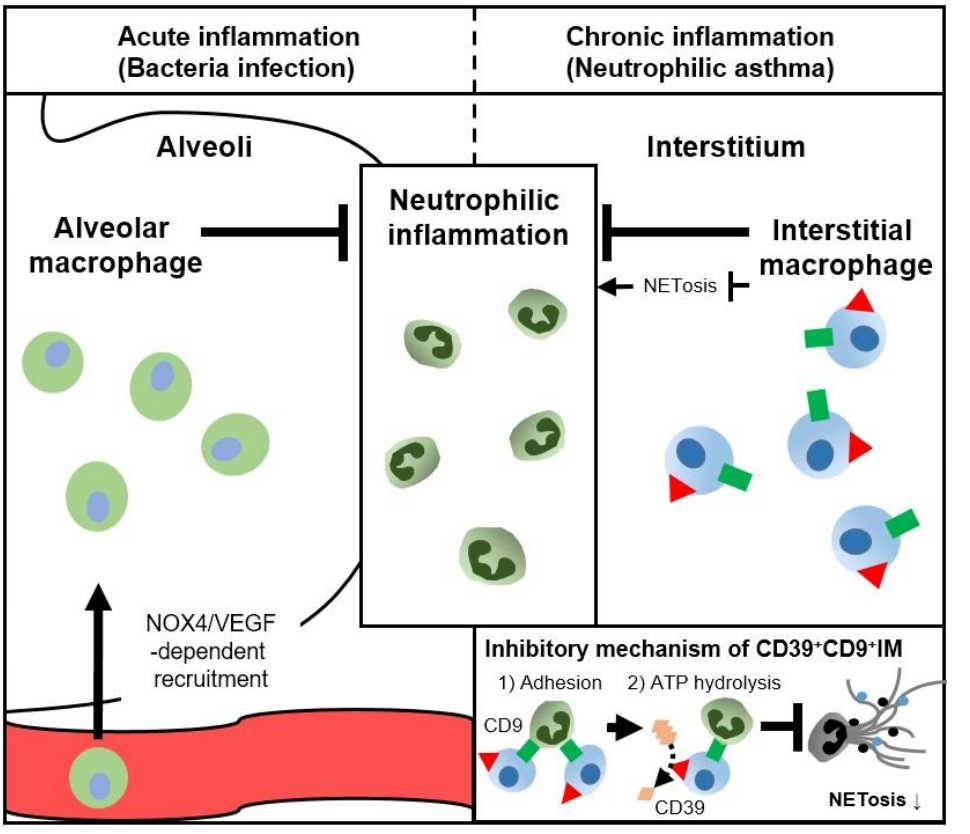

Figure 19. Schematic of the study.

V. CONCLUSION

In Part 1, we demonstrated that the presence of NOX4 is necessary to induce ICAM1 expression in lung endothelial cells after *S. aureus* infection through VEGF, which subsequently leads to the recruitment of AMs. These recruited AMs play a crucial role in reducing neutrophilic inflammation. Our findings suggest that NOX4 and its downstream signaling pathways play a crucial role in orchestrating the recruitment of AMs to resolve neutrophilic inflammation in response to *S. aureus* infection (Fig. 19). These results provide new insights into the development of novel therapeutic strategies for lung infections caused by *S. aureus*.

In Part 2, we demonstrated that IL-23 inhibitor suppressed Th17-mediated neutrophilic inflammation, and single cell analyses identified $CD39^{+}CD9^{+}$ IMs associated with therapeutic effects of αIL-23p19 in NDA mouse lungs. Also, adoptive transfer of $CD39^{+}CD9^{+}$ IMs ameliorated Th17 cell activation and neutrophilic inflammation in NDA mouse lungs. Moreover, $CD39^{+}CD9^{+}$ IMs suppressed IL-23-mediated Th17 cell activation and neutrophilic inflammation by inhibiting NETosis. In our *ex vivo* experiments, $CD39^{+}CD9^{+}$ IMs directly inhibited NETosis of neutrophils in CD39 and CD9-dependent manner. In addition, we demonstrated that the $CD39^{+}CD9^{+}$ IM axis identified from our OVA-driven model is also present in an allergen extract-derived model HDM. Furthermore, $CD39^{+}CD9^{+}$ IMs or immune cells are inversely correlated with severity of airway inflammatory diseases.

Thus, our results identified a potent endogenous brake that could inhibit Th17 cell activation and was also suppressed itself by IL-23 (IL-23⊣ $CD39^{+}CD9^{+}$ IMs⊣ Th17 cell activation).

In conclusion, we found that AM recruitment was responsible for attenuation of neutrophilic inflammation upon *S. aureus* infection in Part 1, and $CD39^{+}CD9^{+}$ IMs suppressed IL-23/Th17-mediated neutrophilic asthma by

inhibiting NETosis in Part 2. These results showed that AMs and IMs could reduce neutrophilic inflammation under specific conditions (Fig. 19). Taken together, we demonstrated that specific subtypes of macrophages had crucial roles in the regulation of airway neutrophilic inflammation in the lung.

REFERENCES

1. Aegerter H, Lambrecht BN, Jakubzick CV. Biology of lung macrophages in health and disease. Immunity 2022;55:1564-80.
2. Patel VI, Metcalf JP. Airway Macrophage and Dendritic Cell Subsets in the Resting Human Lung. Crit Rev Immunol 2018;38:303-31.
3. Hou F, Xiao K, Tang L, Xie L. Diversity of Macrophages in Lung Homeostasis and Diseases. Front Immunol 2021;12:753940.
4. Lee JW, Chun W, Lee HJ, Min JH, Kim SM, Seo JY, et al. The Role of Macrophages in the Development of Acute and Chronic Inflammatory Lung Diseases. Cells 2021;10.
5. Aberdein JD, Cole J, Bewley MA, Marriott HM, Dockrell DH. Alveolar macrophages in pulmonary host defence the unrecognized role of apoptosis as a mechanism of intracellular bacterial killing. Clin Exp Immunol 2013;174:193-202.
6. Hussell T, Bell TJ. Alveolar macrophages: plasticity in a tissue-specific context. Nat Rev Immunol 2014;14:81-93.
7. Mathie SA, Dixon KL, Walker SA, Tyrrell V, Mondhe M, O'Donnell VB, et al. Alveolar macrophages are sentinels of murine pulmonary homeostasis following inhaled antigen challenge. Allergy 2015;70:80-9.
8. Shi C, Pamer EG. Monocyte recruitment during infection and inflammation. Nat Rev Immunol 2011;11:762-74.
9. Regal-McDonald K, Xu B, Barnes JW, Patel RP. High-mannose intercellular adhesion molecule-1 enhances CD16(+) monocyte adhesion to the endothelium. Am J Physiol Heart Circ Physiol 2019;317:H1028-h38.
10. Lin YT, Chen LK, Jian DY, Hsu TC, Huang WC, Kuan TT, et al. Visfatin Promotes Monocyte Adhesion by Upregulating ICAM-1 and VCAM-1 Expression in Endothelial Cells via Activation of p38-PI3K-Akt Signaling and Subsequent ROS Production and IKK/NF-κB Activation. Cell Physiol Biochem 2019;52:1398-411.
11. McQuattie-Pimentel AC, Budinger GRS, Ballinger MN. Monocyte-derived Alveolar Macrophages: The Dark Side of Lung Repair? Am J Respir Cell Mol Biol 2018;58:5-6.
12. Allard B, Panariti A, Martin JG. Alveolar Macrophages in the Resolution of Inflammation, Tissue Repair, and Tolerance to Infection. Front Immunol 2018;9:1777.
13. Das A, Sinha M, Datta S, Abas M, Chaffee S, Sen CK, et al. Monocyte and macrophage plasticity in tissue repair and regeneration. Am J Pathol 2015;185:2596-606.

14. Westphalen K, Gusarova GA, Islam MN, Subramanian M, Cohen TS, Prince AS, et al. Sessile alveolar macrophages communicate with alveolar epithelium to modulate immunity. Nature 2014;506:503-6.
15. Jain S, Williams DJ, Arnold SR, Ampofo K, Bramley AM, Reed C, et al. Community-acquired pneumonia requiring hospitalization among U.S. children. N Engl J Med 2015;372:835-45.
16. Ryu JC, Kim MJ, Kwon Y, Oh JH, Yoon SS, Shin SJ, et al. Neutrophil pyroptosis mediates pathology of P. aeruginosa lung infection in the absence of the NADPH oxidase NOX2. Mucosal Immunol 2017;10:757-74.
17. Self WH, Wunderink RG, Williams DJ, Zhu Y, Anderson EJ, Balk RA, et al. Staphylococcus aureus Community-acquired Pneumonia: Prevalence, Clinical Characteristics, and Outcomes. Clin Infect Dis 2016;63:300-9.
18. Buvelot H, Posfay-Barbe KM, Linder P, Schrenzel J, Krause KH. Staphylococcus aureus, phagocyte NADPH oxidase and chronic granulomatous disease. FEMS Microbiol Rev 2017;41:139-57.
19. Wertheim HFL, Melles DC, Vos MC, van Leeuwen W, van Belkum A, Verbrugh HA, et al. The role of nasal carriage in Staphylococcus aureus infections. The Lancet Infectious Diseases 2005;5:751-62.
20. Parker D, Prince A. Immunopathogenesis of Staphylococcus aureus pulmonary infection. Semin Immunopathol 2012;34:281-97.
21. DeLeo FR, Diep BA, Otto M. Host defense and pathogenesis in Staphylococcus aureus infections. Infect Dis Clin North Am 2009;23:17-34.
22. Bernard K, Hecker L, Luckhardt TR, Cheng G, Thannickal VJ. NADPH oxidases in lung health and disease. Antioxid Redox Signal 2014;20:2838-53.
23. Basuroy S, Tcheranova D, Bhattacharya S, Leffler CW, Parfenova H. Nox4 NADPH oxidase-derived reactive oxygen species, via endogenous carbon monoxide, promote survival of brain endothelial cells during TNF-alpha-induced apoptosis. Am J Physiol Cell Physiol 2011;300:C256-65.
24. Martyn KD, Frederick LM, von Loehneysen K, Dinauer MC, Knaus UG. Functional analysis of Nox4 reveals unique characteristics compared to other NADPH oxidases. Cell Signal 2006;18:69-82.
25. Pendyala S, Gorshkova IA, Usatyuk PV, He D, Pennathur A, Lambeth JD, et al. Role of Nox4 and Nox2 in hyperoxia-induced reactive oxygen species generation and migration of human lung endothelial cells. Antioxid Redox Signal 2009;11:747-64.
26. Kim J, Seo M, Kim SK, Bae YS. Flagellin-induced NADPH oxidase 4

activation is involved in atherosclerosis. Sci Rep 2016;6:25437.
27. Moon JS, Nakahira K, Chung KP, DeNicola GM, Koo MJ, Pabon MA, et al. NOX4-dependent fatty acid oxidation promotes NLRP3 inflammasome activation in macrophages. Nat Med 2016;22:1002-12.
28. Kim JH, Lee J, Bae SJ, Kim Y, Park BJ, Choi JW, et al. NADPH oxidase 4 is required for the generation of macrophage migration inhibitory factor and host defense against Toxoplasma gondii infection. Sci Rep 2017;7:6361.
29. Fu P, Mohan V, Mansoor S, Tiruppathi C, Sadikot RT, Natarajan V. Role of nicotinamide adenine dinucleotide phosphate-reduced oxidase proteins in Pseudomonas aeruginosa-induced lung inflammation and permeability. Am J Respir Cell Mol Biol 2013;48:477-88.
30. Fanta CH. Asthma. N Engl J Med 2009;360:1002-14.
31. Holgate ST. Innate and adaptive immune responses in asthma. Nat Med 2012;18:673-83.
32. Levy BD, Noel PJ, Freemer MM, Cloutier MM, Georas SN, Jarjour NN, et al. Future Research Directions in Asthma. An NHLBI Working Group Report. Am J Respir Crit Care Med 2015;192:1366-72.
33. Douwes J, Gibson P, Pekkanen J, Pearce N. Non-eosinophilic asthma: importance and possible mechanisms. Thorax 2002;57:643-8.
34. Panettieri RA, Jr. Neutrophilic and Pauci-immune Phenotypes in Severe Asthma. Immunol Allergy Clin North Am 2016;36:569-79.
35. Bruijnzeel PL, Uddin M, Koenderman L. Targeting neutrophilic inflammation in severe neutrophilic asthma: can we target the disease-relevant neutrophil phenotype? J Leukoc Biol 2015;98:549-56.
36. Plantinga M, Guilliams M, Vanheerswynghels M, Deswarte K, Branco-Madeira F, Toussaint W, et al. Conventional and monocyte-derived CD11b(+) dendritic cells initiate and maintain T helper 2 cell-mediated immunity to house dust mite allergen. Immunity 2013;38:322-35.
37. Soroosh P, Doherty TA, Duan W, Mehta AK, Choi H, Adams YF, et al. Lung-resident tissue macrophages generate Foxp3+ regulatory T cells and promote airway tolerance. J Exp Med 2013;210:775-88.
38. Iezzi G, Sonderegger I, Ampenberger F, Schmitz N, Marsland BJ, Kopf M. CD40-CD40L cross-talk integrates strong antigenic

signals and microbial stimuli to induce development of IL-17-producing CD4+ T cells. Proc Natl Acad Sci U S A 2009;106:876-81.
39. Huang G, Wang Y, Chi H. Regulation of TH17 cell differentiation by innate immune signals. Cell Mol Immunol 2012;9:287-95.
40. Bettelli E, Carrier Y, Gao W, Korn T, Strom TB, Oukka M, et al. Reciprocal developmental pathways for the generation of pathogenic effector TH17 and regulatory T cells. Nature 2006;441:235-8.
41. McGeachy MJ, Chen Y, Tato CM, Laurence A, Joyce-Shaikh B, Blumenschein WM, et al. The interleukin 23 receptor is essential for the terminal differentiation of interleukin 17-producing effector T helper cells in vivo. Nat Immunol 2009;10:314-24.
42. Langrish CL, Chen Y, Blumenschein WM, Mattson J, Basham B, Sedgwick JD, et al. IL-23 drives a pathogenic T cell population that induces autoimmune inflammation. J Exp Med 2005;201:233-40.
43. Guan Q, Ma Y, Aboud L, Weiss CR, Qing G, Warrington RJ, et al. Targeting IL-23 by employing a p40 peptide-based vaccine ameliorates murine allergic skin and airway inflammation. Clin Exp Allergy 2012;42:1397-405.
44. Li Y, Sun M, Cheng H, Li S, Liu L, Qiao H, et al. Silencing IL-23 expression by a small hairpin RNA protects against asthma in mice. Exp Mol Med 2011;43:197-204.
45. Trevor JL, Deshane JS. Refractory asthma: mechanisms, targets, and therapy. Allergy 2014;69:817-27.
46. Nabhan AN, Brownfield DG, Harbury PB, Krasnow MA, Desai TJ. Single-cell Wnt signaling niches maintain stemness of alveolar type 2 cells. Science 2018;359:1118-23.
47. Zepp JA, Zacharias WJ, Frank DB, Cavanaugh CA, Zhou S, Morley MP, et al. Distinct Mesenchymal Lineages and Niches Promote Epithelial Self-Renewal and Myofibrogenesis in the Lung. Cell 2017;170:1134-48 e10.
48. Montoro DT, Haber AL, Biton M, Vinarsky V, Lin B, Birket SE, et al. A revised airway epithelial hierarchy includes CFTR-expressing ionocytes. Nature 2018;560:319-24.
49. Plasschaert LW, Zilionis R, Choo-Wing R, Savova V, Knehr J, Roma G, et al. A single-cell atlas of the airway epithelium reveals the CFTR-rich pulmonary ionocyte. Nature 2018;560:377-81.
50. LaFave LM, Kartha VK, Ma S, Meli K, Del Priore I, Lareau C, et al. Epigenomic State Transitions Characterize Tumor Progression in Mouse Lung Adenocarcinoma. Cancer Cell 2020;38:212-28 e13.

51. Little DR, Lynch AM, Yan Y, Akiyama H, Kimura S, Chen J. Differential chromatin binding of the lung lineage transcription factor NKX2-1 resolves opposing murine alveolar cell fates in vivo. Nat Commun 2021;12:2509.
52. Franks TJ, Colby TV, Travis WD, Tuder RM, Reynolds HY, Brody AR, et al. Resident cellular components of the human lung: current knowledge and goals for research on cell phenotyping and function. Proc Am Thorac Soc 2008;5:763-6.
53. Treutlein B, Brownfield DG, Wu AR, Neff NF, Mantalas GL, Espinoza FH, et al. Reconstructing lineage hierarchies of the distal lung epithelium using single-cell RNA-seq. Nature 2014;509:371-5.
54. Yu Y, Tsang JC, Wang C, Clare S, Wang J, Chen X, et al. Single-cell RNA-seq identifies a PD-1(hi) ILC progenitor and defines its development pathway. Nature 2016;539:102-6.
55. Guo M, Du Y, Gokey JJ, Ray S, Bell SM, Adam M, et al. Single cell RNA analysis identifies cellular heterogeneity and adaptive responses of the lung at birth. Nat Commun 2019;10:37.
56. Wallrapp A, Riesenfeld SJ, Burkett PR, Abdulnour RE, Nyman J, Dionne D, et al. The neuropeptide NMU amplifies ILC2-driven allergic lung inflammation. Nature 2017;549:351-6.
57. Wang A, Chiou J, Poirion OB, Buchanan J, Valdez MJ, Verheyden JM, et al. Single-cell multiomic profiling of human lungs reveals cell-type-specific and age-dynamic control of SARS-CoV2 host genes. Elife 2020;9.
58. Xu H, Ling M, Xue J, Dai X, Sun Q, Chen C, et al. Exosomal microRNA-21 derived from bronchial epithelial cells is involved in aberrant epithelium-fibroblast cross-talk in COPD induced by cigarette smoking. Theranostics 2018;8:5419-33.
59. McGovern TK, Robichaud A, Fereydoonzad L, Schuessler TF, Martin JG. Evaluation of respiratory system mechanics in mice using the forced oscillation technique. J Vis Exp 2013; doi:10.3791/50172.e50172.
60. Lee JY, Hall JA, Kroehling L, Wu L, Najar T, Nguyen HH, et al. Serum Amyloid A Proteins Induce Pathogenic Th17 Cells and Promote Inflammatory Disease. Cell 2020;180:79-91.e16.
61. Zheng GX, Terry JM, Belgrader P, Ryvkin P, Bent ZW, Wilson R, et al. Massively parallel digital transcriptional profiling of single cells. Nat Commun 2017;8:14049.
62. Stuart T, Butler A, Hoffman P, Hafemeister C, Papalexi E, Mauck WM, 3rd, et al. Comprehensive Integration of Single-Cell Data. Cell

2019;177:1888-902 e21.
63. Heng TS, Painter MW. The Immunological Genome Project: networks of gene expression in immune cells. Nat Immunol 2008;9:1091-4.
64. Aran D, Looney AP, Liu L, Wu E, Fong V, Hsu A, et al. Reference-based analysis of lung single-cell sequencing reveals a transitional profibrotic macrophage. Nat Immunol 2019;20:163-72.
65. Stuart T, Srivastava A, Madad S, Lareau CA, Satija R. Single-cell chromatin state analysis with Signac. Nat Methods 2021;18:1333-41.
66. Huang da W, Sherman BT, Lempicki RA. Systematic and integrative analysis of large gene lists using DAVID bioinformatics resources. Nat Protoc 2009;4:44-57.
67. McLean CY, Bristor D, Hiller M, Clarke SL, Schaar BT, Lowe CB, et al. GREAT improves functional interpretation of cis-regulatory regions. Nat Biotechnol 2010;28:495-501.
68. Martin M. Cutadapt removes adapter sequences from high-throughput sequencing reads. 2011 2011;17:3.
69. Kim D, Paggi JM, Park C, Bennett C, Salzberg SL. Graph-based genome alignment and genotyping with HISAT2 and HISAT-genotype. Nat Biotechnol 2019;37:907-15.
70. Anders S, Pyl PT, Huber W. HTSeq--a Python framework to work with high-throughput sequencing data. Bioinformatics 2015;31:166-9.
71. Newman AM, Steen CB, Liu CL, Gentles AJ, Chaudhuri AA, Scherer F, et al. Determining cell type abundance and expression from bulk tissues with digital cytometry. Nat Biotechnol 2019;37:773-82.
72. Modena BD, Tedrow JR, Milosevic J, Bleecker ER, Meyers DA, Wu W, et al. Gene expression in relation to exhaled nitric oxide identifies novel asthma phenotypes with unique biomolecular pathways. Am J Respir Crit Care Med 2014;190:1363-72.
73. Perotin JM, Schofield JPR, Wilson SJ, Ward J, Brandsma J, Strazzeri F, et al. Epithelial dysregulation in obese severe asthmatics with gastro-oesophageal reflux. Eur Respir J 2019;53.
74. Camiolo M, Gauthier M, Kaminski N, Ray A, Wenzel SE. Expression of SARS-CoV-2 receptor ACE2 and coincident host response signature varies by asthma inflammatory phenotype. J Allergy Clin Immunol 2020;146:315-24.e7.
75. Bolstad BM, Irizarry RA, Astrand M, Speed TP. A comparison of normalization methods for high density oligonucleotide array data based on variance and bias. Bioinformatics 2003;19:185-93.

76. Murakami Y, Ishii T, Nunokawa H, Kurata K, Narita T, Yamashita N. TLR9-IL-2 axis exacerbates allergic asthma by preventing IL-17A hyperproduction. Sci Rep 2020;10:18110.
77. Radermecker C, Sabatel C, Vanwinge C, Ruscitti C, Marechal P, Perin F, et al. Locally instructed CXCR4(hi) neutrophils trigger environment-driven allergic asthma through the release of neutrophil extracellular traps. Nat Immunol 2019;20:1444-55.
78. Fokkens WJ, Lund VJ, Hopkins C, Hellings PW, Kern R, Reitsma S, et al. European Position Paper on Rhinosinusitis and Nasal Polyps 2020. Rhinology 2020;58:1-464.
79. Hopkins C, Browne JP, Slack R, Lund V, Brown P. The Lund-Mackay staging system for chronic rhinosinusitis: how is it used and what does it predict? Otolaryngol Head Neck Surg 2007;137:555-61.
80. Park J, Jeong D, Chung YW, Han S, Kim DH, Yu J, et al. Proteomic analysis-based discovery of a novel biomarker that differentiates intestinal Behcet's disease from Crohn's disease. Sci Rep 2021;11:11019.
81. Park J, Jeong D, Chung YW, Kim DH, Cheon JH, Ryu JH. Quantitative Proteomic Analysis of the Expression of SARS-CoV-2 Receptors in the Gut of Patients with Chronic Enterocolitis. Yonsei Med J 2020;61:891-4.
82. Neupane AS, Willson M, Chojnacki AK, Vargas ESCF, Morehouse C, Carestia A, et al. Patrolling Alveolar Macrophages Conceal Bacteria from the Immune System to Maintain Homeostasis. Cell 2020;183:110-25.e11.
83. McDonald KR, Hernandez-Nichols AL, Barnes JW, Patel RP. Hydrogen peroxide regulates endothelial surface N-glycoforms to control inflammatory monocyte rolling and adhesion. Redox Biol 2020;34:101498.
84. Walpola PL, Gotlieb AI, Cybulsky MI, Langille BL. Expression of ICAM-1 and VCAM-1 and monocyte adherence in arteries exposed to altered shear stress. Arterioscler Thromb Vasc Biol 1995;15:2-10.
85. Usui T, Ishida S, Yamashiro K, Kaji Y, Poulaki V, Moore J, et al. VEGF164(165) as the pathological isoform: differential leukocyte and endothelial responses through VEGFR1 and VEGFR2. Invest Ophthalmol Vis Sci 2004;45:368-74.
86. Kim I, Moon SO, Kim SH, Kim HJ, Koh YS, Koh GY. Vascular endothelial growth factor expression of intercellular adhesion molecule 1 (ICAM-1), vascular cell adhesion molecule 1 (VCAM-1),

and E-selectin through nuclear factor-kappa B activation in endothelial cells. J Biol Chem 2001;276:7614-20.
87. Radisavljevic Z, Avraham H, Avraham S. Vascular endothelial growth factor up-regulates ICAM-1 expression via the phosphatidylinositol 3 OH-kinase/AKT/Nitric oxide pathway and modulates migration of brain microvascular endothelial cells. J Biol Chem 2000;275:20770-4.
88. Kim YM, Kim SJ, Tatsunami R, Yamamura H, Fukai T, Ushio-Fukai M. ROS-induced ROS release orchestrated by Nox4, Nox2, and mitochondria in VEGF signaling and angiogenesis. Am J Physiol Cell Physiol 2017;312:C749-c64.
89. Miyano K, Okamoto S, Yamauchi A, Kawai C, Kajikawa M, Kiyohara T, et al. The NADPH oxidase NOX4 promotes the directed migration of endothelial cells by stabilizing vascular endothelial growth factor receptor 2 protein. J Biol Chem 2020;295:11877-90.
90. Steiner DJ, Furuya Y, Metzger DW. Detrimental Influence of Alveolar Macrophages on Protective Humoral Immunity during Francisella tularensis SchuS4 Pulmonary Infection. Infect Immun 2018;86.
91. Niessen NM, Baines KJ, Simpson JL, Scott HA, Qin L, Gibson PG, et al. Neutrophilic asthma features increased airway classical monocytes. Clin Exp Allergy 2021;51:305-17.
92. Tippett E, Cameron PU, Marsh M, Crowe SM. Characterization of tetraspanins CD9, CD53, CD63, and CD81 in monocytes and macrophages in HIV-1 infection. J Leukoc Biol 2013;93:913-20.
93. Antonioli L, Pacher P, Vizi ES, Haskó G. CD39 and CD73 in immunity and inflammation. Trends Mol Med 2013;19:355-67.
94. Alashkar Alhamwe B, Miethe S, Pogge von Strandmann E, Potaczek DP, Garn H. Epigenetic Regulation of Airway Epithelium Immune Functions in Asthma. Front Immunol 2020;11:1747.
95. Waltman L, van Eck NJ. A smart local moving algorithm for large-scale modularity-based community detection. The European Physical Journal B 2013;86:471.
96. Preissl S, Fang R, Huang H, Zhao Y, Raviram R, Gorkin DU, et al. Single-nucleus analysis of accessible chromatin in developing mouse forebrain reveals cell-type-specific transcriptional regulation. Nat Neurosci 2018;21:432-9.
97. Zhang K, Hocker JD, Miller M, Hou X, Chiou J, Poirion OB, et al. A single-cell atlas of chromatin accessibility in the human genome. Cell 2021;184:5985-6001.e19.
98. Mahajan S, Saini A, Chandra V, Nanduri R, Kalra R, Bhagyaraj E, et

al. Nuclear Receptor Nr4a2 Promotes Alternative Polarization of Macrophages and Confers Protection in Sepsis. J Biol Chem 2015;290:18304-14.

99. Irazoqui JE. Key Roles of MiT Transcription Factors in Innate Immunity and Inflammation. Trends Immunol 2020;41:157-71.

100. Veremeyko T, Yung AWY, Anthony DC, Strekalova T, Ponomarev ED. Early Growth Response Gene-2 Is Essential for M1 and M2 Macrophage Activation and Plasticity by Modulation of the Transcription Factor CEBPβ. Front Immunol 2018;9:2515.

101. Ruffell D, Mourkioti F, Gambardella A, Kirstetter P, Lopez RG, Rosenthal N, et al. A CREB-C/EBPbeta cascade induces M2 macrophage-specific gene expression and promotes muscle injury repair. Proc Natl Acad Sci U S A 2009;106:17475-80.

102. Kobayashi EH, Suzuki T, Funayama R, Nagashima T, Hayashi M, Sekine H, et al. Nrf2 suppresses macrophage inflammatory response by blocking proinflammatory cytokine transcription. Nat Commun 2016;7:11624.

103. Ray N, Kuwahara M, Takada Y, Maruyama K, Kawaguchi T, Tsubone H, et al. c-Fos suppresses systemic inflammatory response to endotoxin. Int Immunol 2006;18:671-7.

104. Kawano H, Kayama H, Nakama T, Hashimoto T, Umemoto E, Takeda K. IL-10-producing lung interstitial macrophages prevent neutrophilic asthma. Int Immunol 2016;28:489-501.

105. Yadav V, Chi L, Zhao R, Tourdot BE, Yalavarthi S, Jacobs BN, et al. Ectonucleotidase tri(di)phosphohydrolase-1 (ENTPD-1) disrupts inflammasome/interleukin 1beta-driven venous thrombosis. J Clin Invest 2019;129:2872-7.

106. Bachus H, Kaur K, Papillion AM, Marquez-Lago TT, Yu Z, Ballesteros-Tato A, et al. Impaired Tumor-Necrosis-Factor-α-driven Dendritic Cell Activation Limits Lipopolysaccharide-Induced Protection from Allergic Inflammation in Infants. Immunity 2019;50:225-40.e4.

107. Daan de Boer J, Roelofs JJ, de Vos AF, de Beer R, Schouten M, Hommes TJ, et al. Lipopolysaccharide inhibits Th2 lung inflammation induced by house dust mite allergens in mice. Am J Respir Cell Mol Biol 2013;48:382-9.

108. Krishnamoorthy N, Douda DN, Bruggemann TR, Ricklefs I, Duvall MG, Abdulnour RE, et al. Neutrophil cytoplasts induce TH17 differentiation and skew inflammation toward neutrophilia in severe asthma. Sci Immunol 2018;3.

109. Delemarre T, Holtappels G, De Ruyck N, Zhang N, Nauwynck H,

Bachert C, et al. A substantial neutrophilic inflammation as regular part of severe type 2 chronic rhinosinusitis with nasal polyps. J Allergy Clin Immunol 2021;147:179-88 e2.
110. Van Buul JD, Fernandez-Borja M, Anthony EC, Hordijk PL. Expression and localization of NOX2 and NOX4 in primary human endothelial cells. Antioxid Redox Signal 2005;7:308-17.
111. Ago T, Kitazono T, Ooboshi H, Iyama T, Han YH, Takada J, et al. Nox4 as the major catalytic component of an endothelial NAD(P)H oxidase. Circulation 2004;109:227-33.
112. Carnesecchi S, Deffert C, Donati Y, Basset O, Hinz B, Preynat-Seauve O, et al. A key role for NOX4 in epithelial cell death during development of lung fibrosis. Antioxid Redox Signal 2011;15:607-19.
113. Kim HJ, Park YD, Moon UY, Kim JH, Jeon JH, Lee JG, et al. The role of Nox4 in oxidative stress-induced MUC5AC overexpression in human airway epithelial cells. Am J Respir Cell Mol Biol 2008;39:598-609.
114. Lee CF, Ullevig S, Kim HS, Asmis R. Regulation of Monocyte Adhesion and Migration by Nox4. PLoS One 2013;8:e66964.
115. Ullevig S, Zhao Q, Lee CF, Seok Kim H, Zamora D, Asmis R. NADPH oxidase 4 mediates monocyte priming and accelerated chemotaxis induced by metabolic stress. Arterioscler Thromb Vasc Biol 2012;32:415-26.
116. Fu P, Ramchandran R, Sudhadevi T, Kumar PPK, Krishnan Y, Liu Y, et al. NOX4 Mediates Pseudomonas aeruginosa-Induced Nuclear Reactive Oxygen Species Generation and Chromatin Remodeling in Lung Epithelium. Antioxidants (Basel) 2021;10.
117. Kevil CG, Patel RP, Bullard DC. Essential role of ICAM-1 in mediating monocyte adhesion to aortic endothelial cells. Am J Physiol Cell Physiol 2001;281:C1442-7.
118. Yang L, Froio RM, Sciuto TE, Dvorak AM, Alon R, Luscinskas FW. ICAM-1 regulates neutrophil adhesion and transcellular migration of TNF-alpha-activated vascular endothelium under flow. Blood 2005;106:584-92.
119. Sumagin R, Brazil JC, Nava P, Nishio H, Alam A, Luissint AC, et al. Neutrophil interactions with epithelial-expressed ICAM-1 enhances intestinal mucosal wound healing. Mucosal Immunol 2016;9:1151-62.
120. Regal-McDonald K, Patel RP. Selective Recruitment of Monocyte Subsets by Endothelial N-Glycans. Am J Pathol 2020;190:947-57.
121. Scott DW, Dunn TS, Ballestas ME, Litovsky SH, Patel RP.

Identification of a high-mannose ICAM-1 glycoform: effects of ICAM-1 hypoglycosylation on monocyte adhesion and outside in signaling. Am J Physiol Cell Physiol 2013;305:C228-37.
122. Mizgerd JP. Molecular mechanisms of neutrophil recruitment elicited by bacteria in the lungs. Semin Immunol 2002;14:123-32.
123. Vieira SM, Lemos HP, Grespan R, Napimoga MH, Dal-Secco D, Freitas A, et al. A crucial role for TNF-alpha in mediating neutrophil influx induced by endogenously generated or exogenous chemokines, KC/CXCL1 and LIX/CXCL5. Br J Pharmacol 2009;158:779-89.
124. Zasłona Z, Wilhelm J, Cakarova L, Marsh LM, Seeger W, Lohmeyer J, et al. Transcriptome profiling of primary murine monocytes, lung macrophages and lung dendritic cells reveals a distinct expression of genes involved in cell trafficking. Respir Res 2009;10:2.
125. Schagat TL, Wofford JA, Wright JR. Surfactant protein A enhances alveolar macrophage phagocytosis of apoptotic neutrophils. J Immunol 2001;166:2727-33.
126. Wong CK, Smith CA, Sakamoto K, Kaminski N, Koff JL, Goldstein DR. Aging Impairs Alveolar Macrophage Phagocytosis and Increases Influenza-Induced Mortality in Mice. J Immunol 2017;199:1060-8.
127. Serhan CN, Chiang N, Dalli J, Levy BD. Lipid mediators in the resolution of inflammation. Cold Spring Harb Perspect Biol 2014;7:a016311.
128. Knapp S, Leemans JC, Florquin S, Branger J, Maris NA, Pater J, et al. Alveolar macrophages have a protective antiinflammatory role during murine pneumococcal pneumonia. Am J Respir Crit Care Med 2003;167:171-9.
129. Puttur F, Gregory LG, Lloyd CM. Airway macrophages as the guardians of tissue repair in the lung. Immunol Cell Biol 2019;97:246-57.
130. Aegerter H, Kulikauskaite J, Crotta S, Patel H, Kelly G, Hessel EM, et al. Influenza-induced monocyte-derived alveolar macrophages confer prolonged antibacterial protection. Nat Immunol 2020;21:145-57.
131. Di Domizio J, Gilliet M. Psoriasis Caught in the NET. J Invest Dermatol 2019;139:1426-9.
132. Lande R, Ganguly D, Facchinetti V, Frasca L, Conrad C, Gregorio J, et al. Neutrophils activate plasmacytoid dendritic cells by releasing self-DNA-peptide complexes in systemic lupus erythematosus. Sci Transl Med 2011;3:73ra19.

133. Chen X, Li Y, Qin L, He R, Hu C. Neutrophil Extracellular Trapping Network Promotes the Pathogenesis of Neutrophil-associated Asthma through Macrophages. Immunol Invest 2021;50:544-61.
134. Nakajima H, Hirose K. Role of IL-23 and Th17 Cells in Airway Inflammation in Asthma. Immune Netw 2010;10:1-4.
135. Mangan S, Alon U. Structure and function of the feed-forward loop network motif. Proc Natl Acad Sci U S A 2003;100:11980-5.
136. Happel KI, Zheng M, Young E, Quinton LJ, Lockhart E, Ramsay AJ, et al. Cutting edge: roles of Toll-like receptor 4 and IL-23 in IL-17 expression in response to Klebsiella pneumoniae infection. J Immunol 2003;170:4432-6.
137. Happel KI, Dubin PJ, Zheng M, Ghilardi N, Lockhart C, Quinton LJ, et al. Divergent roles of IL-23 and IL-12 in host defense against Klebsiella pneumoniae. J Exp Med 2005;202:761-9.
138. Ye P, Rodriguez FH, Kanaly S, Stocking KL, Schurr J, Schwarzenberger P, et al. Requirement of interleukin 17 receptor signaling for lung CXC chemokine and granulocyte colony-stimulating factor expression, neutrophil recruitment, and host defense. J Exp Med 2001;194:519-27.
139. Schurich A, Raine C, Morris V, Ciurtin C. The role of IL-12/23 in T cell-related chronic inflammation: implications of immunodeficiency and therapeutic blockade. Rheumatology (Oxford) 2018;57:246-54.
140. Feagan BG, Sandborn WJ, D'Haens G, Panes J, Kaser A, Ferrante M, et al. Induction therapy with the selective interleukin-23 inhibitor risankizumab in patients with moderate-to-severe Crohn's disease: a randomised, double-blind, placebo-controlled phase 2 study. Lancet 2017;389:1699-709.
141. Feagan BG, Sandborn WJ, Gasink C, Jacobstein D, Lang Y, Friedman JR, et al. Ustekinumab as Induction and Maintenance Therapy for Crohn's Disease. N Engl J Med 2016;375:1946-60.

ABSTRACT (IN KOREAN)

호흡기 염증에서 대식세포 아형의 기능 및 조절 기전에 대한 연구

< 지도교수 유지환 >

연세대학교 대학원 의과학과

한승한

폐의 대식세포는 여러 아형으로 구성되며, 염증 상황에서 다양한 역할을 한다. 우리는 급성 호흡기 염증 상황에서 폐포 대식세포의 역할과 만성 호흡기 염증 상황에서 간질 대식세포의 역할에 대해 연구하였다.

본 연구 1부에서, 황색포도상구균 감염 시 폐포 대식세포의 유입이 폐에서 호중구성 염증을 억제하였다. 여러 병원체에 대해 폐포 대식세포는 항상성 유지와 상처 회복에 중요한 역할을 한다고 알려져 있지만, 황색포도상구균 감염 시 폐포 대식세포의 유입 방법과 작용 방법은 잘 알려지지 않았다. 우리는 황색포도상구균 감염 시 폐포 대식세포 유입을 조절하는 NADPH oxidase 4 (NOX4) 의 면역학적 역할을 규명하였다. NOX4 유전자 조작 생쥐는 야생형 생쥐에 비해서 폐포 대식세포의 유입이 감소하였고, 황색포도상구균 감염에 취약했다. 감염 시, 폐포 대식세포를 제거한 생쥐에서 대조군에 비해 호중구의 침윤, 폐 손상 그리고 염증이 증가하였다. 또한 우리의 연구는 황색포도상구균 감염 시 혈관 내피세포의 NOX4 가 ICAM1

발현을 증가시켜 폐포 대식세포 모집을 증가시키는 것을 밝혔다. 위의 결과를 통해, 우리는 혈관 내피세포의 NOX4-ICAM1 axis 를 통한 폐포 대식세포 유입이 급성 호중구 염증의 완화에 필요함을 제시하였다.

본 연구 2부에서, $CD39^+CD9^+$ 간질 대식세포는 호중구 세포외 덫 생성 (NETosis) 을 막아, IL-23-T 도움 17 (Th17) 매개된 호중구성 천식을 억제하였다. IL-23-Th17 axis 는 여러가지 염증 상황에서 호중구성 염증에 중요하다고 알려져 있다. 또한 우리의 호중구성 천식은 Th17 활성과 호중구성 염증, 그리고 NETosis 가 증가하는 양상을 보였고, 우리는 호중구성 천식에서 호중구성 염증을 억제할 수 있는 새로운 pathway를 발견하였다. 단일 세포 다중 오믹스 분석을 통해 호중구성 천식에서 감소하고, IL-23 저해 항체 처리 시 증가하는 $CD39^+CD9^+$ 간질 대식세포를 확인하였다. $CD39^+CD9^+$ 간질 대식세포의 입양 전이 (adoptive transfer) 는 NETosis 와 앞선 호중구성 천식의 양상을 억제하였다. $CD39^+CD9^+$ 간질 대식세포는 CD9을 통해 호중구에 부착하고, CD39를 통해 호중구 주위의 ATP 를 분해하여 NETosis 를 막았다. 또한 우리의 결과는 $CD39^+CD9^+$ 간질 대식세포가 IL-23-Th17 axis 만큼 효과적인 호중구성 염증 조절자라는 것을 밝혔다. 마지막으로, 심각한 천식 또는 만성 비부비동염을 가진 환자에서 $CD39^+CD9^+$ 간질 대식세포가 가벼운 천식 또는 약한 비부비동염 환자에 비해 줄어있었다. 위 결과는, IL23-Th17를 통한 호흡기 염증 질병에서 $CD39^+CD9^+$ 간질 대식세포가 세포 치료로 사용 될 가능성을 제시한다.

종합적으로, 우리는 폐에서 대식세포의 특정 아형들이 급성 및 만성 호흡기 염증 상황에서 호중구성 염증을 조절하는 중요한 역할을 한다는 사실을 규명하였다.

핵심되는 말 : 폐 대식세포, 대식세포 아형, 폐포 대식세포, 황색포도상구균, NADPH oxidase 4 (NOX4), 박테리아 감염, 간질 대식세포, 호중구성 천식, IL-23, 만성 호흡기 염증.

PUBLICATION LIST

Han SH, Moon SM, Chung YW, Ryu JH., NADPH oxidase 4-mediated alveolar macrophage recruitment to lung attenuates neutrophilic inflammation in *Staphylococcus aureus* infection. *Immune network.* 2023;23:e42.